UNIVERSITY OF CALIFORNIA,
IRVINE

Synthesis, Characterization, and Reactivity Studies on Transition Metal Amidophenolate Complexes

DISSERTATION

submitted in partial satisfaction of the requirements
for the degree of

DOCTOR OF PHILOSOPHY

in Chemistry

by

Younju (Isis) Lee

Dissertation Committee:
Professor Alan F. Heyduk, Chair
Professor Andrew S. Borovik
Professor Jenny Y. Yang

2026

TABLE OF CONTENTS

Page

LIST OF FIGURES v

LIST OF TABLES viii

LIST OF SCHEMES x

ACKNOWLEDGMENTS xii

VITA xiii

ABSTRACT OF THE DISSERTATION xiv

Chapter 1: Introduction 1

1.1. Metal-ligand cooperative reactivity 1

1.2. Catecholate-Type Redox-Active Ligands 4

1.3. Ruthenium Complexes with Catecholate-Type Ligands 7

1.4. Ligand-to-Ligand Charge-Transfer complexes 9

1.5. Contributions of this work 11

1.6. References 13

Chapter 2: Five-coordinate Aminophenol Complexes of Ruthenium(II) 19

2.1. Introduction 19

2.2. Results 21

2.2.1. Synthesis and structural characterization of a Ru(^{Ph}ap)$(PR_3)_n$ series 21

2.2.2. Spectroscopic analysis 26

2.2.3. Electrochemical analysis of 1a 27

2.2.4. Theoretical calculations 28

2.2.5. Reactivity with small molecules 29

2.3. Discussion 34

2.3.1. Determination of the oxidation states of the ligand and metal 34
2.3.2. Replacing phosphines to determine the effects of sterics 35
2.3.3. Ancillary ligand replacement 36
2.4. Conclusion 37
2.5. Experimental 38
2.6. References 46
Chapter 3: Reactivity of Ruthenium(II) Amidophenolate Complexes 50
3.1. Introduction 50
3.2. Results 52
3.2.1. Chemical oxidation of 3a 52
3.2.2. Reactivity with H_2 58
3.2.3. Reactivity with acid 60
3.2.4. Addition of azides 61
3.2.5. Reactivity with phenylacetylene 64
3.3. Discussion 66
3.3.6. Chemical oxidation of 1a 66
3.3.1. Hydrogenation 66
3.3.2. Reactivity with azide 67
3.3.3. Reactivity with phenylacetylene 68
3.4. Conclusion 69
3.5. Experimental 70
3.6. References 79
Chapter 4: Charge Transfer Complexes of Titanium(IV) and Zirconium(IV) 85
4.1. Introduction 85

4.2. Results 88
4.2.1. Synthesis 88
4.2.2. Structural Analysis 89
4.2.3. Spectroscopic Analysis 91
4.2.4. Density Functional Theory Calculations 92
4.3. Discussion 95
4.3.5. Designation of the oxidation states of the redox-active ligands and metals 95
4.3.6. Characters of the low energy charge-transfer transition 96
4.4. Conclusion 98
4.5. Experimental 100
4.6. References 105

LIST OF FIGURES

Page

Figure 1.1 Nickel based catecholate-diimine LL′CT complexes. Charge transfer from the tetrachlorocathecolate to the diimine acceptors are depicted. 10

Figure 2.1 $^{31}P\{^{1}H\}$ NMR of **1a/1b** in temperatures ranging from 20 °C (brown) to −100 °C (blue) in 20 °C increments. The peak near 58 ppm is of the metal phosphine and the peak near −7 ppm is of the free PPh_3. Triphenylphosphine oxide was added as the reference at 23.2 ppm. 22

Figure 2.2 Solid-state structure of $N_2Ru(^{Ph}ap)(PPh_3)_2$, $Ru(^{Ph}ap)(PMe_3)_3$, and $Ru(^{Ph}ap)(dppe)(PPh_3)$ with thermal ellipsoids set at 50 % probability. Hydrogen atoms and solvent molecules are omitted for clarity. 24

Figure 2.3 UV-visible spectra of **1a** and **2a-b** (left) and IR spectra of 1a (right). 26

Figure 2.4 Cyclic voltammograms of **1a** in THF (purple) and **3** in MeCN (green) at 200 mV/s. Star indicates the open circuit potential. 27

Figure 2.5 Kohn-Sham representations of the HOMO−3 to LUMO of **1a** (left to right). (iso = 0.045) 28

Figure 2.6 ORTEP diagram of $(L)_nRu(^{Ph}ap)(PPh_3)_2$ with thermal ellipsoids set at 50 % probability. Hydrogen atoms and solvent molecules are omitted. 31

Figure 2.7 UV-visible spectra of $(L)_nRu(^{Ph}ap)(PPh_3)_2$ (L = N_2, CO, $(CO)_2$, MeCN, C_2H_4) in THF. 33

Figure 2.8 IR spectrum of **1a** in KBr (top left) and scan rate dependence of **1a** in THF. 41

Figure 3.1 Experimental X-band EPR spectra of **3b** in toluene at 77 K (left) and 298 K (right). 53

Figure 3.2 UV-visible spectra of **3a-c** in THF. 53

Figure 3.3 ORTEP diagrams of **3b** (left) and **3c** (right) with thermal ellipsoids shown at 50 % probability. Hydrogen atoms, solvent molecules, and counterions have been omitted for clarity..... 54

Figure 3.4 Kohn-Sham representations of the FMOs of **3b** (left) and **3c** (right). (iso = 0.045)..... 56

Figure 3.5 Cyclic voltammograms of **3a-c** in MeCN at 200 mV/s. Star indicates the open circuit potential. 57

Figure 3.6 Zoomed in ^{1}H NMR of the H_2 addition product of **1a** in C_6D_6. 58

Figure 3.7 Relative area under the *tert*-butyl peaks of **1a** over time. 59

Figure 3.8 ORTEP diagram of **6** with thermal ellipsoids shown at 50 % probability. Hydrogen atoms and solvent molecules have been omitted for clarity. 60

Figure 3.9 ORTEP diagram of **7** with thermal ellipsoids shown at 50 % probability. Hydrogen atoms and solvent molecules have been omitted for clarity. 61

Figure 3.10 Kinetics data of the reaction between **1a** (blue) and 4 equivalents of 1-azido-4-(trifluoromethyl)benzene. The intermediate is depicted in green and product (**7**) in magenta. 63

Figure 3.11 Zoomed ^{1}H NMR and $^{13}C[^{1}H]$ NMR of **8** displaying the vinylidene proton and the metal-bound carbon. 64

Figure 3.12 ORTEP diagram of **8** with thermal ellipsoids shown at 50 % probability. Hydrogen atoms and solvent molecules have been omitted for clarity. 65

Figure 3.13 Spin density plot for **3b** with isovalues 0.0015. 72

Figure 3.14 ^{1}H NMR of the H_2 addition product to **1a** in C_6D_6. 75

Figure 3.15 ^{1}H NMR spectrum of **1a** with the addition of 1 atm H_2. 76

Figure 4.1 ^{1}H NMR of Zr(^{tBu}ap)$_2$A (A = bpy, phen dipph, ^{tBu}bpy) and Ti(^{tBu}ap)$_2$A (A = bpy, phen) (top to bottom) in benzene-d_6 at 298K. Residual proteo solvent signal appears at 7.16 ppm. Satellite peaks from the residual solvent signal are observed at 6.96 and 7.36 ppm. Minor solvent impurities from pentane and THF are present in **2a** near 0.8 ppm. 89

Figure 4.2 ORTEP diagram of **1d** with thermal ellipsoids shown at 50 % probability. Hydrogen atoms and solvent molecules have been omitted for clarity. 90

Figure 4.3 Electronic absorption spectra of complexes **1a-d**, **2a-b** (left). A zoom-in of the same spectra between 450 and 750 nm (right). 91

Figure 4.4 Kohn-Sham representations of the HOMO (bottom) and LUMO (top) of **1a-d** and **2a-b** (left to right). 92

Figure 4.5 TD-DFT UV-Vis plot (purple broken line) and experimentally obtained UV-Vis spectra (green solid line) of **1a-d**. 94

LIST OF TABLES

Page

Table 2.1 Selected bond distances (Å) and angles of solid-state structures of $(N_2)Ru(^{Ph}ap)(PPh_3)_2$, $Ru(^{Ph}ap)(PMe_3)_3$, and $Ru(^{Ph}ap)(PPh_3)$(dppe). For the five coordinate species, the two largest bond angles on the metal center are reported. 23

Table 2.2 UV-vis-NIR transition of complexes **1-5** in THF. 26

Table 2.3 Reduction potentials from cyclic voltammetry experiments for **1a** and **3** in THF and MeCN, respectively at 200 mV/s. All values are referenced to the $[FeCp_2]^{+/0}$ internal standard redox couple. 28

Table 2.4 Mulliken population analysis distributions for selected FMOs of **1a**. 29

Table 2.5 Selected bond distances (Å) and angles of solid-state structures of $(L)_nRu(^{Ph}ap)(PPh_3)_2$ (L = N_2, MeCN, CO, C_2H_4). For the five coordinate species, the two largest bond angles on the metal center are reported. 32

Table 2.6 UV-vis-NIR transition of $(L)_nRu(^{Ph}ap)(PPh_3)_2$ (L = N_2, CO, $(CO)_2$, MeCN, C_2H_4) in THF. 33

Table 2.7 X-ray diffraction data collection and refinement parameters for complexes **1-5**. 45

Table 3.1 UV-vis transition of complexes 3a-c in THF. 54

Table 3.2 Selected bond distances (Å) and angles of solid-state structures of **3a-c**. Estimated standard deviations are indicated in parentheses. 55

Table 3.3 Mulliken population analysis distributions for selected FMOs of **3b** and **3c**. 56

Table 3.4 Reduction potentials from cyclic voltammetry experiments for **3a-c** in MeCN, respectively at 200 mV/s. All values are referenced to the $[FeCp_2]^{+/0}$ internal standard redox couple. 58

Table 3.5 Selected bond distances (Å) and angles of solid-state structure of **6-8**. 62

Table 3.6 X-ray diffraction data collection and refinement parameters for complexes **3b**, **3c**, **6-8**. 74

Table 4.1 Selected bond distances of $Zr(^{tBu}ap)_2{}^{tBu}bpy$ and the previously reported $Zr(^{tBu}ap)_2(THF)_2$[30] in solid state. 90

Table 4.2 UV-vis transitions of complexes **1a-d** and **2a-b** in benzene. 92

Table 4.3 Mulliken population analysis atomic charge distributions for frontier molecular orbitals and their calculated energy difference. 93

Table 4.4 X-ray diffraction data collection and refinement parameters for complex **1d**. 103

LIST OF SCHEMES

Page

Scheme 1.1 Proposed mechanisms of the active sites of [FeFe]-hydrogenase and [NiFe]-hydrogenase displaying MLC in heterolytically cleaving H_2. The activated hydrogen is colored in blue to demonstrate the cleavage but are indifferentiable with amine protons..... 1

Scheme 1.2 Proposed mechanism of H_2 activation on a diphosphine diamine enantioselective hydrogenation catalyst for ketone hydrogenation (top) and a reversible aromatization PNP pincer complex (bottom). 3

Scheme 1.3 Heterolytic cleavage of Si–H and B–H bonds by metal thiolates. 4

Scheme 1.4 Three oxidation states of the catecholate-type ligand bound to metal. E = O, S, NR. 5

Scheme 1.5 Classification of ruthenium complexes with catecholate-type ligands by their oxidation states by Fujita et al.[45] The triplet state is omitted in the Class B iminoquinone-Ru(III) state. 7

Scheme 1.6 Alcohol oxidation catalyst reported by Tanaka et al.[52-54] 9

Scheme 2.1 Synthesis of ruthenium amidophenolate phosphine complexes (**1a**, **2a-b**). 21

Scheme 2.2 Proposed equilibrium between **1a** and **1b** in solution state..... 21

Scheme 2.3 Synthesis of $(L)_nRu(^{Ph}ap)(PPh_3)_2$ (L = N_2, MeCN, CO, C_2H_4)..... 30

Scheme 3.1 E–H bond cleaving (E = Si, B) through metal-ligand reactivity. (Ar^F = 3,5-bis(trifluoromethyl)phenyl)..... 50

Scheme 3.2 Chemical oxidation of **3a** with ferrocenium salts..... 52

Scheme 3.3 Direct and transfer hydrogenation studies performed with complex **1a**. 60

Scheme 3.4 Synthesis of the tetrazene complex **7**. 61

Scheme 3.5 Synthesis of the vinylidene complex **8**. 64

Scheme 3.6 Proposed mechanism of hydrogenation of **1a**. 66

Scheme 3.7 A potential mechanism for generating the tetrazene product **7**. 68

Scheme 4.1 The structures of a carotene-porphyrin-fullerene triad charge-transfer dye molecule and $[Ru(bpy)_3]^{2+}$ MLCT dye. The porphyrin acts as a photosensitizer which initiates the electron-hole separation. The carotene is the electron donor, and the fullerene electron acceptor. In the $[Ru(bpy)_3]^{2+}$, the charge-transfer occurs from the metal to the bipyridine ligand. 85

Scheme 4.2 Complexes presented in this chapter. 87

Scheme 4.3 Synthesis of **1a-d** and **2a-b**. 88

ACKNOWLEDGMENTS

If there was one person who was a perfect dad-coach in this world, it would be my advisor. He knows when exactly you need a little push or a pep talk and when you need gentle encouragement. He will make you believe that you have it in you to achieve anything, because he already knows it even if you don't. I was very fortunate to have Alan as my advisor, for he has cursed me with the knowledge of the highest of the standards and critical thinking skills. Most importantly, he has made this awkward kid somewhat sociable with his unrelenting dad jokes. Thank you, Alan, for teaching me how to fish.

I am grateful to my committee members, Andy and Jenny, for their invaluable feedback and support during rotation and my exams, and for fostering a close-knit inorganic community at UCI. I would not have been able to finish without their guidance.

It was a blast teaching for Ramesh for the CHEM 1 series. The ship he runs is titanic and there are wrenches thrown from all sides, but he has answers for every situation. I have learned to be a more patient and empathetic teacher from his example. I truly appreciate his support and trust.

I was extremely lucky to have overlapped with these members of the Heyduk lab. Bronte has set the standard as the most proficient scientist and experimentalist. She's the north star that I always strive to sail towards. Rachel is a brilliant mentor and an awesome friend. Her genuine passion for good science and empathetic mentorship has inspired me to be better. I am so grateful for our friendship and excited to see it grow in the coming decades. David has always entertained my existential nihilistic rants about science and the world, and I appreciate him for it. Jennifer was my comrade through the thicks and thins. I am grateful for the time we spent in and out of lab. Thank you for the adventure between countless cups of coffee, omelets, and chicken fingers. Jake is an incredibly motivated and efficient chemist, and I learned so much from him. And this is our year I can feel it man. I owe Vivian a lot for all she did for the lab. And I appreciate Bach's emotional support for the three graduating seniors. Lastly, in all seriousness, I would like to thank Steve the VAC box mascot for teaching me resilience and patience.

I am grateful for the members of our department who foster an open and collaborative culture. I was lucky to have access to equipment shared by the facility managers and their fellows, as well as equipment and chemicals from the labs in the department. Thank you especially to Dr. Joe Ziller, Sunny, Tyler, Lauren, Joseph, and Vivian for trying your best to sift through the needles and plates. Thank you to Dr. Felix Grun, Ben Katz, Dr. Philip Dennison, Dr. Suv Sengupta, Dr. Dima Fishman, and Maik Bolhorn. I am also immensely grateful for the department staff who are so knowledgeable and capable. I appreciate the members of the Borovik Lab, Evans Lab, Yang Lab, Prescher Lab, Jarvo Lab, and Dong Lab for letting me use their instruments and borrow their chemicals or ears. I am in debt of Dr. Nadia Hirbawi's acts of kindness that range from helping me with Mech homework to periodically checking in and feeding me during my time of distress.

I was also truly lucky to have been given the opportunity to participate in research as an undergraduate by Professor Joshua Figueroa and be mentored by Dr. Chinglin Joanne Chan. Dr. Haim Weizman also gave me the inspiration and courage to pursue a higher degree. I am grateful for their guidance.

The members of my smallest social circle have supported me with infinite faith and love. Attempting to put into words how I feel would be futile. I am who I am because of you.

VITA

Younju (Isis) Lee

Education

University of California, Irvine — Feb. 2026
PhD in Chemistry

University of California, San Diego — Jun. 2019
B.S. Chemistry — Magna Cum Laude
B.S. Cognitive Behavioral Neuroscience

Publications

In Preparation:

Lee, Y.; Ziller, J. W.; Heyduk, A. F. Electron-Rich Five-Coordinate Amidophenolate Complexes of Ruthenium

Lee, Y.; Ziller, J. W.; Heyduk, A. F. Metal-ligand Cooperation in Ru(II) Amidophenolate Complexes

Jaimes, J. L.; Lee, Y.; Ziller, J. W.; Heyduk, A. F. Donor-Acceptor Charge Transfer Complexes of Group IV Metals

Presentations

Oral: Synthesis and Characterization of Five-Coordinate Ru(II) Aminophenol Complexes. Lee, Y.; Heyduk, Alan F. SoCal Organometallics, Caltech, 2025.

Oral: Synthesis and Reactivity of the Isocyano Analogue of CpCo(CO) Fragment. Lee, Y.; Figueroa, J. S. Summer Research Conference, UC San Diego, 2018.

Research Experience

Graduate Student Researcher | Heyduk Lab — 2020-2026

- Investigated how covalency between the metal and ligand affect the electronic structure, reactivity and physical properties of transition metal complexes using redox-active aminophenols.

Undergraduate Researcher | Figueroa Lab — 2017-2019

- Studied low valent cobalt carbonyl analogues using sterically bulky isocyanides.

ABSTRACT OF THE DISSERTATION

Synthesis, Characterization, and Reactivity Studies on Transition Metal Amidophenolate Complexes

by
Isis Lee
Doctor of Philosophy in Chemistry
University of California, Irvine, 2026
Professor Alan F. Heyduk, Chair

Catecholate-type ligands on transition metals have demonstrated the ability to act as proton and electron reservoirs, enabling diverse chemical transformations. This dissertation investigates how redox-active amidophenolate ligands control the electronic structure, reactivity and physical properties of transition metal complexes, spanning five-coordinate ruthenium complexes as well as group IV charge-transfer dyes.

Chapter 2 examines the synthesis of a new series of five-coordinate ruthenium (II) amidophenolate complexes, $L_nRu(^{Ph}ap)(PR_3)_m$ (L = N_2, MeCN, CO, C_2H_4, ^{Ph}ap = 3,5-di-*tert*-butyl-(6-phenylamidophenolate), PR_3 = PPh_3, PMe_3, diphenylphosphinoethane). The geometry of these complexes is controlled by the rich electron density donated by the amidophenolate ligand as well as the ancillary phosphines' steric bulk. X-ray diffraction analysis supported by DFT calculations reveal a high level of covalency between the metal and amidophenolate which leads to intermediate ligand oxidation states. The apical L ligand is readily replaced, allowing these complexes to be a good platform for exploring reactivity.

Chapter 3 explores the reactivity of the ruthenium (II) amidophenolate platform. Electrochemical analysis and chemical oxidation showcase the stability of the doubly oxidized state of the complex, suggesting multielectron chemistry. H_2 activation is observed across the Ru–N bond through metal-ligand cooperation. However, exposure to excess H_2 leads to the hydrogenation of the ligand and decomposition of the complex. Addition of organic azide

produces a stable tetrazene complex which halts productive nitrene transfer, though kinetic studies suggest an imido intermediate. Reaction with phenylacetylene generates a metal vinylidene complex which enables catalytic alkyne homocoupling with moderate selectivity towards the Z-enyne.

Chapter 4 probes the effect of the d electrons of the metal and the angle of the donor and acceptor ligands in a series of group IV ligand-to-ligand charge-transfer (LL′CT) complexes. The zirconium complexes display a single low-intensity absorption band observed through UV-Vis spectroscopy, while the titanium analogues exhibit a stronger, broader absorption due to the increased level of metal and ligand orbital mixing. Modifying the bipyridine acceptor tunes the energy of the LL′CT band by up to 0.15 eV. Structural analysis through X-ray diffraction revealed the dihedral angle between the donor and acceptor ligand was near 80 °, which modulated the orbital overlap and subsequently the intensity of the transition.

Chapter 1: Introduction

1.1. Metal-ligand cooperative reactivity

In classical transition metal homogenous catalysts, the important bond-breaking and bond-making transformations occur on the metal while the coordinated ligand stays as a spectator. Elementary reactions relevant to catalysis, such as oxidative addition, reductive elimination, and ß-hydride elimination, all occur on the metal with electrons sourced from the metal d-orbitals. In designing of such catalysts, the ligand is chosen for its indirect influence on reactivity by modulating the solubility, steric environment, and electron density.

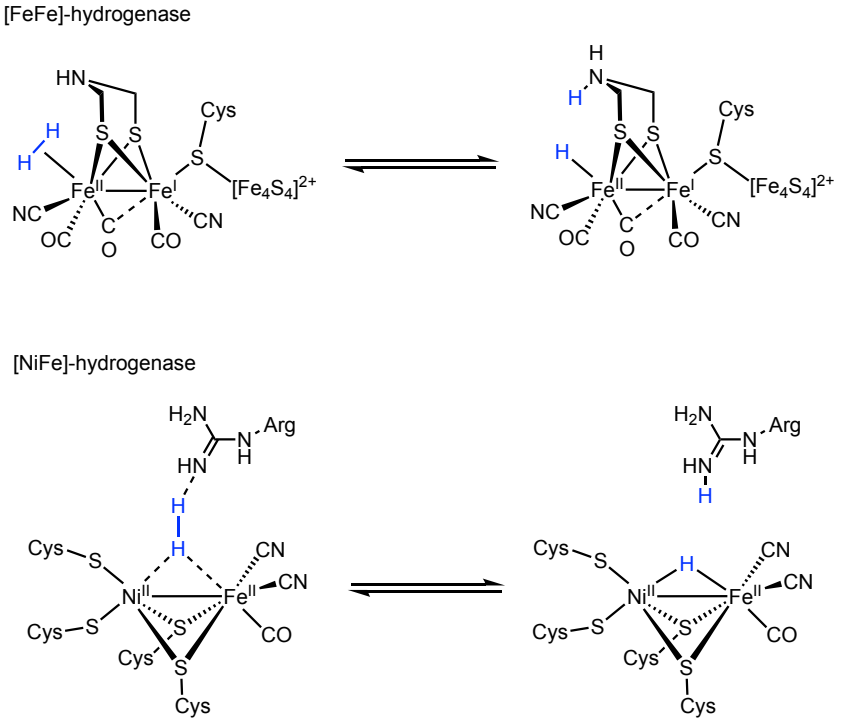

Scheme 1.1 Proposed mechanisms of the active sites of [FeFe]-hydrogenase and [NiFe]-hydrogenase displaying MLC in heterolytically cleaving H_2. The activated hydrogen is colored in blue to demonstrate the cleavage but are indifferentiable with amine protons.

However, in nature, catalysis where ligands are seen to assume a more direct role is commonly found.[1] For example, bond activations in iron containing hydrogenases involve heterolytic H_2 splitting across the metal and ligand that results in no change in the metal oxidation state as depicted in **Scheme 1.1**. Studies that inserted synthetic mimics of the

[FeFe]-hydrogenase active site into the cofactor-free form of [FeFe]-hydrogenase showed that full catalytic activity was only achieved with the analogues involving bridging azadithiolates.[2–6] Similarly, [NiFe]-hydrogenase was thought to be activating H_2 into a proton on the cystine sulfur and a hydride that bridges between the metals, although a recent study with site-directed mutagenesis discovered that a nitrogen atom from an arginine acts as the base.[7–9] In both cases, the electronegative nitrogen or sulfur is thought to be working as a proximal basic site where the H_2 can be cleaved heterolytically. Such systems inspired catalyst designs to incorporate ligands that can actively participate in chemical transformations. This type of reactivity was named as metal-ligand cooperation (MLC),[1] where both the metal and ligand are involved concertedly in the crucial bond-breaking or bond-forming step of a catalytic cycle. The terminology has been sometimes used broadly to encompass reactivity that includes hemiliable ligands or ligands in the second coordination sphere, as often seen in protein active sites. In this manuscript, MLC will be limited to examples where the metal and ligand are chemically modified and in the first coordination sphere.

One of the first examples of MLC achieved through the metathesis between a metal-ligand bond and a bond in the substrate was discovered by Noyori's group.[10–13] They reported the considerable increase of catalytic ketone hydrogenation reactivity of ruthenium complexes upon addition of diamines with an N–H group. Mechanistic studies following the initial discovery unveiled that the metal acts as the Lewis acid and the ligand acts as the Lewis base, cleaving H_2 across the metal ligand bond as a hydride and proton. The hydrogen then is transferred to the carbonyl through a pericyclic transition state, where the proton is transferred to the partially negatively charged oxygen and the hydride to the partially positively charged carbon (**Scheme 1.2**).[14–16] The first generation Noyori's catalyst has been

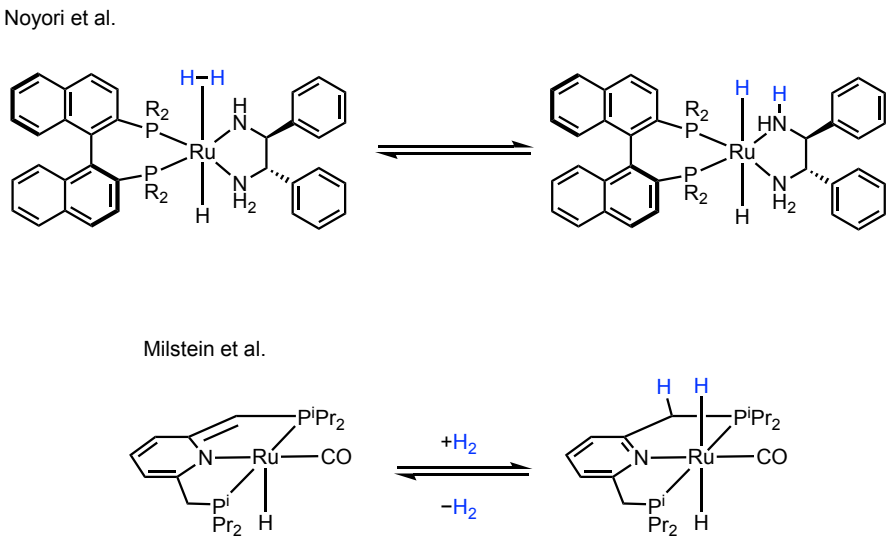

Scheme 1.2 Proposed mechanism of H_2 activation on a diphosphine diamine enantioselective hydrogenation catalyst for ketone hydrogenation (top) and a reversible aromatization PNP pincer complex (bottom).

since then developed into highly enantioselective hydrogenation catalysts by employing chiral biphosphine ligands, an achievement recognized with the 2001 Nobel Prize in Chemistry.[17] Another well studied example of hydrogenation through MLC involves a reversible aromatization on the ligand backbone that allows the hydrogen to be split across the metal and the ligand. Milstein et al demonstrated a ruthenium complex with a pyridine-amide pincer that can reversibly bind an equivalent of proton through the aromatization of the pyridine moiety as described in **Scheme 1.2**.[18] Iridium complexes of such pincer ligands have catalytically hydrogenated ketones and imines.[19,20] There are ligands containing electronegative heteroatoms such as oxygen and sulfur were also found to cleave H_2 heterolytically, the former less common due to the increased lability of coordinated alcohols. These catalysts have been applied to hydrogenation of unsaturated C=O or C=N bonds through similar metathesis mechanisms.[21,22]

The majority of studies invoking MLC is focused on the heterolytic cleavage of the H–H bond and consecutive hydrogenation. More recently, driven by the similar electronegativities of silicon and boron to hydrogen, there have been efforts to expand the scope to other E–H

bonds (E = Si, B).[23] Select systems that can cleave H_2 across the metal and ligand have demonstrated the ability to activate hydrosilanes or hydroboranes. The affinity of silicon to electronegative atoms such as sulfur have been utilized in designing a ruthenium arene with a tethered thiolate that can perform catalytic hydrosilylation to pyridines and carbonyls. (**Scheme 1.3**)[24–26] The same system has also been shown to heterolytically cleave B–H bonds and catalytically borylate pyrroles. Similar strategies employing other electronegative atoms such as nitrogen and oxygen on ligands have been shown to be effective in cleaving E–H bonds.

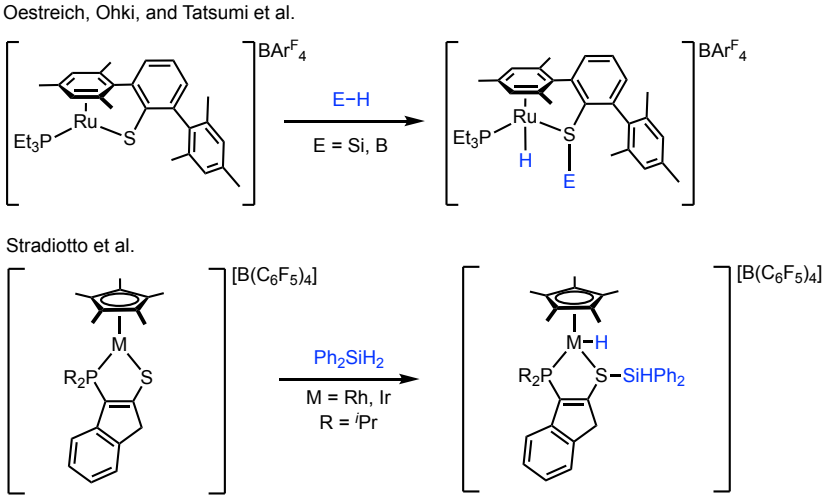

Scheme 1.3 Heterolytic cleavage of Si–H and B–H bonds by metal thiolates.

1.2. Catecholate-Type Redox-Active Ligands

One of the prerequisites for MLC reactivity is that the bonding mode of the ligand and the metal must be altered upon activation of a substrate, as the chemical change happens in the first coordination sphere. Typically, this change is seen as the ligand changes from an X-type to an L-type upon the addition of the proton, silicon, or boron. Therefore, the ligand acts as a reservoir for a proton analogue, ideally while still bound to the metal. A well-studied family of ligands that can act as a proton reservoir are ortho-catecholates and their analogues. A library of studies has been published on their capability to modulate the thermodynamics

of hydrogen atom transfer reactions, owing to their ability to store electrons in addition to protons.[27–31]

The capacity of catecholate-type ligands to act as electron reservoirs puts them in a category of ligands labeled redox-active. Redox-active ligands are characterized by their ability to exist in multiple oxidation states bound to a metal, owing to the proximity of the energies of the ligand frontier molecular orbitals (FMOs) and the metal d-orbitals. Their characteristics have made them the object of studies for 60 years since the seminal review by Jørgensen, where he introduced the terminology of "innocent" ligands as ligands that allow the metal oxidation state to be determined unambiguously.[32] While oftentimes both terms are used interchangeably, the term "redox-active" is now more reserved for ligands that are stable in their multiple oxidation states bound to metal, while in the traditional term of "non-innocent" encompasses all ligands that display ambiguity in their oxidation state.[33]

As a prototypical example such ligand class, catecholate-type ligands can stably bind to metal in three distinct oxidation states ranging from the fully reduced catecholate dianion to the fully oxidized neutral quinone. The resulting ambiguity of the ligand oxidation state in ortho-catecholate complexes necessitates multiple experimental evidence from various spectroscopic and electrochemical methods to elicit them. Due to the sensitivity of bond lengths within the ligand to its oxidation state, single-crystal X-ray diffraction is a useful tool to characterize complexes with catecholate-type ligands. As depicted in **Scheme 1.4**, as the ligand gets oxidized, the bond distances within the ligand will bear characteristics of different bond orders. The C(3)–C(4), C(5)–C(6), C(1)–E, and C(2)–E bond distances contract due to double bonds becoming more localized, while C(1)–C(2), C(2)–C(3), and C(4)–C(5) bond

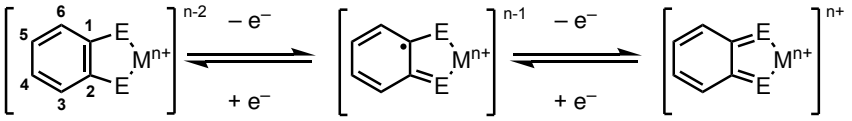

Scheme 1.4 Three oxidation states of the catecholate-type ligand bound to metal. E = O, S, NR.

distances increase due to them developing more single bond character.[34,35] For certain catecholate analogues that have a large library of reported complexes, Brown developed the "Metrical Oxidation State" (MOS) calculator that allows the determination of ligand oxidation state through comparison of structural data.[36]

The high resolution metrical data from the solid-state bond distances can be corroborated with solution state bulk spectroscopic analysis. Transition metal complexes with catecholate type ligands in the semiquinone or quinone state are known to be intensely colored, which can be characterized through UV-Vis-NIR spectroscopy. The identities of these intense absorptions are mainly charge transfers between metal and ligand or in the semiquinone state, intraligand π to π* transitions. These transitions typically show up in the lower energy region higher than 600 nm with the absorption coefficient near 10^4 M^{-1} cm^{-1}.[37–40] Electron paramagnetic resonance (EPR) spectroscopy for radicals and nuclear magnetic resonance (NMR) spectroscopy for diamagnetic complexes are also useful to determining the oxidation state of the ligand and location of the electrons. For a S = 1/2 spin system where the unpaired electron is localized on the ligand, the EPR spectra is similar to a free semiquinone with an isotropic signal near $g = 2.00$.[41–44] For diamagnetic systems, the ^{1}H NMR chemical shifts for the protons on the catecholate-type ligands alter significantly between different oxidation states. The electronic structure of transition metal complexes with catecholate-type ligands can be characterized further with voltammetry studies. The redox-active π system on the ligands exhibit redox couples at more mild potentials compared to metal based redox processes. Due to the chelating effect of the ligand, two reversible reduction events localized on the ligand are commonly observed in the cyclic voltammograms.[44] The open circuit potential is another key evidence that is used in assigning the ligand oxidation state by comparing it to the potentials of the reduction events.

1.3. Ruthenium Complexes with Catecholate-Type Ligands

Ruthenium complexes with catecholate analogues have been studied intensively due to the good match of metal d-orbital and ligand FMO energy. Fujita and coworkers have compiled the extensive library of these complexes, with the classification of the four stable oxidation states of the ruthenium catecholate-type complexes.[45] Within the four classes, there

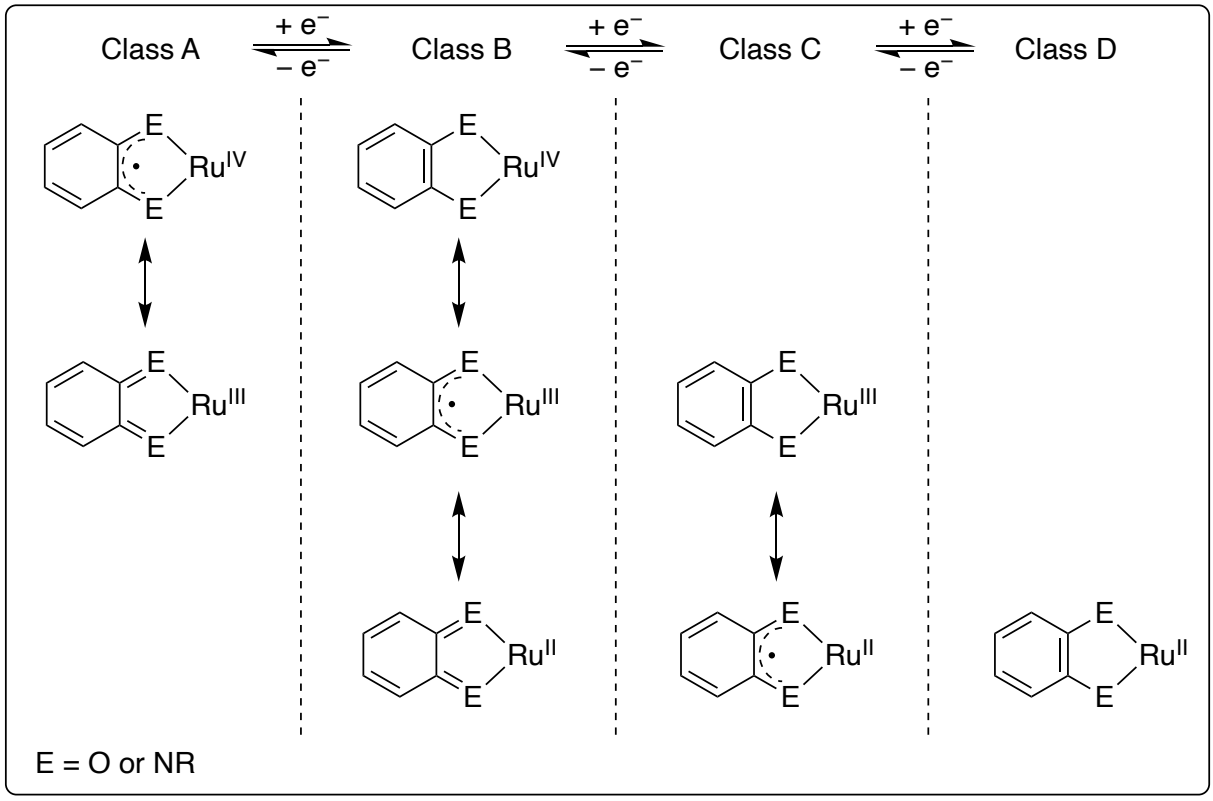

Scheme 1.5 Classification of ruthenium complexes with catecholate-type ligands by their oxidation states by Fujita et al.[45] The triplet state is omitted in the Class B iminoquinone-Ru(III) state.

are multiple possible oxidation state assignments for the metal and ligand, which is controlled by the selection of the ligand backbone, ancillary ligands, and other environmental factors of the complex. The most reduced form is the unambiguous Class D, where the ligand is expected to be in the fully reduced catecholate oxidation state and the metal is in the +2 oxidation state. One electron oxidation of the Class D complexes result in the Class C, where the unpaired electron could reside on the ligand in the semiquinone oxidation state paired with the Ru(II) metal, or on the metal as Ru(III) with the catecholate state ligand.

Consecutive one electron oxidation of Class C complexes results in Class B, which has the most options possible for ligand and metal oxidation state assignment. The ligand could be in the fully oxidized state as a quinone bound to a Ru(II) center, as a semiquinone bound to a Ru(III), or catecholate bound to Ru(IV). In addition, the semiquinone-Ru(III) configuration could be a triplet or a singlet which involves ferromagnetic coupling between the radicals on the ligand and metal. Lastly, another one electron oxidation from the Class B complexes leads to Class A, where a semiquinone could be bound to a Ru(IV) center or a quinone could be complexed to a Ru(III). The multiple possible ligand and metal oxidation state for these ruthenium complexes with catecholate-type ligands necessitates the careful corroboration of experimental evidence discussed above, especially with complexes with more than one catecholate analogues, which is not uncommon.[37–40,46,47]

To add to the complexity of the electronic structure of these complexes, the good energy match between the metal d-orbitals and the ligand π system results in increased covalency between the metal and ligand. This results in diffused electron density across metal and ligand owing to the contributions from multiple resonance forms, which leads to experimental data that could be interpreted as intermediate, noninteger oxidation states for both metal and ligand.[48–51] For instance, solid-state bond distances of the ligand commonly lie between the average bond distances tabulated from other transition metal catecholate-type ligand complexes. Therefore, in addition to the multiple experimental data, density functional theory (DFT) calculations are often used to aid in finding the extent of the metal and ligand contributions to the complexes' FMOs.[40,52,53]

The aforementioned unique electronic characteristics of the ruthenium complexes with catecholate-type ligands have been studied intensively for their potential in catalysis due to the increased electronic communication between the metal and ligand. However, reactivity studies of these systems are limited compared to the vast literature of fundamental studies.

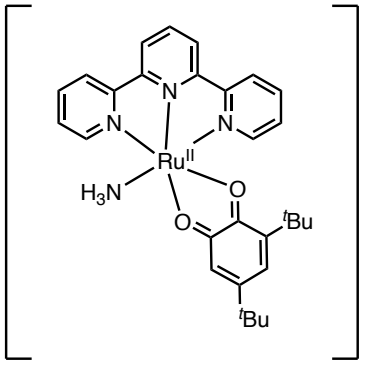

Scheme 1.6 Alcohol oxidation catalyst reported by Tanaka et al.[52-54]

Tanaka and coworkers have demonstrated the electrocatalytic oxidation of alcohols using a Ru(II)-quinone-ammonia complex, which utilized the stability of a high oxidation state intermediate owing to the electron density donated from the ligand.[54–56] To date, most of the reactivity studies employ the strategy of stabilizing the high oxidation state intermediate through the increased electron density donation from the ligand to the metal, focused on Class B complexes.

1.4. Ligand-to-Ligand Charge-Transfer complexes

The tunable FMO energies of redox-active ligands make them valuable for photochemical energy conversion. A prominent example is a class of molecular dyes that utilize the intramolecular charge transfers observed in metal complexes with redox-active ligands, as discussed in Section 1.2. An early model of such charge-transfer dye is the $[Ru(bpy)^3]^{2+}$.[57,58] The photoinduced metal-to-ligand charge-transfer (MLCT) occurs between the metal d-orbital and the bipyridine π* orbitals, owing to the ability of bipyridine to be reduced by an electron. The advantages of transition metal complex charge-transfer dyes include the ease of synthesis and customizability of the ligands compared to their extended conjugated organic counterparts. However, in MLCT dyes, the distance of the charge transfer is shorter, increasing the probability of rapid recombination of the excited electron and hole pair back to the ground state. To extend the distance between the electron-hole pair, transition metal dyes where the HOMO and LUMO are located in separate ligands have been designed. In these dyes, the electron is excited from one redox-active ligand to another, performing ligand-to-ligand charge-transfer (LL′CT).

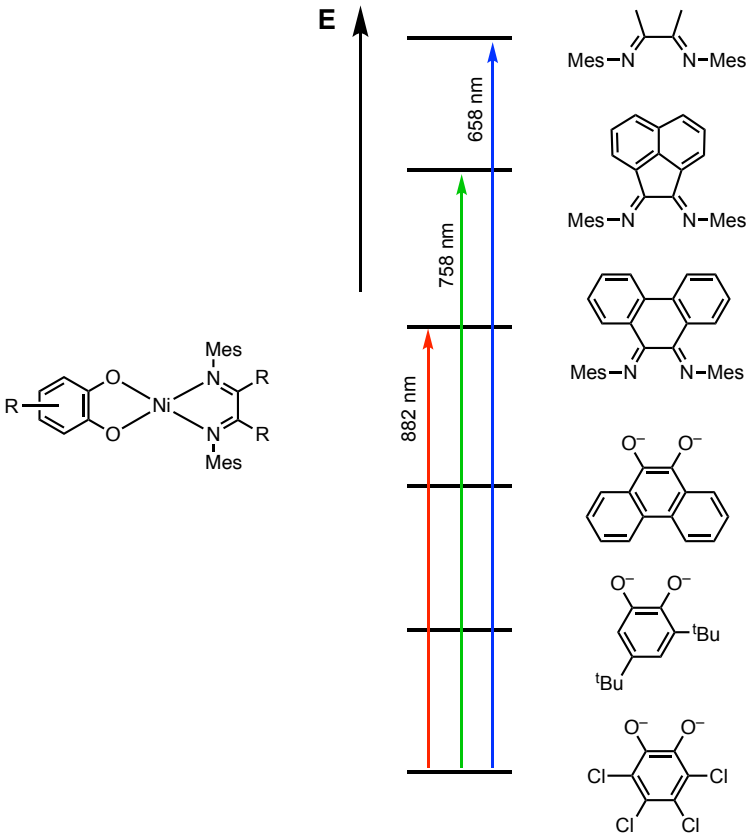

Figure 1.1 Nickel based catecholate-diimine LL′CT complexes. Charge transfer from the tetrachlorocathecolate to the diimine acceptors are depicted.

Previous studies in the lab have showcased the tunability of the absorption profile of a series of Ni(II) catecholate diimine LL′CT complexes through modification of the ligands.[59,60] In this system, charge-transfer occurs from the fully reduced catecholates to the fully oxidized diimines, as confirmed by the sensitivity of the electromagnetic absorption profile to the electron donating or electron withdrawing character of the ligand backbones. The charge-transfer band is further characterized by its sensitivity to the solvent polarity, displaying a solvatochromic shift due to the excited state after the charge-transfer being less polar compared to the ground state. The relative energies of the ligand π systems agreed with the relative reduction potentials observed for the oxidation of the catecholates and the reduction of the diimines within the complexes. As a result of the varying HOMO and LUMO energy gaps, the LL′CT band in the UV-Vis region could be tuned up to 0.8 eV.

The system above utilizes the increased overlap between the donor and acceptor ligands' π systems coming from the square planar arrangement about the d^8 metal. Fewer systems with lower number of metal d electrons have been reported. Recent studies have found that a small amount of orbital mixing from redox-active metal orbitals aid in LL′CT when the dihedral angle between the ligands are less than 180 °. Zhang and coworkers have reported early metal diazabutadiene systems where the DFT calculations predict a higher oscillator strength of the LLCT band compared to experimental results.[61] They have attributed this to the overlap integral predominantly originating from the d orbital of the metal, which suggests that the redox-active metal is contributing to the Laporte-allowed charge-transfer.

1.5. Contributions of this work

The work presented in this dissertation investigates transition metal amidophenolate complexes.

Chapter 2 discusses the synthesis and characterization of a series of five-coordinate ruthenium (II) amidophenolate phosphine complexes and their reactivity with small π acids. The electron density donation from the ligand to the metal due to the good overlap of their orbital energies lead to the low coordination number, while the sterics from bulky phosphines force an equilibrium between a phosphine-bound and dinitrogen-bound complex in room temperature. The pendant dinitrogen bound to the metal is easily replaced with other π acids such as acetonitrile, carbon monoxide, and ethylene, though no activation of bound π acids was observed.

Chapter 3 investigates the MLC and multi-electron reactivity of the complexes characterized in Chapter 2. The basic amine on the amidophenolate can act as a proton reservoir, splitting H_2 heterolytically. Kinetic studies suggest that the activation of the

dihydrogen goes through an early transition state, binding as a dihydrogen first to the metal before being heterolytically cleaved across the metal-ligand bond. While the complex was not stable under excess H_2 which prevented catalytic hydrogenation of substrates, catalytic transfer hydrogenation was observed using NH_3BH_3 as the hydrogen source. Addition of excess aryl azides to the complex resulted in the generation of a five-coordinate tetrazene complex, which did not display any nitrene transfer to substrates. However, an intermediate is observed in the ^1H NMR and the addition of substrates before the azide leads to generation of some nitrene transfer products. This suggests the possibility of a transient imido capable of nitrene transfer forming before an equivalent of azide traps it.

Chapter 4 investigates a series of group IV amidophenolate bipyridine complexes and the effects of the geometry and metal d electrons on the charge-transfer band. The LL′CT band was sensitive to the identity of the electron acceptor bipyridine and could be tuned by up to 0.15 eV. The titanium complexes exhibit broader and higher intensity absorption from the low energy LMCT, but the zirconium complexes possess a cleaner low intensity LL′CT peak due to the higher energy of the LMCT.

1.6. References

(1) Que, L.; Tolman, W. B. Biologically Inspired Oxidation Catalysis. *Nature* **2008**, *455* (7211), 333–340. https://doi.org/10.1038/nature07371.

(2) Berggren, G.; Adamska, A.; Lambertz, C.; Simmons, T. R.; Esselborn, J.; Atta, M.; Gambarelli, S.; Mouesca, J.-M.; Reijerse, E.; Lubitz, W.; Happe, T.; Artero, V.; Fontecave, M. Biomimetic Assembly and Activation of [FeFe]-Hydrogenases. *Nature* **2013**, *499* (7456), 66–69. https://doi.org/10.1038/nature12239.

(3) Esselborn, J.; Lambertz, C.; Adamska-Venkates, A.; Simmons, T.; Berggren, G.; Noth, J.; Siebel, J.; Hemschemeier, A.; Artero, V.; Reijerse, E.; Fontecave, M.; Lubitz, W.; Happe, T. Spontaneous Activation of [FeFe]-Hydrogenases by an Inorganic [2Fe] Active Site Mimic. *Nat. Chem. Biol.* **2013**, *9* (10), 607–609. https://doi.org/10.1038/nchembio.1311.

(4) Schilter, D.; Rauchfuss, T. B. And the Winner is…Azadithiolate: An Amine Proton Relay in the [FeFe] Hydrogenases. *Angew. Chem. Int. Ed.* **2013**, *52* (51), 13518–13520. https://doi.org/10.1002/anie.201307132.

(5) Esselborn, J.; Muraki, N.; Klein, K.; Engelbrecht, V.; Metzler-Nolte, N.; Apfel, U.-P.; Hofmann, E.; Kurisu, G.; Happe, T. A Structural View of Synthetic Cofactor Integration into [FeFe]-Hydrogenases. *Chem. Sci.* **2016**, *7* (2), 959–968. https://doi.org/10.1039/C5SC03397G.

(6) Siebel, J. F.; Adamska-Venkatesh, A.; Weber, K.; Rumpel, S.; Reijerse, E.; Lubitz, W. Hybrid [FeFe]-Hydrogenases with Modified Active Sites Show Remarkable Residual Enzymatic Activity. *Biochemistry* **2015**, *54* (7), 1474–1483. https://doi.org/10.1021/bi501391d.

(7) Evans, R. M.; Brooke, E. J.; Wehlin, S. A. M.; Nomerotskaia, E.; Sargent, F.; Carr, S. B.; Phillips, S. E. V.; Armstrong, F. A. Mechanism of Hydrogen Activation by [NiFe] Hydrogenases. *Nat. Chem. Biol.* **2016**, *12* (1), 46–50. https://doi.org/10.1038/nchembio.1976.

(8) Ogata, H.; Nishikawa, K.; Lubitz, W. Hydrogens Detected by Subatomic Resolution Protein Crystallography in a [NiFe] Hydrogenase. *Nature* **2015**, *520* (7548), 571–574. https://doi.org/10.1038/nature14110.

(9) Tai, H.; Hirota, S. Mechanism and Application of the Catalytic Reaction of [NiFe] Hydrogenase: Recent Developments. *ChemBioChem* **2020**, *21* (11), 1573–1581. https://doi.org/10.1002/cbic.202000058.

(10) Noyori, R.; Koizumi, M.; Ishii, D.; Ohkuma, T. Asymmetric Hydrogenation via Architectural and Functional Molecular Engineering. *Pure Appl. Chem.* **2001**, *73* (2), 227–232. https://doi.org/10.1351/pac200173020227.

(11) Noyori, R.; Ohkuma, T. Asymmetric Catalysis by Architectural and Functional Molecular Engineering: Practical Chemo- and Stereoselective Hydrogenation of Ketones.

Angew. Chem. Int. Ed. **2001**, *40* (1), 40–73. https://doi.org/10.1002/1521-3773(20010105)40:1%253C40::AID-ANIE40%253E3.0.CO;2-5.

(12) Noyori, R.; Hashiguchi, S. Asymmetric Transfer Hydrogenation Catalyzed by Chiral Ruthenium Complexes. *Acc. Chem. Res.* **1997**, *30* (2), 97–102. https://doi.org/10.1021/ar9502341.

(13) Doucet, H.; Ohkuma, T.; Murata, K.; Yokozawa, T.; Kozawa, M.; Katayama, E.; England, A. F.; Ikariya, T.; Noyori, R. Trans-[RuCl2(Phosphane)2(1,2-Diamine)] and Chiral Trans-[RuCl2(Diphosphane)(1,2-Diamine)]: Shelf-Stable Precatalysts for the Rapid, Productive, and Stereoselective Hydrogenation of Ketones. *Angew. Chem. Int. Ed.* **1998**, *37* (12), 1703–1707. https://doi.org/10.1002/(SICI)1521-3773(19980703)37:12%253C1703::AID-ANIE1703%253E3.0.CO;2-I.

(14) Leyssens, T.; Peeters, D.; Harvey, J. N. Origin of Enantioselective Hydrogenation of Ketones by RuH_2 (Diphosphine)(Diamine) Catalysts: A Theoretical Study. *Organometallics* **2008**, *27* (7), 1514–1523. https://doi.org/10.1021/om700940m.

(15) Di Tommaso, D.; French, S. A.; Zanotti-Gerosa, A.; Hancock, F.; Palin, E. J.; Catlow, C. R. A. Computational Study of the Factors Controlling Enantioselectivity in Ruthenium(II) Hydrogenation Catalysts. *Inorg. Chem.* **2008**, *47* (7), 2674–2687. https://doi.org/10.1021/ic701981v.

(16) Ohkuma, T.; Utsumi, N.; Tsutsumi, K.; Murata, K.; Sandoval, C.; Noyori, R. The Hydrogenation/Transfer Hydrogenation Network: Asymmetric Hydrogenation of Ketones with Chiral η^6 -Arene/ *N*-Tosylethylenediamine–Ruthenium(II) Catalysts. *J. Am. Chem. Soc.* **2006**, *128* (27), 8724–8725. https://doi.org/10.1021/ja0620989.

(17) Sandoval, C. A.; Ohkuma, T.; Muñiz, K.; Noyori, R. Mechanism of Asymmetric Hydrogenation of Ketones Catalyzed by BINAP/1,2-Diamine–Ruthenium(II) Complexes. *J. Am. Chem. Soc.* **2003**, *125* (44), 13490–13503. https://doi.org/10.1021/ja030272c.

(18) Zhang, J.; Leitus, G.; Ben-David, Y.; Milstein, D. Facile Conversion of Alcohols into Esters and Dihydrogen Catalyzed by New Ruthenium Complexes. *J. Am. Chem. Soc.* **2005**, *127* (31), 10840–10841. https://doi.org/10.1021/ja052862b.

(19) Chen, X.; Jia, W.; Guo, R.; Graham, T. W.; Gullons, M. A.; Abdur-Rashid, K. Highly Active Iridium Catalysts for the Hydrogenation of Ketones and Aldehydes. *Dalton Trans.* **2009**, No. 8, 1407. https://doi.org/10.1039/b815501a.

(20) Clarke, Z. E.; Maragh, P. T.; Dasgupta, T. P.; Gusev, D. G.; Lough, A. J.; Abdur-Rashid, K. A Family of Active Iridium Catalysts for Transfer Hydrogenation of Ketones. *Organometallics* **2006**, *25* (17), 4113–4117. https://doi.org/10.1021/om060049z.

(21) Musa, S.; Shaposhnikov, I.; Cohen, S.; Gelman, D. Ligand–Metal Cooperation in PCP Pincer Complexes: Rational Design and Catalytic Activity in Acceptorless Dehydrogenation of Alcohols. *Angew. Chem. Int. Ed.* **2011**, *50* (15), 3533–3537. https://doi.org/10.1002/anie.201007367.

(22) Silantyev, G. A.; Filippov, O. A.; Musa, S.; Gelman, D.; Belkova, N. V.; Weisz, K.; Epstein, L. M.; Shubina, E. S. Conformational Flexibility of Dibenzobarrelene-Based PC(Sp^3)P Pincer Iridium Hydride Complexes: The Role of Hemilabile Functional Groups and External Coordinating Solvents. *Organometallics* **2014**, *33* (21), 5964–5973. https://doi.org/10.1021/om500308g.

(23) Higashi, T.; Kusumoto, S.; Nozaki, K. Cleavage of Si–H, B–H, and C–H Bonds by Metal–Ligand Cooperation: Focus Review. *Chem. Rev.* **2019**, *119* (18), 10393–10402. https://doi.org/10.1021/acs.chemrev.9b00262.

(24) Hesp, K. D.; McDonald, R.; Ferguson, M. J.; Stradiotto, M. New Cationic and Zwitterionic Cp*M(κ² -P,S) Complexes (M = Rh, Ir): Divergent Reactivity Pathways Arising from Alternative Modes of Ancillary Ligand Participation in Substrate Activation. *J. Am. Chem. Soc.* **2008**, *130* (48), 16394–16406. https://doi.org/10.1021/ja8062277.

(25) Stahl, T.; Müther, K.; Ohki, Y.; Tatsumi, K.; Oestreich, M. Catalytic Generation of Borenium Ions by Cooperative B–H Bond Activation: The Elusive Direct Electrophilic Borylation of Nitrogen Heterocycles with Pinacolborane. *J. Am. Chem. Soc.* **2013**, *135* (30), 10978–10981. https://doi.org/10.1021/ja405925w.

(26) Stahl, T.; Hrobárik, P.; Königs, C. D. F.; Ohki, Y.; Tatsumi, K.; Kemper, S.; Kaupp, M.; Klare, H. F. T.; Oestreich, M. Mechanism of the Cooperative Si–H Bond Activation at Ru–S Bonds. *Chem. Sci.* **2015**, *6* (7), 4324–4334. https://doi.org/10.1039/C5SC01035G.

(27) Lu, F.; Zarkesh, R. A.; Heyduk, A. F. A Redox-Active Ligand as a Reservoir for Protons and Electrons: O2 Reduction at Zirconium(IV). *Eur. J. Inorg. Chem.* **2012**, *2012* (3), 467–470. https://doi.org/10.1002/ejic.201100798.

(28) Charette, B. J.; Ziller, J. W.; Heyduk, A. F. Exploring Ligand-Centered Hydride and H-Atom Transfer. *Inorg. Chem.* **2021**, *60* (7), 5367–5375. https://doi.org/10.1021/acs.inorgchem.1c00351.

(29) Charette, B. J. Investigations into the Reactivity of Transition Metal Complexes with Redox-Active Ligands for Proton Coupled Electron Transfer and Nitrene Transfer, University of California, Irvine, 2021. https://escholarship.org/uc/item/2p70w8nm.

(30) Charette, B. J.; Ziller, J. W.; Heyduk, A. F. Metal-Ion Influence on Ligand-Centered Hydrogen-Atom Transfer. *Inorg. Chem.* **2021**, *60* (3), 1579–1589. https://doi.org/10.1021/acs.inorgchem.0c02981.

(31) Rosenkoetter, K. E.; Wojnar, M. K.; Charette, B. J.; Ziller, J. W.; Heyduk, A. F. Hydrogen-Atom Noninnocence of a Tridentate [SNS] Pincer Ligand. *Inorg. Chem.* **2018**, *57* (16), 9728–9737. https://doi.org/10.1021/acs.inorgchem.8b00618.

(32) Jørgensen, Chr. K. Differences between the Four Halide Ligands, and Discussion Remarks on Trigonal-Bipyramidal Complexes, on Oxidation States, and on Diagonal Elements of One-Electron Energy. *Coord. Chem. Rev.* **1966**, *1* (1), 164–178. https://doi.org/10.1016/S0010-8545(00)80170-8.

(33) Chirik, P. J. Preface: Forum on Redox-Active Ligands. *Inorg. Chem.* **2011**, *50* (20), 9737–9740. https://doi.org/10.1021/ic201881k.

(34) Pierpont, C. G.; Buchanan, R. M. Transition Metal Complexes of O-Benzoquinone, o-Semiquinone, and Catecholate Ligands. *Coord. Chem. Rev.* **1981**, *38* (1), 45–87. https://doi.org/10.1016/S0010-8545(00)80499-3.

(35) Fox, G. A.; Pierpont, C. G. Periodic Trends in Charge Distribution for Transition Metal Complexes Containing Catecholate and Semiquinone Ligands. Metal-Mediated Spin Coupling in the Bis(3,5-Di-Tert-Butyl-1,2-Semiquinone) Complexes of Palladium(II) and Platinum(II) M(DBSQ)2 (M = Pd, Pt). *Inorg. Chem.* **1992**, *31* (18), 3718–3723. https://doi.org/10.1021/ic00044a012.

(36) Brown, S. N. Metrical Oxidation States of 2-Amidophenoxide and Catecholate Ligands: Structural Signatures of Metal–Ligand π Bonding in Potentially Noninnocent Ligands. *Inorg. Chem.* **2012**, *51* (3), 1251–1260. https://doi.org/10.1021/ic202764j.

(37) Lever, A. B. P.; Auburn, P. R.; Dodsworth, E. S.; Haga, M. Aki.; Liu, Wei.; Melnik, Milan.; Nevin, W. Andrew. Bis(Dioxolene)(Bipyridine)Ruthenium Redox Series. *J. Am. Chem. Soc.* **1988**, *110* (24), 8076–8084. https://doi.org/10.1021/ja00232a020.

(38) Lever, A. B. P.; Masui, H.; Metcalfe, R. A.; Stufkens, D. J.; Dodsworth, E. S.; Auburn, P. R. The Ground and Excited State Electronic Structures of Ruthenium Quinones and Related Species. *Coord. Chem. Rev.* **1993**, *125* (1–2), 317–331. https://doi.org/10.1016/0010-8545(93)85028-3.

(39) Haga, M.; Dodsworth, E. S.; Lever, A. B. P. Catechol-Quinone Redox Series Involving Bis(Bipyridine)Ruthenium(II) and Tetrakis(Pyridine)Ruthenium(II). *Inorg. Chem.* **1986**, *25* (4), 447–453. https://doi.org/10.1021/ic00224a013.

(40) Luna, J. A.; Spielvogel, K. D.; Loutsch, N. R.; Loria, S. M.; Weisburn, L. P.; Ringenberg, M. R.; Vlaisavljevich, B.; Keith, J. M.; Shaw, S. K.; Daly, S. R. Spectroscopic and Theoretical Studies of Ruthenium Complexes with a Noninnocent N_2 S_2 Ligand in Different Redox States. *Inorg. Chem.* **2025**, *64* (31), 15961–15979. https://doi.org/10.1021/acs.inorgchem.5c02059.

(41) Ye, S.; Sarkar, B.; Duboc, C.; Fiedler, J.; Kaim, W. The Redox Series $[M(Bpy)_2(Q)]^{n+}$, M = Ru or Os, Q = 3,5-Di- *Tert* -Butyl-N-Phenyl-1,2-Benzoquinonemonoimine. Isolation and a Complete X and W Band EPR Study of the Semiquinone States ($n = 1$). *Inorg. Chem.* **2005**, *44* (8), 2843–2847. https://doi.org/10.1021/ic048407i.

(42) Chegerev, M. G.; Arsenyeva, K. V.; Cherkasov, A. V.; Piskunov, A. V. Specific Features of EPR Spectroscopy of Organotin Compounds with Paramagnetic Ligands of the O-Iminobenzosemiquinone Type. *Russ. J. Coord. Chem.* **2020**, *46* (11), 746–755. https://doi.org/10.1134/S1070328420110019.

(43) Ray, K.; Weyhermüller, T.; Neese, F.; Wieghardt, K. Electronic Structure of Square Planar Bis(Benzene-1,2-Dithiolato)Metal Complexes $[M(L)_2]^z$ ($z = 2-, 1-, 0$; M = Ni, Pd,

Pt, Cu, Au): An Experimental, Density Functional, and Correlated Ab Initio Study. *Inorg. Chem.* **2005**, *44* (15), 5345–5360. https://doi.org/10.1021/ic0507565.

(44) Chłopek, K.; Bothe, E.; Neese, F.; Weyhermüller, T.; Wieghardt, K. Molecular and Electronic Structures of Tetrahedral Complexes of Nickel and Cobalt Containing *N,N*'-Disubstituted, Bulky *o*-Diiminobenzosemiquinonate(1−) π-Radical Ligands. *Inorg. Chem.* **2006**, *45* (16), 6298–6307. https://doi.org/10.1021/ic060242l.

(45) Boyer, J. L.; Rochford, J.; Tsai, M.-K.; Muckerman, J. T.; Fujita, E. Ruthenium Complexes with Non-Innocent Ligands: Electron Distribution and Implications for Catalysis. *Coord. Chem. Rev.* **2010**, *254* (3–4), 309–330. https://doi.org/10.1016/j.ccr.2009.09.006.

(46) Bhattacharya, S.; Pierpont, C. G. Structure and Bonding in Bis(Quinone) Complexes of Ruthenium. Synthesis and Characterization of the Ru(PPh3)2(SQ)2 (SQ = 3,5-Tert-Butylsemiquinone, Tetrachloro-1,2-Semiquinone) Series. *Inorg. Chem.* **1991**, *30* (7), 1511–1516. https://doi.org/10.1021/ic00007a017.

(47) Bhattacharya, S.; Gupta, P.; Basuli, F.; Pierpont, C. G. Structural Systematics for *o*-C_6H_4XY Ligands with X,Y= O, NH, and S Donor Atoms. *o*-Iminoquinone and *o*-Iminothioquinone Complexes of Ruthenium and Osmium. *Inorg. Chem.* **2002**, *41* (22), 5810–5816. https://doi.org/10.1021/ic025766+.

(48) Boone, S. R.; Pierpont, C. G. Charge Delocalization in Ruthenium-Quinone Complexes. Structural Characterization of Bis(Bipyridine)(3,5-Di-Fert-Butylsemiquinonato)Ruthenium(II) Perchlorate and Trans -Bis(4-Íerí-Butylpyridine)Bis(3,5-Di-Íerí-Butylquinone)Ruthenium.

(49) Gianino, J.; Brown, S. N. Highly Covalent Metal–Ligand π Bonding in Chelated Bis- and Tris(Iminoxolene) Complexes of Osmium and Ruthenium. *Dalton Trans.* **2020**, *49* (21), 7015–7027. https://doi.org/10.1039/D0DT01287D.

(50) Gorelsky, S. I.; Lever, A. B. P.; Ebadi, M. Ruthenium D-Orbital Delocalization in Bis(Bipyridine)Ruthenium Derivatives of Redox Active Quinonoid Ligands. *Coord. Chem. Rev.* **2002**, *230* (1–2), 97–105. https://doi.org/10.1016/S0010-8545(02)00094-2.

(51) Das, D.; Das, A. K.; Sarkar, B.; Mondal, T. K.; Mobin, S. M.; Fiedler, J.; Záliš, S.; Urbanos, F. A.; Jiménez-Aparicio, R.; Kaim, W.; Lahiri, G. K. The Semiquinone−Ruthenium Combination as a Remarkably Invariant Feature in the Redox and Substitution Series $[Ru(Q)_n(Acac)_{3-n}]^m$, n = 1−3; m = (−2), −1, 0, +1, (+2); Q = 4,6-Di-*Tert*-Butyl-*N*-Phenyl-*o*-Iminobenzoquinone. *Inorg. Chem.* **2009**, *48* (24), 11853–11864. https://doi.org/10.1021/ic901900g.

(52) Saha, A.; Rajput, A.; Gupta, P.; Mukherjee, R. Probing the Electronic Structure of $[Ru(L^1)_2]^z$ (z = 0, 1+ and 2+) (H_2L^1 : A Tridentate 2-Aminophenol Derivative) Complexes in Three Ligand Redox Levels. *Dalton Trans.* **2020**, *49* (43), 15355–15375. https://doi.org/10.1039/D0DT03074K.

(53) Das, D.; Mondal, T. K.; Chowdhury, A. D.; Weisser, F.; Schweinfurth, D.; Sarkar, B.; Mobin, S. M.; Urbanos, F. A.; Jiménez-Aparicio, R.; Lahiri, G. K. Valence and Spin Situations in Isomeric [(Bpy)Ru(Q′)2]n (Q′ = 3,5-Di-Tert-Butyl-N-Aryl-1,2-Benzoquinonemonoimine). An Experimental and DFT Analysis. *Dalton Trans.* **2011**, *40* (33), 8377. https://doi.org/10.1039/c1dt10609k.

(54) Hino, T.; Wada, T.; Fujihara, T.; Tanaka, K. Redox Behavior of New Ru–Dioxolene–Ammine Complexes and Catalytic Activity toward Electrochemical Oxidation of Alcohol under Mild Conditions. *Chem. Lett.* **2004**, *33* (12), 1596–1597. https://doi.org/10.1246/cl.2004.1596.

(55) Ozawa, H.; Hino, T.; Ohtsu, H.; Wada, T.; Tanaka, K. A New Type of Electrochemical Oxidation of Alcohols Mediated with a Ruthenium–Dioxolene–Amine Complex in Neutral Water. *Inorganica Chim. Acta* **2011**, *366* (1), 298–302. https://doi.org/10.1016/j.ica.2010.11.013.

(56) Wada, T.; Tsuge, K.; Tanaka, K. Syntheses and Redox Properties of Bis(Hydroxoruthenium) Complexes with Quinone and Bipyridine Ligands. Water-Oxidation Catalysis. *Inorg. Chem.* **2001**, *40* (2), 329–337. https://doi.org/10.1021/ic000552i.

(57) Verma, S.; Kar, P.; Das, A.; Ghosh, H. N. Photophysical Properties of Ligand Localized Excited State in Ruthenium(Ii) Polypyridyl Complexes: A Combined Effect of Electron Donor–Acceptor Ligand. *Dalton Trans.* **2011**, *40* (38), 9765. https://doi.org/10.1039/c1dt10266d.

(58) Burstall, F. H. 34. Optical Activity Dependent on Co-Ordinated Bivalent Ruthenium. *J. Chem. Soc. Resumed* **1936**, 173. https://doi.org/10.1039/jr9360000173.

(59) Kramer, W. W.; Cameron, L. A.; Zarkesh, R. A.; Ziller, J. W.; Heyduk, A. F. Donor–Acceptor Ligand-to-Ligand Charge-Transfer Coordination Complexes of Nickel(II). *Inorg. Chem.* **2014**, *53* (16), 8825–8837. https://doi.org/10.1021/ic5017214.

(60) Cameron, L. A.; Ziller, J. W.; Heyduk, A. F. Near-IR Absorbing Donor–Acceptor Ligand-to-Ligand Charge-Transfer Complexes of Nickel(II). *Chem. Sci.* **2016**, *7* (3), 1807–1814. https://doi.org/10.1039/C5SC02703A.

(61) Yan, H.; Wu, B.; Wei, J.; Zhang, W.-X. Insight into the Ligand-to-Ligand Charge-Transfer Process in Rare-Earth-Metal Diradical Complexes. *Inorg. Chem.* **2023**, *62* (21), 8052–8057. https://doi.org/10.1021/acs.inorgchem.3c00900.

Chapter 2: Five-coordinate Aminophenol Complexes of Ruthenium(II)

2.1. Introduction

Redox-active catecholate-type ligands (**Scheme 1.4**) bound to ruthenium ions (Ru-RALs) have engendered great interest due to the high degree of covalency granted by the similar energies of the ruthenium d-orbitals and the redox-active π* orbital of the ligands.[1–8] This allows the complexes access to multiple possible electronic configurations through resonance as depicted in **Scheme 1.5**.[3] The extent of the orbital mixing in these systems is so high that they are more accurately depicted as a delocalized 5-membered metallocycle involving the electronegative atoms bound to ruthenium and the α-carbons.[4,9,10] While the fully reduced complexes of Class D can unambiguously be described as a Ru(II) ion bound to a catecholate-type ligand, there are multiple possible oxidation state assignments for the ligand and metal for each electron transferred out of the complex. With consecutive oxidations, there are multiple possible electron configurations that require corroboration of multitude of experimental data to assign the oxidation states of the metal and ligand. Fortunately, the well-behaved electronic characteristics of Ru-RALs have made it possible to probe the oxidation states of the metal and ligand through methods such as UV-Vis, EPR, XPS, IR, Raman spectroscopy, electrochemical studies, and X-ray crystallography.[11–14] However, oftentimes the electronic state of a complex has contributions from multiple resonance forms owing to the extensive covalency between the metal and ligand, leading to an intermediate physical oxidation state that differs from the formal, integer oxidation state.[15,16] For instance, the distance between the oxygen and the α-carbon in a catecholate bound to a metal ion in a purely ionic bond decreases from 1.355, 1.285, to 1.217 Å as the ligand oxidizes from catecholate to quinone.[17] But it is not uncommon for experimentally determined bond distances to lie in between as in the case of ruthenium bis-catecholate complexes where said

bond distances are measured to be 1.32 Å.[2] Therefore, rigorous investigation of multiple experimental data in addition to computational analysis is used to identify the nature of the electronic configuration of these Ru-RALs.

The extensive fundamental studies on redox-active ligands and these electronically remarkable Ru-RAL systems that have been published since the 1970s have implied the potential for homogenous catalysis.[18–21] However, sparce publications on reactivity can be found. Tanaka et al. demonstrated electrocatalytic oxidation of alcohols using a Ru(II)-quinone-ammonia complex with an ancillary terpyridine (**Scheme 1.6**), utilizing the stability of the higher oxidation state on the metal through the catecholate.[22,23]

To create a platform that can tap into the rich and well-behaved electronic properties of the ruthenium catecholate, new five-coordinate mono-aminophenol phosphine complexes of ruthenium(II) have been designed and characterized. Phosphines were selected as ancillary ligands due to their softness, which would be ideal to match with the covalent and soft Ru-RAL moiety. The newly synthesized five-coordinate Ru-RAL platform was tested for its reactivity with small π acids.

2.2. Results

2.2.1. Synthesis and structural characterization of a Ru(^{Ph}ap)(PR$_3$)$_n$ series

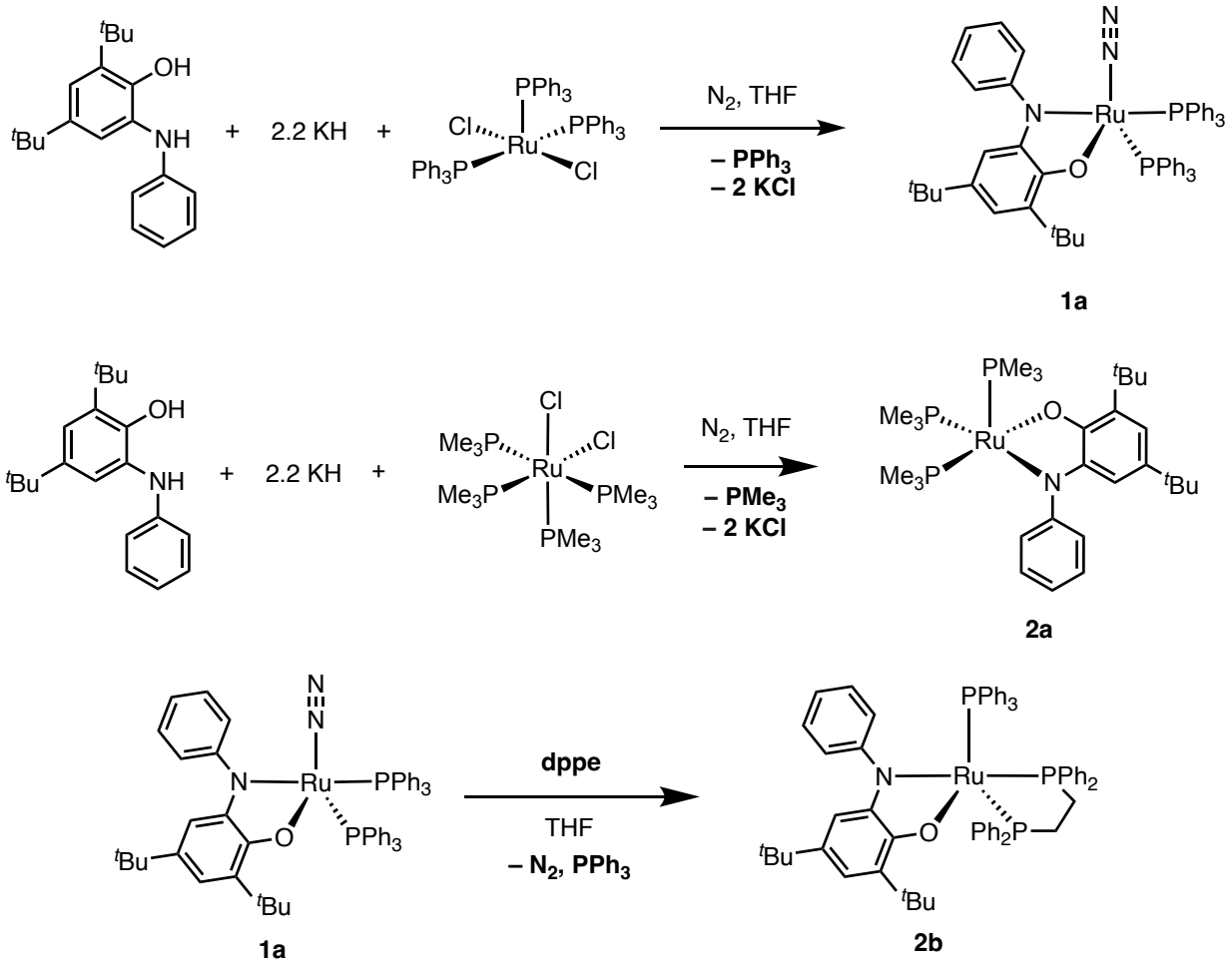

Scheme 2.1 Synthesis of ruthenium amidophenolate phosphine complexes (**1a**, **2a-b**).

Ruthenium(II) complex of the 3,5-di-*tert*-butyl-(6-phenylamidophenolate) (^{Ph}ap^{2-}) ligand was readily accessed by salt metathesis (**Scheme 2.1**). Surprisingly, single crystal X-ray diffraction and IR spectroscopy of the intended tris-phosphine complex Ru(^{Ph}ap)(PPh$_3$)$_3$ (**1b**) revealed it to be a terminally bound N_2 complex N_2Ru(^{Ph}ap)(PPh$_3$)$_2$ (**1a**) as observed by a terminal diatomic ligand and an IR absorbance at 2124 cm^{-1} presented in section 2.2.2. However, ^{1}H NMR of the isolated solids retrieved from

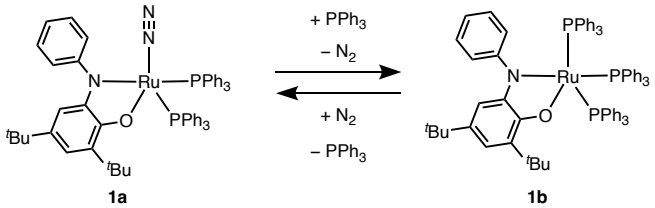

Scheme 2.2 Proposed equilibrium between **1a** and **1b** in solution state.

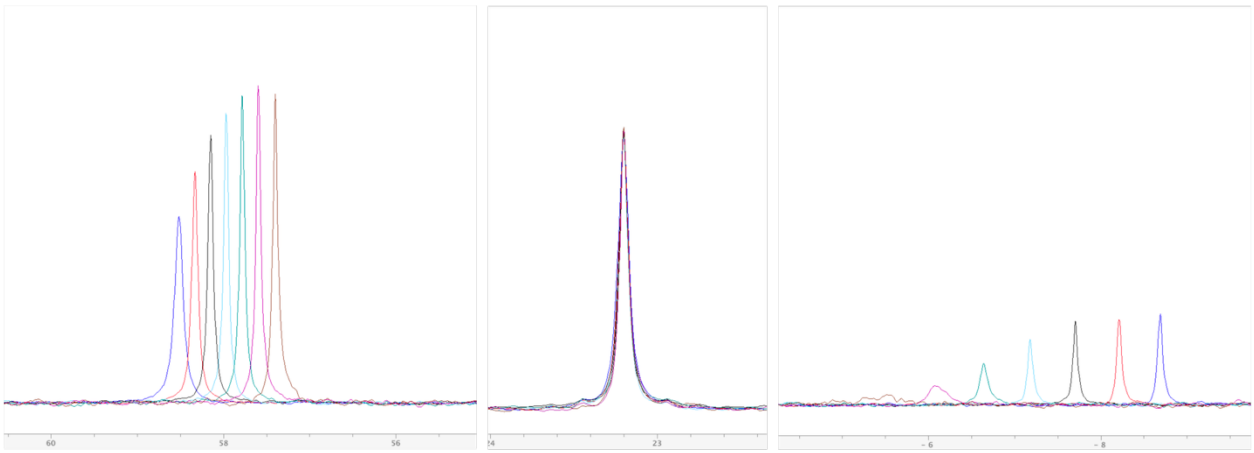

Figure 2.1 ^{31}P $\{^{1}H\}$ NMR of **1a/1b** in temperatures ranging from 20 °C (brown) to −100 °C (blue) in 20 °C increments. The peak near 58 ppm is of the metal phosphine and the peak near −7 ppm is of the free PPh_3. Triphenylphosphine oxide was added as the reference at 23.2 ppm.

recrystallization constantly displayed more than the expected 30 protons from the PPh_3 in varying degrees and a broad singlet near 5.5 ppm was sometimes observed in the ^{31}P NMR. The small impurity was suspected to be the originally intended tris-PPh_3 complex due to the extra equivalent from the ruthenium starting material. Further purification through recrystallization or solvent extraction was not successful due to the similar solubility of **1a** and PPh_3 in pentane, Et_2O, THF, benzene, and toluene, while **1a** decomposed in halogenated solvents and reacted with MeCN as discussed in section 1.2.3. In an attempt to convert all of the N_2-bound species into the PPh_3 bound species, excess triphenylphosphine was added to the recrystallized **1a** in deuterated benzene. However, the addition of up to 30 equivalents of excess PPh_3 did not lead to any chemical shift in the ^{1}H NMR. The putative equilibrium between **1a/1b** was therefore studied through low temperature (LT) ^{31}P $\{^{1}H\}$ NMR in proteo-THF with triphenylphosphine oxide added as a reference (23.2 ppm) and ^{1}H NMR in THF-d_8 between 25 to −100 °C, as presented in **Figure 2.1**. As the temperature decreased, the broad singlet near 5.5 ppm became sharper and shifted upfield, while the metal bound phosphine peak at 57.4 ppm shifted downfield as it initially sharpened near 0 °C but broadened again as the temperature decreased. Within the temperature that THF stays liquid, above −108.4

°C, the equilibrium between the suspected tris-phosphine complex **1b** and **1a** as descripted in **Scheme 2.2** is not refined to be clearly distinguished from each other. The resulting average ^{1}H NMR of the two species at 298 K is well resolved in the typical proton resonance regions and can be identified by the two characteristic *tert*-butyl singlet resonances that range from 1.4 to 1.6 ppm and a singlet resonance in the $\{^{1}H\}$ ^{31}P NMR spectrum at 57.4 ppm, suggesting that all of the ruthenium bound PPh_3 are chemically equivalent in the NMR timescale. Based on the solid-state and solution data, **1a** and **1b** appear to be five-coordinate complexes, an unusual characteristic among the many reported examples of Ru-RALs, which are predominantly 6-coordinate.

Table 2.1 Selected bond distances (Å) and angles of solid-state structures of $(N_2)Ru(^{Ph}ap)(PPh_3)_2$, $Ru(^{Ph}ap)(PMe_3)_3$, and $Ru(^{Ph}ap)(PPh_3)(dppe)$. For the five coordinate species, the two largest bond angles on the metal center are reported.

Complex	1a	2a	2b
Ru-O(1)	2.108(2)	2.0781(8)	2.0824(11)
Ru-N(1)	1.998(3)	2.0317(10)	2.0081(13)
O(1)-C(1)	1.335(4)	1.3345(14)	1.3268(18)
N(1)-C(2)	1.400(5)	1.4029(14)	1.4069(19)
C(1)-C(2)	1.411(5)	1.4177(16)	1.411(2)
C(2)-C(3)	1.401(5)	1.3975(16)	1.407(2)
C(3)-C(4)	1.380(5)	1.4001(16)	1.389(2)
C(4)-C(5)	1.413(5)	1.3916(16)	1.406(2)
C(5)-C(6)	1.381(5)	1.4055(16)	1.396(2)
C(6)-C(1)	1.421(5)	1.4131(16)	1.421(2)
Ru-P(1)	2.2937(10)	2.2825(3)	2.3030(4)
Ru-P(2)	2.2921(10)	2.2098(3)	2.2625(4)
Ru-P(3)	-	2.2798(3)	2.2499(4)
Ru-N(2)	1.929(3)	-	-
MOS	**−1.57**	**−1.76**	**−1.62**
N(1)-Ru-P(*trans*)	134.00(9)	153.47(3)	132.27(4)
O(1)-Ru-P(*trans*)	-	168.55(3)	174.84(3)
O(1)-Ru-L[b]	172.68(12)	-	-
O(1)-Ru-N(1)	79.46(11)	78.31(4)	78.70(5)
τ_5	**0.64**	**0.25**	**0.71**
Ligand cone angle	**145**	**118[a]**	**122**

(a) Tolman cone angle for dppe

To determine whether the low coordination number was driven by the sterics of the crowded ligand sphere or by electronic structure requirements of the complex, the synthesis

was repeated with smaller phosphines. The phosphine ligands chosen were due to the smaller Tolman cone angle than PPh_3.[24] The phosphines of choice were PMe_3 and dppe with the Tolman cone angle of 118 ° and 122 °, compared to the 145 ° of PPh_3. For the PMe_3 variant, analogous synthesis was performed with the precursor $Ru(PMe_3)_4Cl_2$. To install dppe, an equivalent of the ligand was added to **1a** and the product was isolated by recrystallization in cold pentane. The resulting complexes were $Ru(^{tBu}ap)(PMe_3)_3$ (**2a**) and $Ru(^{tBu}ap)(PPh_3)$(dppe) (**2b**). The complexes display well resolved resonances in the diamagnetic region of ^1H NMR and ^{31}P $\{^1H\}$ NMR. **2a** can be identified by its phosphorus resonance at 17.94 ppm and **2b** displays a triplet for the PPh_3 at 57.31 ppm and a doublet of doublets at 59.76 ppm.

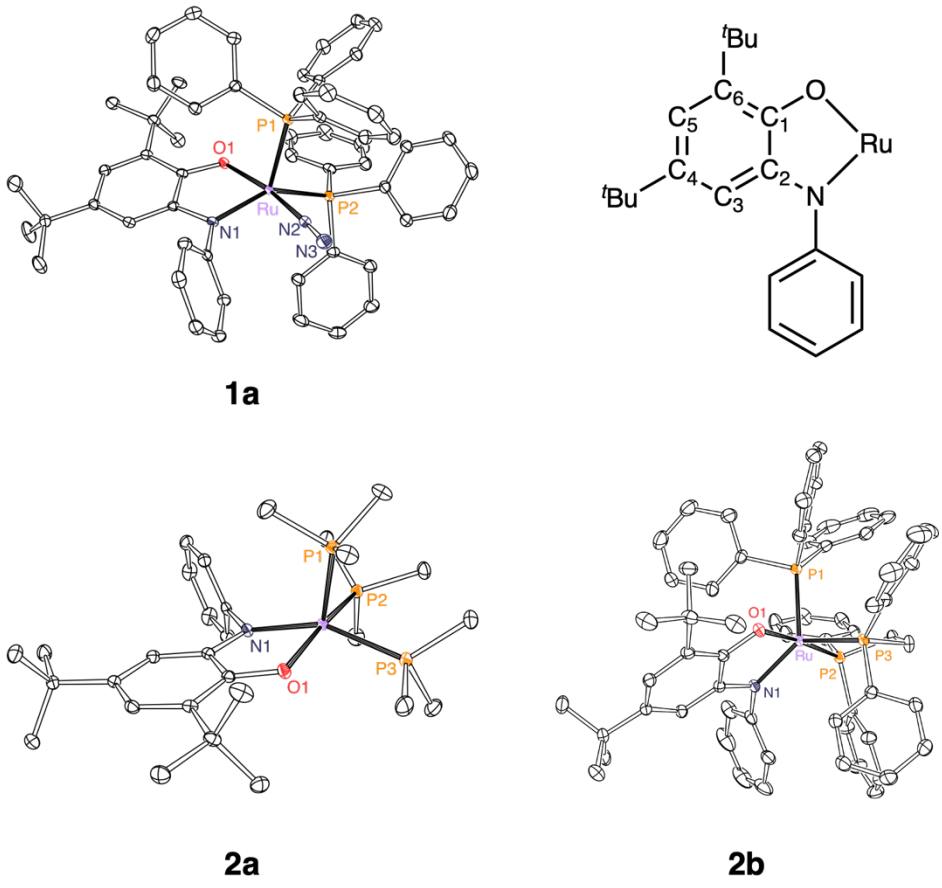

Figure 2.2 Solid-state structure of $N_2Ru(^{Ph}ap)(PPh_3)_2$, $Ru(^{Ph}ap)(PMe_3)_3$, and $Ru(^{Ph}ap)(dppe)(PPh_3)$ with thermal ellipsoids set at 50 % probability. Hydrogen atoms and solvent molecules are omitted for clarity.

Single-crystal X-ray diffraction methods were used to probe the molecular structures and to gain insight on the metal and ligand oxidation states in each complex. Selected bond metrics, bond angles, and τ_5 values for complex **1a**, **2a**, and **2b** are presented in **Table 2.1** and the ORTEP diagram in **Figure 2.2**. X-ray quality crystals were harvested from concentrated pentane or diethyl ether solutions cooled to −35 °C, or from a pentane/THF diffusion. From the mixture of **1a** and **1b** in pentane, only **1a** was isolated as X-ray quality single crystals. **2a** and **2b** retained all three phosphines as the ancillary ligand. The geometry of the complexes is closely tied to sterics, with τ_5 values increasing in correlation to the Tolman cone angle of the phosphine ligand (**Table 2.1**). As the cone angle increases from 118 ° (**2a**, PMe_3) to 145 ° (**1a**, PPh_3), the complex assumes a more trigonal bipyramidal structure, while the fixed bite angle of the chelating dppe forces the structure of **2b** to be closer to trigonal bipyramid.

It is established that Ru-RALs often demonstrate intermediate metal and ligand oxidation states due to the high covalency between the two. To aid in the assignmenmt of the metal and ligand oxidation state, the metrical oxidation states (MOS) of the redox-active aminophenol for each complex were calculated by comparing the bond length of the ligand to the compiled literature of structural data of metal aminophenol complexes.[17] The calculated MOS are non-integer values between −1.44 and −1.86 as expected from formally $Ru^{II\text{-}tBu}ap^{2-}$ complexes due to the high degree of covalency between the ligand and the metal. The MOS of the amidophenolate increased as the alkyl groups on the phosphines were substituted with the phenyl groups (**2a<2b<1a**).

2.2.2. Spectroscopic analysis

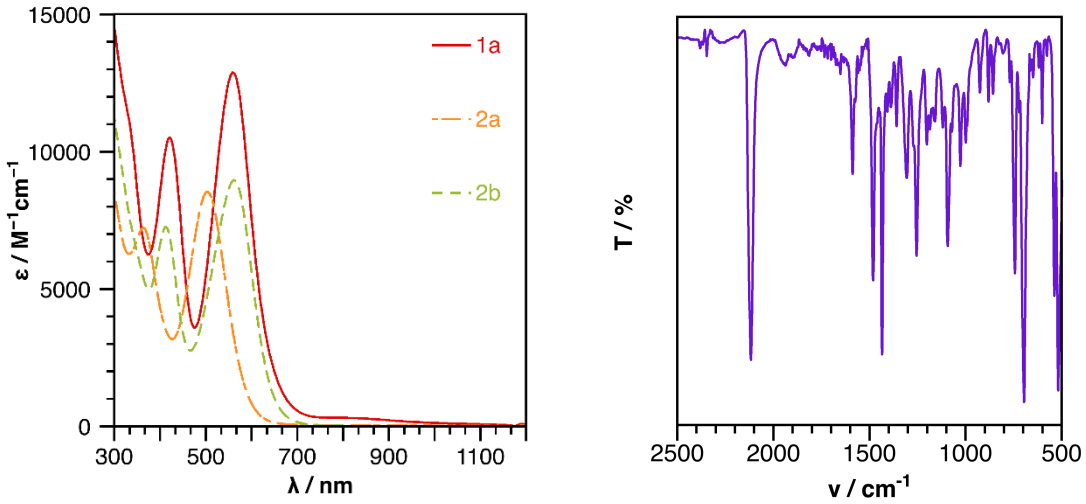

Figure 2.3 UV-visible spectra of **1a** and **2a-b** (left) and IR spectra of 1a (right).

The ruthenium amidophenolate phosphine complexes have been characterized through electronic absorbance spectroscopy in the UV-vis-NIR region in THF at 298K, and **1a** was also characterized through IR spectroscopy as a KBr pellet (**Figure 2.3**). The wavelength and extinction coefficients of the absorbance features for the UV-vis are summarized in **Table 2.2**. The complexes display two absorbance peaks, one between 360 to 480 nm (2.6 to 3.4 eV) and another between 500 to 580 nm (2.1 to 2.5 eV). **1a** also showed a prominent absorption peak in the IR region at 2124 cm^{-1}, which is consistent with Ru(II) bound terminal dinitrogen.[25,26]

Table 2.2 UV-vis-NIR transition of complexes **1-5** in THF.

λ / nm (ε / $M^{-1}cm^{-1}$)		
1a	**2a**	**2b**
421 (9700)	363 (7500)	473 (7300)
560 (12000)	503 (7600)	561 (9100)

2.2.3. Electrochemical analysis of 1a

Electrochemical studies were performed to probe the accessible oxidation states of the complex. Voltammetric experiments were performed with 1.0 mM analyte and 0.1 M $[Bu_4N][PF_6]$ electrolyte concentration with a glassy carbon working electrode, platinum wire counter electrode, and $Ag^{+/0}$ pseudo-reference electrode under N_2 atmosphere at 298K. When **1a** was dissolved in MeCN for cyclic voltammetry studies, a reaction between the complex and the solvent was observed as two new peaks grew within the timeframe of data collection. Therefore, electrochemistry of **1a** is reported in THF. The product of the reaction between **1a** and MeCN was isolated as the ligand substituted complex $(MeCN)Ru(^{Ph}ap)(PPh_3)_2$ (**3**). Electrochemistry for complex **3** was more well-behaved in MeCN compared to THF as the solvent. For both **1a** and **3**, three redox couples have been observed between the range of −3 and 1 V. The first feature at −2.5 V for both complexes appear in the more negative region compared to the open circuit potential. The next event is found past the open circuit potential, at −0.39 V for **1a** and −0.83 V for **3**. The last peak appears at 0.13 V for **1a**, and −0.19 V for **3**

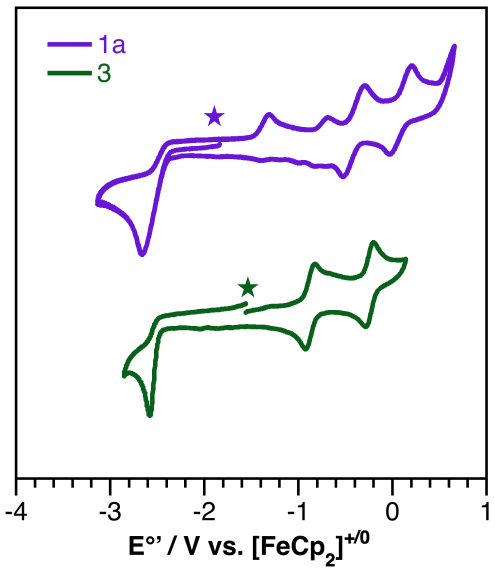

Figure 2.4 Cyclic voltammograms of **1a** in THF (purple) and **3** in MeCN (green) at 200 mV/s. Star indicates the open circuit potential.

which is the only reversible event where i_{pa}/i_{pc} is near unity and i_{pa} and i_{pc} are both directly proportional to the square root of the scan rate.

Table 2.3 Reduction potentials from cyclic voltammetry experiments for **1a** and **3** in THF and MeCN, respectively at 200 mV/s. All values are referenced to the $[FeCp_2]^{+/0}$ internal standard redox couple.

	$E^{\circ\prime}$ / V vs. $[FeCp_2]^{+/0}$ (i_{pa}/i_{pc})		
1a	−2.50	−0.39 (3.79)	0.13 (1.97)
3	−2.48	−0.83 (1.78)	−0.19 (1.02)

2.2.4. Theoretical calculations

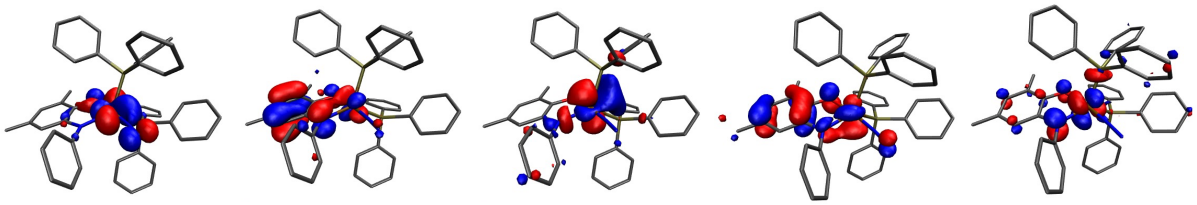

Figure 2.5 Kohn-Sham representations of the HOMO−3 to LUMO of **1a** (left to right). (iso = 0.045)

Density functional theory (DFT) calculations of **1a** were performed in Gaussian 16 to investigate the electron distribution over the ^{Ph}ap and metal center. The *tert*-butyl groups of the solid structure were substituted to hydrogen atoms to minimize computational load and final geometry optimizations, and energy calculations were carried out using B3P86 functional with def2TZVP basis set. The bond metrics obtained from the optimized geometry and thermodynamic frequency calculations were within 0.04 Å with the experimental structural data for the metal-heteroatom bond distances, and within 0.02 Å for the intraligand bond distances. Mulliken population analysis yielded the atomic charge distributions for the frontier molecular orbitals (FMOs), which is presented in **Table 2.4**. The Kohn-Sham diagram of the same FMOs are presented in **Figure 2.5**.

Table 2.4 Mulliken population analysis distributions for selected FMOs of **1a**.

	M / %	N(^{Ph}ap) / %	O / %	C(^{Ph}ap) / %	P / %
LUMO	33.9	10.0	4.4	11.4	11.7
HOMO	20.2	4.3	14.0	39.9	1.9
HOMO−1	50.0	7.5	3.6	7.0	10.4
HOMO−2	14.5	13.5	4.5	48.7	3.0
HOMO−3	64.6	0.0	10.3	1.1	2.5

2.2.5. Reactivity with small molecules

Inspired by the reactivity studies of the previously reported OPDA analogue of **1b**, **1a** was subjected to ligand replacement studies with a list of small molecules with varying π acid strength according to **Scheme 2.3**.[9] As found during a cyclic voltammetry study, addition of excess MeCN to **1a** results in ligand substituted product, **3**. The acetonitrile-bound complex can be independently synthesized by adding excess MeCN after the salt metathesis step as well. Complex **3** was characterized through the well resolved proton spectra in ^{1}H NMR in the diamagnetic region and ^{31}P NMR signal at 65.11 ppm. Addition of 1 atmosphere of carbon monoxide to complex **1a** yields both five-coordinate monocarbonyl (CO)Ru(^{tBu}ap)(PPh_3)$_2$ (**4a**) and the six-coordinate dicarbonyl (CO)$_2$Ru(^{tBu}ap)(PPh_3)$_2$ (**4b**) complexes. The dicarbonyl product can be isolated from a chilled pentane solution of the crude mixture as purple crystals, while the monocarbonyl product can be separately synthesized as depicted in **Scheme 2.3**, by adding an excess of paraformaldehyde as a carbonyl source in benzene through the dehydrogenation of formaldehyde.[27] Both complexes can be identified through the set of *tert*-butyl singlet resonances in ^{1}H NMR at around 1.3 to 1.6 ppm, and through the characteristic CO stretching absorption near 1940 cm^{-1} in the IR region. Both equivalents of CO binding seem to be reversible, as observed from the regeneration of **1a** under an atmosphere of N_2 in solution monitored by ^{1}H NMR.

Even weaker π-acids can also replace L when added in sufficient amounts, as evidenced by the generation of ethylene bound $(C_2H_4)Ru(^{tBu}ap)(PPh_3)_2$ (**5**) complex when **1a** is exposed to 1 atmosphere of ethylene after three freeze-pump-thaw cycles. The resulting complex can be isolated as purple crystals from chilled pentane solution and can be characterized by the shift of the aliphatic proton signal to 1.35 and 1.57 ppm as well as the appearance of the bound C_2H_4 observed as a broad singlet at 2.70 ppm in the ^1H NMR. As

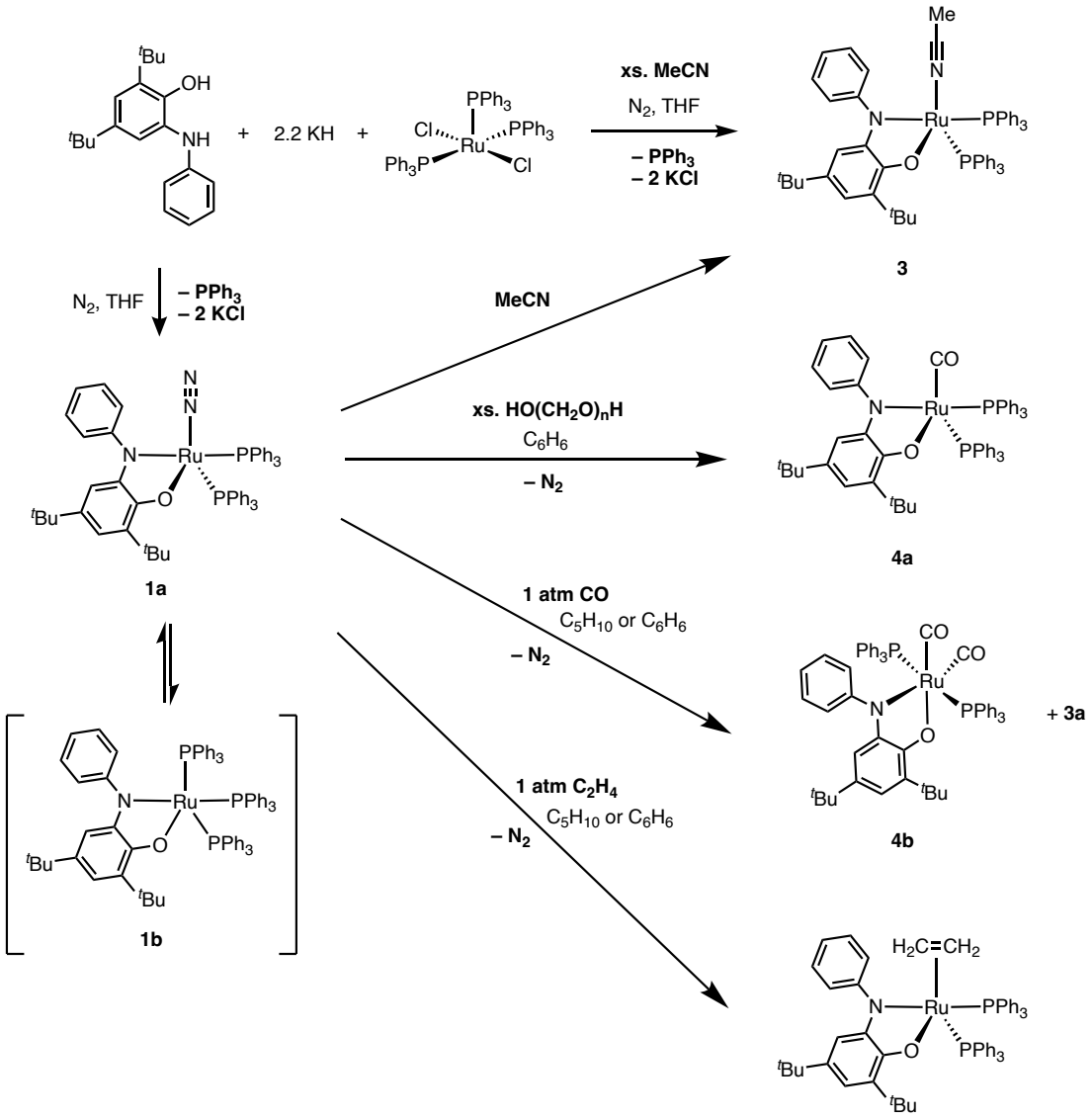

Scheme 2.3 Synthesis of $(L)_nRu(^{Ph}ap)(PPh_3)_2$ (L = N_2, MeCN, CO, C_2H_4).

with the carbonyl complexes, the binding of ethylene is reversible and **1a** is regenerated under N_2 atmosphere.

All complexes but **4b** in the $(L)_nRu(^{Ph}ap)(PPh_3)_2$ series were five-coordinate, where the six-coordinate dicarbonyl complex assumed an octahedral geometry with *trans*-phosphines. In the five-coordinate complexes, the phosphines are oriented *cis* to each other while the aminophenol is always oriented so that the phenol is *trans* to the L regardless of its identity. The calculated MOS for the amidophenolates were in between −1 and −2, similar to the phosphine series. The intermediate MOS values suggested significant electron density donation into the metal from the π system of the ligand to the d-orbitals, which could then be used to backbond into the π acids. However, the bond distance within the π acid ligands were

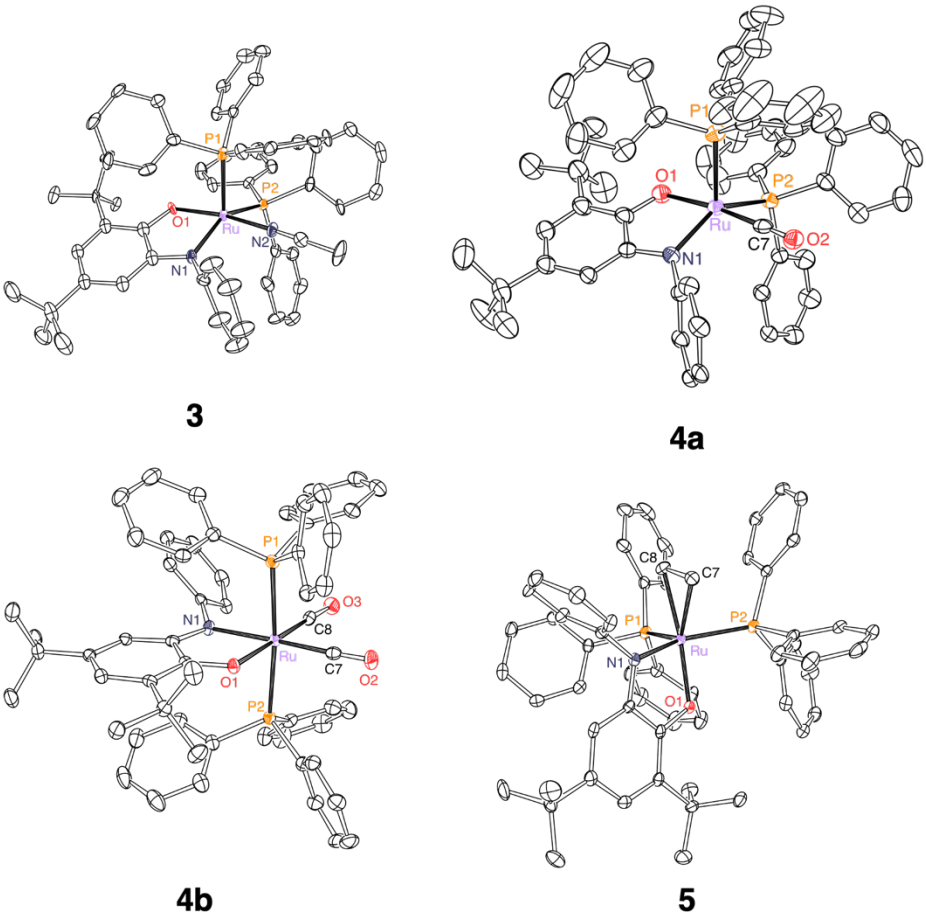

Figure 2.6 ORTEP diagram of $(L)_nRu(^{Ph}ap)(PPh_3)_2$ with thermal ellipsoids set at 50 % probability. Hydrogen atoms and solvent molecules are omitted.

not significantly different from their "free" states. The distance between the nitrogens in the N_2 ligand of **1a** was 1.110 Å, which is comparable to a triple bond in the free dinitrogen molecule of 1.098 Å.[28] Similarly, the carbonyl C-O bond lengths in **4a** and **4b** are 1.169, 1.139, and 1.142 Å, while free carbon monoxide bond length is 1.128 Å. The C-C bond length within acetonitrile in **3**, and C-C bond length of the bound ethylene in **5** are 1.472 Å and 1.397 Å respectively, which is only slightly elongated from 1.458 Å[29] and 1.339 Å[30] reported for acetonitrile and ethylene.

Table 2.5 Selected bond distances (Å) and angles of solid-state structures of $(L)_nRu(^{Ph}ap)(PPh_3)_2$ (L = N_2, MeCN, CO, C_2H_4). For the five coordinate species, the two largest bond angles on the metal center are reported.

Complex	1a	3[a]	4a	4b	5
Ru-O(1)	2.108(2)	2.052	2.058(3)	2.0543(11)	2.0532(11)
Ru-N(1)	1.998(3)	1.984	2.019(3)	2.0924(14)	2.0098(13)
O(1)-C(1)	1.335(4)	1.333	1.319(5)	1.3576(19)	1.3313(17)
N(1)-C(2)	1.400(5)	1.390	1.390(5)	1.403(2)	1.3835(19)
C(1)-C(2)	1.411(5)	1.420	1.414(6)	1.413(2)	1.421(2)
C(2)-C(3)	1.401(5)	1.396	1.403(6)	1.394(2)	1.406(2)
C(3)-C(4)	1.380(5)	1.388	1.381(6)	1.390(2)	1.384(2)
C(4)-C(5)	1.413(5)	1.398	1.393(7)	1.396(2)	1.406(2)
C(5)-C(6)	1.381(5)	1.405	1.387(6)	1.393(2)	1.396(2)
C(6)-C(1)	1.421(5)	1.418	1.418(6)	1.407(2)	1.421(2)
Ru-P(1)	2.2937(10)	2.240	2.3019(10)	2.4188(5)	2.3315(5)
Ru-P(2)	2.2921(10)	2.294	2.3255(10)	2.4488(5)	2.3214(5)
Ru-P(3)	-	-	-	-	-
Ru-L(1)[b]	1.929(3)	1.993	1.841(5)	1.8922(17)	2.2012(16) 2.1731(16)
Ru-L(2)[b]	-	-	-	1.8854(17)	-
MOS	**−1.57**	**−1.63**	**−1.52**	**−1.86**	**−1.44**
N(1)-Ru-P(*trans*)	134.00(9)	143.23	140.68(10)	-	149.72(4)
O(1)-Ru-P(*trans*)	-		-	-	-
O(1)-Ru-L[b]	172.68(12)	171.25	170.15(15)	-	142.83(5)[c]
O(1)-Ru-N(1)	79.46(11)	79.36	77.99(13)	79.85(5)	
τ_5	**0.64**	**0.47**	**0.49**	-	**0.11[c]**

(a) Preliminary structure
(b) L represents the atom from the L bound to Ru.
(c) The ethylene carbon closer to the oxygen was used.

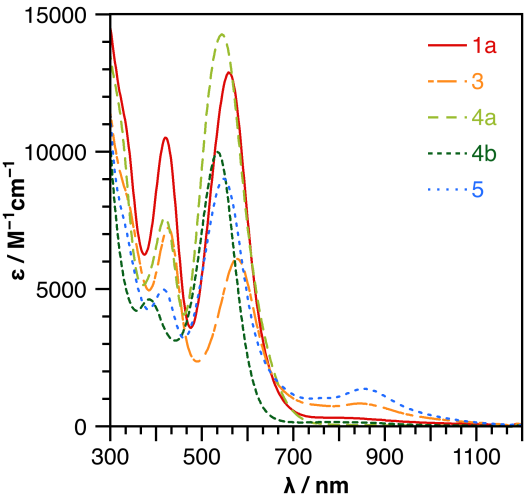

Figure 2.7 UV-visible spectra of $(L)_nRu(^{Ph}ap)(PPh_3)_2$ (L = N_2, CO, $(CO)_2$, MeCN, C_2H_4) in THF.

The electron absorption spectroscopy of the π acid series show a similar pattern to the phosphine series as presented in **Figure 2.7** and **Table 2.6**. There are two major absorbances near 400 and 550 nm (3.10 and 2.25 eV) which are assigned as Ru(d)-^{Ph}ap(π) π to Ru(d)-^{Ph}ap(π) π* identical to the phosphine complexes. For complexes **3** and **5**, low energy transitions at low absorbances were observed. The transitions could be artifact of oxidized impurities due to the air sensitivity of the complexes. However, there is a possibility that those transitions are charge transfers from mixed metal and RAL into the L ligand.

Table 2.6 UV-vis-NIR transition of $(L)_nRu(^{Ph}ap)(PPh_3)_2$ (L = N_2, CO, $(CO)_2$, MeCN, C_2H_4) in THF.

λ / nm (ε / $M^{-1}cm^{-1}$)				
1a	**3**	**4a**	**4b**	**5**
421 (9700)	426 (3800)	419 (7700)	385 (4700)	416 (4700)
560 (12000)	576 (3200)	544 (13000)	535 (9900)	548 (9000)

2.3. Discussion

2.3.1. Determination of the oxidation states of the ligand and metal

The oxidation states of the ligand and metal can be inferred through charge balance as the complexes above belong in Class D (Ru^{II}-ap^{2-}). The designation of the oxidation states was corroborated through its solid-state structure as well as spectroscopic and electrochemical measurements. From the solid-state structures, the MOS of the ligand is calculated to be intermediate between −1.86 and −1.44. The fractional values are expected from the high covalency between the metal and the ligand, which would delocalize the electron density of the fully reduced ligand over the metal. The increased covalency between the metal and ^{Ph}ap is observed in the theoretical calculations as well, as the Mulliken population analysis shows that HOMO has contributions from both the ruthenium (20.2 %) and ^{Ph}ap (58.2 %).

UV-Visible spectra of metal complexes with catecholate type ligands can be used to identify the ligand oxidation state. In most of the complexes above, two peaks were observed that could be most accurately characterized as Ru-^{Ph}ap π to Ru-^{Ph}ap π* transitions commonly observed in other Ru-RAL systems. The absence of the easily distinguishable intraligand low energy high intensity (λ > 800 nm, ε > 10,000 $M^{-1}cm^{-1}$) transition rules out the possibility of Class B or C systems.

The electrochemical measurements for the dinitrogen complex **1a** and the acetonitrile complex **3** suggest that the significantly negative and irreversible event near −2.5 V is most likely a metal reduction that involves an irreversible chemical change. The other two oxidations that are anodic to the open circuit potential are assigned as the oxidation of the complex from a Class D to Class C (−0.39 for **1a** and −0.83 for **3**) and a subsequent oxidation from Class C to Class B (0.13 for **1a** and −0.19 for **3**). Other than the difference in the solvent

that the measurement was taken in, the shift in the potential of the oxidation events between **1a** and **3** may come from the change in the coordination environment of the oxidized species. As the complex lose electron density, it may be more stabilized by acquiring another equivalent of ligand from the solvent. The smaller size of MeCN could be kinetically advantageous in coordinating to the metal center compared to THF. The slower binding of THF could also explain the smaller events observed for **1a** near −1.3 and −0.8 V, which may be the oxidations to a five-coordinate unstable Class C and Class B complexes, while the more well-behaved events are between the six-coordinate THF-bound species. The open circuit potential lies before the first reversible event, meaning that the bulk complexes of **1a** and **3** exist as the fully reduced Class D state.

2.3.2. Replacing phosphines to determine the effects of sterics

The proposed equilibrium of **1a**/**1b** suggests that the sterics applied from the bulky triphenylphosphines is enough to displace the third phosphine and replace it with a dinitrogen from the atmosphere. Complex **1a** also stays five-coordinate in an intermediate geometry between trigonal bipyramidal and square pyramidal in solid-state. In solution, both **1a** and **1b** seem to be in fluxional five-coordinate geometry in room temperature in the NMR timescale as evidenced by the metal phosphine singlet in the ^{31}P NMR. Even though the solid-state structure shows that there is an open coordination site *trans*- to one of the phosphines, the Ru^{II}-*tBu*ap^{2-} complex stays five-coordinate. This is likely due to the enhanced covalency between the metal and the amidophenolate ligand that result in a higher electron density around the metal that prevents the occupation of the sixth coordination site. This effect has been explained as an electron configuration closer to 18e$^-$ due to the bond order of Ru-N and Ru-O being higher than 1, supported by their shorter bond distance in the solid state.[9]

For a d^6 electron configuration on the metal, square planar geometry is expected to be more stable compared to trigonal bipyramid as the electrons fill the d_{xz}, d_{yz}, and d_{xy} orbitals in a closed shell configuration. Therefore, complex **2a** crystalizes out the closest to square planar geometry with a τ_5 value of 0.25 owing to the small cone angle of PMe_3. The added bulk from the phenyl substituents on dppe and PPh_3 further pushes the complex into intermediate geometry with τ_5 value of 0.64 for **1a**. Lastly, the fixed bite angle of the chelating dppe ligand locks the complex in a geometry closer to trigonal bipyramid in complex **2b**, with a τ_5 value of 0.71.

The phosphines are oriented *cis* to each other while the aminophenol is always oriented so that the phenol is *trans* to the axial L regardless of its identity. It seems that there is a Ru-L π interaction apparent from the Kohn-Sham diagram of the HOMO−3 of **1a** which prefers the weak acid L to be *trans* to the phenol even with the cost of arranging the bulky phosphines *cis* to each other.

2.3.3. Ancillary ligand replacement

The equilibrium between **1a** and **1b** suggested that the apical ligand could be substituted easily, which would be beneficial for potential reactivity. Small π acids of different strength were able to readily displace the apical ligand to generate complexes **3-5** when added in excess as previously demonstrated by a similar five-coordinate ruthenium(II) o-phenylenediamine phosphine complex.[9] Of the π acids that were added, only CO generated a mixture of five-coordinate mono- and six-coordinate dicarbonyl species, suggesting the back-donation into the carbonyl was strong enough to relieve the electron density from the ligand to form the octahedral geometry without a formal oxidation.

2.4. Conclusion

A series of five-coordinate ruthenium amidophenolate complexes were synthesized and characterized. Spectroscopic, electrochemical, and solid-state bond metric evidence led to the assignment of these complexes as formally Class D ($Ru^{II\text{-}Ph}ap^{2-}$) Ru-RALs with increased covalency between the metal and the amidophenolate ligand. Replacement of the ancillary phosphines revealed that less bulky phosphines allowed the solid-state structure of the complex to form the more energetically stable square pyramidal geometry. Due to the high electron density on the metal, the complexes stayed five-coordinate across different phosphine analogues. The liability of the weak π acid ligand was documented through replacement with other π acids, albeit no activation of the π acids were observed. The well-behaved electronic properties make these Class D ruthenium amidophenolate series good candidates for reactivity.

2.5. Experimental

General Considerations. All manipulations were carried out using standard Schlenk-line techniques and glovebox techniques under nitrogen. Hydrocarbon and ethereal solvents were sparged with argon before being deoxygenated and dried through activated Q5 and alumina columns. Such solvents were stored over activated molecular sieves in the glovebox. Deuterated solvents were dried over calcium hydride, distilled, and freeze-pump-thawed to remove dioxygen. Potassium hydride was obtained in mineral oil and washed with pentane prior to use. Tetrabutylammonium hexafluorophosphate (Acros) was recrystallized from ethanol three times and dried under vacuum before use. Ferrocene (Acros) was purified by vacuum sublimation. Tris(triphenylphosphine)ruthenium (II) dichloride (Sigma), carbon monoxide (Airgas), and ethylene (Airgas) was used as received. 4,6-di-tert-butyl-2-(phenylamino)phenol was prepared according to published procedures.[31]

Spectroscopic and Electronic Characterization. All NMR spectroscopy was performed on a Bruker Avance 400, 500, or 600 MHz spectrometer at 298K. ^{1}H NMR spectra were referenced to residual proteo impurities of the solvents (7.16 ppm, C6D6). ^{13}C NMR spectra were referenced to TMS using the natural ^{13}C abundance of the solvent. ^{31}P {^{1}H} NMR were referenced with a phosphoric acid external standard (85%, 0.00 ppm). All chemical shifts are reported using the standard notation in parts-per-million with positive shifts to higher frequency from given reference. Electronic absorption spectra were recorded using a PerkinElmer Lambda 800 absorption spectrometer and Jasco V-670 using 10 mm quartz cuvettes at ambient temperatures.

Cyclic voltammetry and differential pulse voltammetry experiments were performed on a Gamry G300 potentiostat/galvanostat/Zero Resistance Ammeter (Gamry Instruments, Warminster, PA) using a 3.0 mm glassy carbon working electrode, a platinum wire counter electrode, and a silver wire pseudo-reference electrode. Experiments were performed at

ambient temperature in a dry nitrogen glovebox with 1 mM analyte and 100 mM $[NBu_4][PF_6]$ supporting electrolyte. All potentials were referenced to $[FeCp_2]^{+/0}$ using ferrocene as an internal standard.

Crystallographic Measurements. X-ray diffraction data were collected on single crystals mounted on glass fiber loops using a Bruker D8 Advance Photon III or a Bruker CCD platform diffractometer at 143K using Mo Kα (λ = 0.71073 Å) radiation, which was wavelength selected with a single-crystal graphite monochromator. A full sphere of data was collected for each crystal structure. The SMART program package was used to determine unit-cell parameters and to collect data. The raw frame data were processed using SAINT[32] and SADABS[33] to yield the reflection data files. Subsequent calculations were carried out using the SHELXTL[34] program suite. Structures were solved by direct methods and refined on F^2 by full-matrix least-squares techniques to convergence. Analytical scattering factors for neutral atoms were used throughout the analyses. Hydrogen atoms, though visible in the difference Fourier map, were generated at calculated positions and their positions refined using the riding model. ORTEP diagrams were generated using ORTEP-3 for Windows.[35] Bond distances were extracted in Mercury for Windows.

Theoretical Calculations. Density functional theory calculations were performed using Gaussian 16[36] employing B3P86 exchange-correlation functional with def2TZVP basis set. All calculations were performed as closed-shell singlets. Geometries were optimized from the solid-state data of each complex. Molecular orbital compositions and atomic charges were calculated using Mulliken population analysis.

Synthesis.

Synthesis of $(N_2)Ru(^{Ph}ap)(PPh_3)_2$ (**1a**)

In a 50 mL round bottom flask, $^{Ph}apH_2$ (0.062 g, 0.21 mmol, 1 equiv.) was dissolved in 10 mL of THF. Potassium hydride (0.019 g, 0.48 mmol, 2.3 equiv.) was added and the reaction was stirred in ambient temperature for 1 hour. The bright yellow solution was filtered over a frit onto a solution of tris(triphenylphosphine)ruthenium (II) dichloride (0.20 g, 0.21 mmol, 1 equiv.) in 20 mL THF. The reaction was stirred in ambient temperature for 2 hours. The solvent was removed in vacuo, then the product was extracted with pentane and filtered through a frit equipped with Celite. The product was recrystallized from chilled pentane solutions to yield deep purple needles in 20% yield. (0.040 g). ^{1}H NMR (C_6D_6, 400 MHz) δ/ppm: 1.47 (s, 9H, $C(CH_3)_3$), 1.48 (s, 9H, $C(CH_3)_3$), 6.91 (m, 23H, aryl-H), 7.33 (m, 16H, aryl-H). $^{31}P\{^{1}H\}$ NMR (500MHz) δ/ppm: 59.07 (s, PPh_3). ^{13}C NMR (400MHz) δ/ppm: 135.8 (aryl–C), 135.6 (aryl–C), 133.9 (aryl–C), 129.2 (aryl–C), 128.7 (aryl–C), 126.1 (aryl–C), 124.2 (aryl–C), 116.2 (aryl–C), 34.9 (CH_3), 34.4 (CH_3), 32.1 (CH_3), 30.3 (CH_3) ppm. FTIR (KBr) ν/cm^{-1} 2124. UV-vis (THF) λ_{max} / nm (ε / M^{-1} cm^{-1}): 422 (8900), 564 (12000).

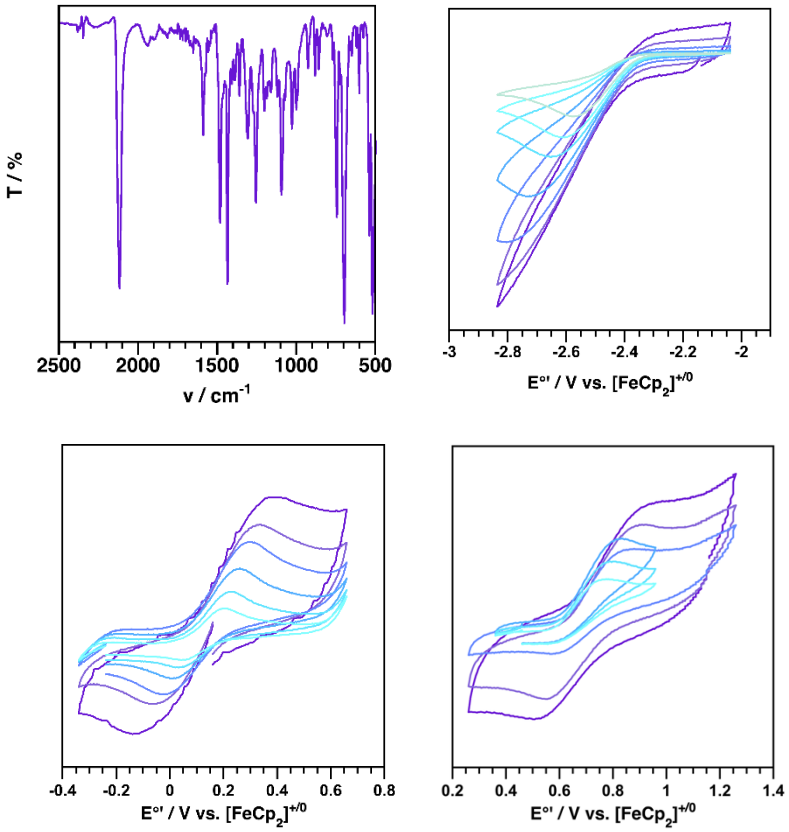

Figure 2.8 IR spectrum of **1a** in KBr (top left) and scan rate dependence of **1a** in THF.

Synthesis of Ru(^{Ph}ap)(PMe_3)$_3$ (**2a**)

In a 20 mL scintillation vial, $^{Ph}apH_2$ (0.065 g, 0.22 mmol, 1 equiv.) was dissolved in 10 mL THF. To it, KH (0.030 g, 0.75 mmol, 3.4 equiv.) was added at once. The suspension was stirred in room temperature for 1.5 hours. The resulting yellow solution was filtered into a vial with RuCl2(PMe3)4 (0.104 g, 0.22 mmol, 1 equiv.) The solution changed to brown. The resulting solution was stirred in room temperature for 2 hours before solvent was removed in vacuo. The product was extracted with 10 mL Et2O which was concentrated down to a solid (0.077g, 56 % yield). (C_6D_6, 400 MHz) δ/ppm: 0.95 (br s, 27H, $P(CH_3)_3$), 1.38 (s, 9H, $C(CH_3)_3$), 1.93 (s, 9H, $C(CH_3)_3$), 6.66 (d, 1H, aryl-H), 7.17-7.30 (m, 5H, aryl-H). $^{31}P\{^1H\}$ NMR

(500MHz) δ/ppm: 17.94 (br s, PMe_3). UV-vis (THF) λ_{max} / nm (ε / M^{-1} cm^{-1}): 363 (7500), 503 (7600).

Synthesis of Ru(^{Ph}ap)(PPh_3)(dppe) (**2b**)

In a 20 mL scintillation vial, **1a** (0.15 g, 0.16 mmol, 1 equiv.) was dissolved in 10 mL THF. To it, 1,2-bis(diphenylphosphino)ethane (0.06 g, 0.16 mmol, 1 equiv.) was added. The solution was stirred in ambient temperatures overnight. The solvent was removed *in vacuo* and the product was extracted with 18 mL pentane, filtered over filter paper, and chilled to –40 °C overnight to yield purple solids (0.10 g, 58% yield). (C_6D_6, 400 MHz) δ/ppm: 1.40 (s, 9H, $C(CH_3)_3$), 1.42 (s, 2H, CH_2), 1.73 (s, 9H, $C(CH_3)_3$), 2.02 (s, 2H, CH_2), 6.67-7.03 (m, aryl-H), 7.39-7.50 (m, aryl-H). $^{31}P\{^1H\}$ NMR (500MHz) δ/ppm: 57.31 (t, $^2J_{PP}$ = 34.1 Hz, PPh_3), 59.76 (d, $^2J_{PP}$ = 35.0 Hz, dppe). UV-vis (THF) λ_{max} / nm (ε / M^{-1} cm^{-1}): 413 (7300), 561 (9100).

Synthesis of (MeCN)Ru(^{Ph}ap)(PPh_3)$_2$ (**3**)

I. Synthesis from $Ru(PPh_3)_3Cl_2$

In a 20 mL scintillation vial, $^{Ph}apH_2$ (0.063 g, 0.21 mmol, 1 equiv.) was dissolved in 10 mL of THF. Potassium hydride (0.035 g, 0.86 mmol, 4 equiv.) was added and the reaction was stirred in ambient temperature for 1 hour. The bright yellow solution was filtered over a frit onto a solution of tris(triphenylphosphine)ruthenium (II) dichloride (0.20 g, 0.21 mmol, 1 equiv.) in 5 mL THF. MeCN (1mL, 0.02 mol, 90 equiv.) was added. The solution turned dark green. The reaction was stirred in ambient temperature for 1.5 hours. The solvent was removed in vacuo. The product was washed with pentane to remove excess PPh_3. The remaining dark solids were extracted with Et2O and filtered through Celite to remove KCl. Solvent was removed under vacuum to yield dark brownish green solids in 91% yield.

II. Synthesis from **1a**

In a 20 mL scintillation vial, **1a** (0.21 g, 0.22 mmol, 1 equiv.) was dissolved in MeCN (2 mL, 40 mmol, 200 equiv.). The solution was stirred overnight in ambient temperature. Volatiles were removed in vacuo to afford dark blue solids in 98% yield (0.21 g). X-ray quality crystals were grown from chilled pentane solutions. ^{1}H NMR (C_6D_6, 400 MHz) δ/ppm: 0.39 (s, 3H, MeCN), 1.56 (s, 9H, $C(CH_3)_3$), 1.60 (s, 9H, $C(CH_3)_3$), 6.90 (m, 24H, aryl-H), 7.38 (m, 13H, aryl-H). ^{31}P {^{1}H} NMR (400MHz) δ/ppm: 65.11 (s, PPh_3). FTIR (KBr) ν/cm^{-1} 2254, 2178. UV-vis (THF) λ_{max} / nm (ε / M^{-1} cm^{-1}): 426 (3800), 576 (3200), 842 (440).

Synthesis of (CO)Ru(^{Ph}ap)(PPh_3)$_2$ (**4a**)

In a 20 mL scintillation vial, **1a** (0.11 g, 0.12 mmol, 1 equiv.) was dissolved in 10 mL benzene. To it, paraformaldehyde (0.17 g, 5.8 mmol, 50 equiv.) was added and stirred overnight in ambient temperature. Excess paraformaldehyde was filtered before volatiles were removed in vacuo to afford deep magenta solids in 87% yield (0.11 g). X-ray quality crystals were grown from chilled Et_2O solutions. ^{1}H NMR (C_6D_6, 400 MHz) δ/ppm: 1.41 (s, 9H, $C(CH_3)_3$), 1.49 (s, 9H, $C(CH_3)_3$), 6.90 (m, 23H, aryl-H), 7.32 (m, 14H, aryl-H). ^{31}P {^{1}H} NMR (400MHz) δ/ppm: 55.95 (s, PPh_3). FTIR (KBr) ν/cm^{-1} 1937. UV-vis (THF) λ_{max} / nm (ε / M^{-1} cm^{-1}): 418 (5900), 544 (11000).

Synthesis of (CO)$_2$Ru(^{Ph}ap)(PPh_3)$_2$ (**4b**)

A 50 mL Konte flask was charged with 10 mL diethyl ether solution of **1a** (0.11 g, 0.12 mmol, 1 equiv.). After two freeze-pump-thaw cycles, the thawed solution was exposed to 1 atm CO. The color of the solution changed instantly from dark purple to dark magenta. X-ray quality crystals were grown from chilled pentane solutions. The following measurements were collected *in situ* as the complex cannot be isolated under N_2 atmosphere. ^{1}H NMR (C_6D_6, 400 MHz) δ/ppm: 1.33 (s, 9H, $C(CH_3)_3$), 1.62 (s, 9H, $C(CH_3)_3$), 6.90 (m, 23H, aryl-H), 7.43 (m,

14H, aryl-H). FTIR (KBr) ν/cm^{-1} 1939. UV-vis (THF) λ_{max} / nm (ε / M^{-1} cm^{-1}): 385 (4700), 535 (9900).

Synthesis of $(C_2H_4)Ru(^{Ph}ap)(PPh_3)_2$ (**5**)

In a 50 mL Strauss flask, **1a** (0.29 g, 0.030 mmol) was dissolved in 20 mL pentane. The solution was frozen and the headspace was evacuated. After thawing the solution, 1 atm of ethylene was added. The flask was closed and swirled. X-ray quality crystals were grown in room temperature from the crude solution. ^{1}H NMR (C_6D_6, 400 MHz) δ/ppm: 1.35 (s, 9H, $C(CH_3)_3$), 1.57 (s, 9H, $C(CH_3)_3$), 2.70 (br s, 4H, $C2H_4$), 6.82-6.92 (m, aryl-H), 7.27-7.25 (m, aryl-H), 7.52 (br s, 1H, aryl-H). ^{31}P {^{1}H} NMR (400MHz) δ/ppm: 58.16 (s, PPh_3). UV-vis (THF) λ_{max} / nm (ε / M^{-1} cm^{-1}): 416 (4700), 548 (9000), 855 (1400).

Table 2.7 X-ray diffraction data collection and refinement parameters for complexes **1-5**.

Complex	1a	2a	2b	4a	4b	5
empirical formula	$C_{56}H_{55}N_3OP_2Ru$	$C_{29}H_{52}NOP_3Ru$	$C_{64}H_{64}NOP_3Ru \cdot 2(C_5H_{12})$	$C_{57}H_{55}NO_2P_2Ru \cdot 3(C_5H_{12})$	$C_{58}H_{55}NO_3P_2Ru \cdot ½(C_5H_{12})$	$C_{58}H_{59}NOP_2Ru \cdot ½(C_5H_{12})$
formula weight	949.04	624.69	1201.43	1165.46	1013.11	985.14
crystal system	Triclinic	Monoclinic	Monoclinic	Monoclinic	Monoclinic	Monoclinic
space group	$P\bar{1}$	$P2_1/n$	$P2_1/n$	$C2/c$	$C2/c$	$P2_1/c$
T / K	100.00	133(2)	93(2)	92.85	133.15	93.15
***a* / Å**	14.2936(10)	10.9456(5)	13.0023(8)	47.7468(18)	20.5382(11)	10.3322(17)
***b* / Å**	17.2076(13)	15.3477(8)	18.8987(12)	19.4795(6)	17.9423(10)	12.382(2)
***c* / Å**	21.5709(16)	18.8521(9)	24.1841(15)	29.0721(10)	27.1439(15)	39.084(6)
***α* / °**	98.791(3)	90	90	90	90	90
***β* / °**	97.947(3)	95.7338(8)	90.3560(10)	114.317(2)	95.7307(10)	95.158(2)
***γ* / °**	108.858(3)	90	90	90	90	90
***V* / Å³**	4860.9(6)	3151.1(3)	5942.6(6)	24640.6(15)	9952.6(9)	4980.0(14)
Z	4	4	4	16	8	4
refl. collected	24152	77535	125488	160768	123042	76777
Data/restraints/parameters	24152 / 0 / 1147	9620 / 0 / 331	19105 / 6 / 625	22302 / 130 / 1171	14963 / 0 / 616	15125 / 1 / 590
R1 (*I*> 2*σ*)[a]	0.0637	0.0226	0.0379	0.0586	0.0357	0.0337
***w*R2 (all data)[b]**	0.1251	0.0562	0.0921	0.1346	0.0869	0.0838
***GOF*[c]**	1.125	1.023	1.026	1.033	1.025	1.019

[a] $R1 = \Sigma||F_o|-|F_c||/\Sigma|F_o|$; [b] $wR2 = [\Sigma[w(F_o^2-F_c^2)^2]/\Sigma[w(F_o^2)^2]]^{1/2}$

[c] Goodness of Fit = $S = [\Sigma[w(F_o^2-F_c^2)^2] / (n-p)]^{1/2}$ where n is the number of reflections and p is the total number of parameters refined.

2.6. References

(1) Gianino, J.; Brown, S. N. Highly Covalent Metal–Ligand π Bonding in Chelated Bis- and Tris(Iminoxolene) Complexes of Osmium and Ruthenium. *Dalton Trans.* **2020**, *49* (21), 7015–7027. https://doi.org/10.1039/D0DT01287D.

(2) Lever, A. B. P.; Auburn, P. R.; Dodsworth, E. S.; Haga, M. Aki.; Liu, Wei.; Melnik, Milan.; Nevin, W. Andrew. Bis(Dioxolene)(Bipyridine)Ruthenium Redox Series. *J. Am. Chem. Soc.* **1988**, *110* (24), 8076–8084. https://doi.org/10.1021/ja00232a020.

(3) Boyer, J. L.; Rochford, J.; Tsai, M.-K.; Muckerman, J. T.; Fujita, E. Ruthenium Complexes with Non-Innocent Ligands: Electron Distribution and Implications for Catalysis. *Coord. Chem. Rev.* **2010**, *254* (3–4), 309–330. https://doi.org/10.1016/j.ccr.2009.09.006.

(4) Gorelsky, S. I.; Lever, A. B. P.; Ebadi, M. Ruthenium D-Orbital Delocalization in Bis(Bipyridine)Ruthenium Derivatives of Redox Active Quinonoid Ligands. *Coord. Chem. Rev.* **2002**, *230* (1–2), 97–105. https://doi.org/10.1016/S0010-8545(02)00094-2.

(5) Lever, A. B. P.; Masui, H.; Metcalfe, R. A.; Stufkens, D. J.; Dodsworth, E. S.; Auburn, P. R. The Ground and Excited State Electronic Structures of Ruthenium Quinones and Related Species. *Coord. Chem. Rev.* **1993**, *125* (1–2), 317–331. https://doi.org/10.1016/0010-8545(93)85028-3.

(6) Haga, M.; Dodsworth, E. S.; Lever, A. B. P. Catechol-Quinone Redox Series Involving Bis(Bipyridine)Ruthenium(II) and Tetrakis(Pyridine)Ruthenium(II). *Inorg. Chem.* **1986**, *25* (4), 447–453. https://doi.org/10.1021/ic00224a013.

(7) Boone, S. R.; Pierpont, C. G. Charge Delocalization in Ruthenium-Quinone Complexes. Structural Characterization of Bis(Bipyridine)(3,5-Di-Fert-Butylsemiquinonato)Ruthenium(II) Perchlorate and Trans -Bis(4-Íerí-Butylpyridine)Bis(3,5-Di-Íerí-Butylquinone)Ruthenium.

(8) Bhattacharya, S.; Pierpont, C. G. Comparative Bonding Properties of Semiquinonate and Iminosemiquinonate Radical Ligands in Ru(CO)z(3,6-DBSQ)2 and Ru(CO)2(PhenoxSQ)2.

(9) Anillo, A.; Barrio, C.; Garcia-Granda, S.; Obeso-Rosete, R. Crystal Structure and Reactivity of [Ru{C,H,(NH)=-I,2}- (PPh,),] with x-Acid Ligandst.

(10) Masui, H. Metalloaromaticity. *Coord. Chem. Rev.* **2001**, *219–221*, 957–992. https://doi.org/10.1016/S0010-8545(01)00389-7.

(11) Bhattacharya, S.; Pierpont, C. G. Structure and Bonding in Bis(Quinone) Complexes of Ruthenium. Synthesis and Characterization of the Ru(PPh3)2(SQ)2 (SQ = 3,5-Tert-Butylsemiquinone, Tetrachloro-1,2-Semiquinone) Series. *Inorg. Chem.* **1991**, *30* (7), 1511–1516. https://doi.org/10.1021/ic00007a017.

(12) Bhattacharya, S.; Gupta, P.; Basuli, F.; Pierpont, C. G. Structural Systematics for *o*-C_6H_4XY Ligands with X,Y= O, NH, and S Donor Atoms. *o*-Iminoquinone and *o*-Iminothioquinone Complexes of Ruthenium and Osmium. *Inorg. Chem.* **2002**, *41* (22), 5810–5816. https://doi.org/10.1021/ic025766+.

(13) Haga, Masaaki.; Dodsworth, E. S.; Lever, A. B. P.; Boone, S. R.; Pierpont, C. G. Synthesis, Characterization, and Charge Distribution of Bis(4-Tert-Butylpyridine)Bis(3,5-Di-Tert-Butylquinone)Ruthenium. *J. Am. Chem. Soc.* **1986**, *108* (23), 7413–7414. https://doi.org/10.1021/ja00283a049.

(14) Pierpont, C. G.; Buchanan, R. M. Transition Metal Complexes of O-Benzoquinone, o-Semiquinone, and Catecholate Ligands. *Coord. Chem. Rev.* **1981**, *38* (1), 45–87. https://doi.org/10.1016/S0010-8545(00)80499-3.

(15) Ye, S.; Sarkar, B.; Duboc, C.; Fiedler, J.; Kaim, W. The Redox Series $[M(Bpy)_2(Q)]^{n+}$, M = Ru or Os, Q = 3,5-Di-*Tert*-Butyl-N-Phenyl-1,2-Benzoquinonemonoimine. Isolation and a Complete X and W Band EPR Study of the Semiquinone States ($n = 1$). *Inorg. Chem.* **2005**, *44* (8), 2843–2847. https://doi.org/10.1021/ic048407i.

(16) Das, D.; Das, A. K.; Sarkar, B.; Mondal, T. K.; Mobin, S. M.; Fiedler, J.; Záliš, S.; Urbanos, F. A.; Jiménez-Aparicio, R.; Kaim, W.; Lahiri, G. K. The Semiquinone–Ruthenium Combination as a Remarkably Invariant Feature in the Redox and Substitution Series $[Ru(Q)_n(Acac)_{3-n}]^m$, $n = 1–3$; $m = (–2), –1, 0, +1, (+2)$; Q = 4,6-Di-*Tert*-Butyl-*N*-Phenyl-*o*-Iminobenzoquinone. *Inorg. Chem.* **2009**, *48* (24), 11853–11864. https://doi.org/10.1021/ic901900g.

(17) Brown, S. N. Metrical Oxidation States of 2-Amidophenoxide and Catecholate Ligands: Structural Signatures of Metal–Ligand π Bonding in Potentially Noninnocent Ligands. *Inorg. Chem.* **2012**, *51* (3), 1251–1260. https://doi.org/10.1021/ic202764j.

(18) Broere, D. L. J.; Plessius, R.; Van Der Vlugt, J. I. New Avenues for Ligand-Mediated Processes – Expanding Metal Reactivity by the Use of Redox-Active Catechol, o-Aminophenol and o-Phenylenediamine Ligands. *Chem. Soc. Rev.* **2015**, *44* (19), 6886–6915. https://doi.org/10.1039/C5CS00161G.

(19) Mondal, R.; Guin, A. K.; Chakraborty, G.; Paul, N. D. Metal–Ligand Cooperative Approaches in Homogeneous Catalysis Using Transition Metal Complex Catalysts of Redox Noninnocent Ligands. *Org. Biomol. Chem.* **2022**, *20* (2), 296–328. https://doi.org/10.1039/D1OB01153G.

(20) Singh, K.; Kundu, A.; Adhikari, D. Ligand-Based Redox: Catalytic Applications and Mechanistic Aspects. *ACS Catal.* **2022**, *12* (20), 13075–13107. https://doi.org/10.1021/acscatal.2c02655.

(21) van der Vlugt, J. I. Radical-Type Reactivity and Catalysis by Single-Electron Transfer to or from Redox-Active Ligands. *Chem. – Eur. J.* **2019**, *25* (11), 2651–2662. https://doi.org/10.1002/chem.201802606.

(22) Hino, T.; Wada, T.; Fujihara, T.; Tanaka, K. Redox Behavior of New Ru–Dioxolene–Ammine Complexes and Catalytic Activity toward Electrochemical Oxidation of Alcohol under Mild Conditions. *Chem. Lett.* **2004**, *33* (12), 1596–1597. https://doi.org/10.1246/cl.2004.1596.

(23) Sengupta, D.; Bhattacharjee, R.; Pramanick, R.; Rath, S. P.; Saha Chowdhury, N.; Datta, A.; Goswami, S. Exclusively Ligand-Mediated Catalytic Dehydrogenation of Alcohols. *Inorg. Chem.* **2016**, *55* (19), 9602–9610. https://doi.org/10.1021/acs.inorgchem.6b01310.

(24) Tolman, C. A. Phosphorus Ligand Exchange Equilibriums on Zerovalent Nickel. Dominant Role for Steric Effects. *J. Am. Chem. Soc.* **1970**, *92* (10), 2956–2965. https://doi.org/10.1021/ja00713a007.

(25) Collman, J. P.; Hutchison, J. E.; Lopez, M. A.; Guilard, R. A Stable Dinitrogen Complex of a Ruthenium Cofacial Diporphyrin. *J. Am. Chem. Soc.* **1992**, *114* (21), 8066–8073. https://doi.org/10.1021/ja00047a015.

(26) Collman, J. P.; Brauman, J. I.; Fitzgerald, J. P.; Sparapany, J. W.; Ibers, J. A. Reversible Binding of Dinitrogen and Dioxygen by a Ruthenium Picnic-Basket Porphyrin. *J. Am. Chem. Soc.* **1988**, *110* (11), 3486–3495. https://doi.org/10.1021/ja00219a024.

(27) Li, W.; Wu, X.-F. The Applications of (Para)Formaldehyde in Metal-Catalyzed Organic Synthesis. *Adv. Synth. Catal.* **2015**, *357* (16–17), 3393–3418. https://doi.org/10.1002/adsc.201500753.

(28) Huber G. Herzberg. *Molecular Spectra And Molecular Structure, IV. Constants Of Diatomic Molecules, K. P. Huber G. Herzberg*.

(29) Gilliam, O. R.; Johnson, C. M.; Gordy, W. Microwave Spectroscopy in the Region from Two to Three Millimeters. *Phys. Rev.* **1950**, *78* (2), 140–144. https://doi.org/10.1103/PhysRev.78.140.

(30) Herzberg, G. *Electronic Spectra and Electronic Structure of Polyatomic Molecules*; Van Nostrand, 1966.

(31) Chaudhuri, P.; Verani, C. N.; Bill, E.; Bothe, E.; Weyhermüller, T.; Wieghardt, K. Electronic Structure of Bis(*o* -Iminobenzosemiquinonato)Metal Complexes (Cu, Ni, Pd). The Art of Establishing Physical Oxidation States in Transition-Metal Complexes Containing Radical Ligands. *J. Am. Chem. Soc.* **2001**, *123* (10), 2213–2223. https://doi.org/10.1021/ja003831d.

(32) Bruker AXS, Inc. SAINT, 2013.

(33) Sheldrick, G. M.; Bruker AXS, Inc. SADABS.

(34) Sheldrick, G. M. SHELXTL, 2001.

(35) Farrugia, L. J. ORTEP-3 for Windows - a Version of ORTEP-III with a Graphical User Interface (GUI). *J. Appl. Crystallogr.* **1997**, *30* (5–1), 565–565. https://doi.org/10.1107/S0021889897003117.

(36) Frisch, M. J.; Trucks, G. W.; Schlegel, H. B.; Scuseria, G. E.; Robb, M. A.; Cheeseman, J. R.; Scalmani, G.; Barone, V.; Petersson, G. A.; Nakatsuji, H.; Li, X.; Caricato, M.; Marenich, A. V.; Bloino, J.; Janesko, B. G.; Gomperts, R.; Mennucci, B.; Hratchian, H. P.; Ortiz, J. V.; Izmaylov, A. F.; Sonnenberg, J. L.; Williams; Ding, F.; Lipparini, F.; Egidi, F.; Goings, J.; Peng, B.; Petrone, A.; Henderson, T.; Ranasinghe, D.; Zakrzewski, V. G.; Gao, J.; Rega, N.; Zheng, G.; Liang, W.; Hada, M.; Ehara, M.; Toyota, K.; Fukuda, R.; Hasegawa, J.; Ishida, M.; Nakajima, T.; Honda, Y.; Kitao, O.; Nakai, H.; Vreven, T.; Throssell, K.; Montgomery Jr., J. A.; Peralta, J. E.; Ogliaro, F.; Bearpark, M. J.; Heyd, J. J.; Brothers, E. N.; Kudin, K. N.; Staroverov, V. N.; Keith, T. A.; Kobayashi, R.; Normand, J.; Raghavachari, K.; Rendell, A. P.; Burant, J. C.; Iyengar, S. S.; Tomasi, J.; Cossi, M.; Millam, J. M.; Klene, M.; Adamo, C.; Cammi, R.; Ochterski, J. W.; Martin, R. L.; Morokuma, K.; Farkas, O.; Foresman, J. B.; Fox, D. J. Gaussian 16 Rev. C.01, 2016.

Chapter 3: Reactivity of Ruthenium(II) Amidophenolate Complexes

3.1. Introduction

In recent years, a growing number of homogenous metal catalysts have been developed where the ligand actively participates in chemical transformations, as opposed to the traditional systems where the reactivity takes place at the metal center.[1,2] This mode of reactivity has been since labeled as metal-ligand cooperativity (MLC), which is defined as reactions that has bond-forming or bond-breaking steps that involve both the metal and the ligand. Well-known examples of MLC arise in hydrogenation/dehydrogenation catalysis.[2–4] One of the earliest demonstrations involved a ruthenium cyclopentadienone complex that cleaves H_2 between the metal and the oxygen on the cyclopentadienone.[5] Since then, numerous hydrogenation catalysts invoking MLC have been reported, including the Noyori's asymmetric hydrogenation catalysts that enantioselectively transfer hydrogenate ketones. Despite the expanding library of studies investigating MLC, most applications remain centered on H–H bond cleavage. Recent efforts have sought to expand the scope by exploring the heterolytic cleavage of other E–H bonds (E = Si, B), motivated by the similar electronegativities of silicon (1.9) and boron (2.0) to that of hydrogen (2.2).[6] Ligands containing nitrogen, oxygen, or sulfur have been employed due to their strong affinity with silicon atoms for Si–H cleaving, which can be seen in **Scheme 3.1**.[7–9] In all cases, the metal acts as the Lewis acid and the ligand Lewis base, so that the hydrosilane is cleaved into a hydride on the metal and a silyl on the ligand.

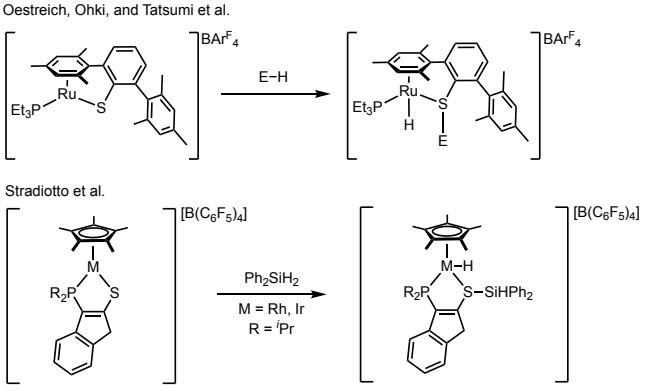

Scheme 3.1 E–H bond cleaving (E = Si, B) through metal-ligand reactivity. (Ar^F = 3,5-bis(trifluoromethyl)phenyl).

Similar systems have been also found to cleave B–H bonds in an analogous fashion.

Ruthenium complexes with catecholate type redox-active ligands (Ru-RALs) have been well studied for their increased covalency between the metal and ligand, which obscures the oxidation state assignments of the metal and ligand. Extensive studies of the Ru-RALs' electronic properties led to the classification of the systems by the overall oxidation state of the complex, ranging from the fully oxidized Class A (Ru^{III}-quinone) to the fully reduced Class D (Ru^{II}-catecholate). But reactivity studies that utilize such distinctive electronic characteristic have been scarce. Catecholate type ligands with at least one nitrogen as the donor have been well studied for their ability as Lewis bases to store protons,[10–12] while ruthenium hydrides are known as stable catalysts for hydrogenations.[13] Combining the two, Ru-RALs are expected to be good candidates for heterolytic cleavage of H_2 or E–H bonds.

In addition, electron-rich late-transition metal complexes are also known to promote the rearrangement of terminal alkynes into metal vinylidenes.[14–21] Many Ru(II) systems with strongly donating ancillary ligands exhibit tautomerization between an η^2-acetylene adduct and the corresponding vinylidene isomer.[22–25] This acetylene-vinylidene equilibrium has been well documented across ruthenium complexes and is sensitive to ligand electronic effects, with more donating ligands shifting the equilibrium towards the vinylidene.[26] Once the vinylidene form is accessed, these species can undergo further transformations such as the homocoupling of the coordinated alkynes into 1,3-eneyes.[21]

In a similar context, catecholate type redox-active ligand complexes have demonstrated novel reactivity through the ligand's abilities to act as electron reservoirs. A proof-of-concept reaction with group IV d^0 metal complexes have displayed catalytic nitrene transfer by sourcing the electrons from the RAL.[27] In addition, a d^{10} late transition metal complex was shown to be capable of nitrene transfer by electron density alleviation from the

metal through the π system of a RAL, stabilizing the putative imido.[28] Given these demonstrations where RALs can either donate or redistribute electron density to enable nitrene transfer, we wanted to test if the Ru-RAL system could similarly support the formation of the reactive imido and promote nitrene transfer.

In this chapter, chemical oxidation, protonation, and preliminary reactivity studies with the Ru-RAL complex introduced in the previous chapter, $(N_2)Ru(^{Ph}ap)(PPh_3)_2$ (^{Ph}ap = 3,5-di-*tert*-butyl-(6-phenylamidophenolate), PPh_3 = triphenylphosphine) is presented. The complex has been isolated in its singly and doubly oxidized analogue, and evidence for the heterolytic cleavage of H_2 was found from ^1H NMR. However, addition of nitrene donors have led to a tetrazene complex that does not display nitrene transfer.

3.2. Results

3.2.1. Chemical oxidation of 3a

In the previous chapter, it was revealed that the fully reduced complexes $(N_2)Ru(^{Ph}ap)(PPh_3)_2$ (**1a**) and $(MeCN)Ru(^{Ph}ap)(PPh_3)_2$ (**3a**) have two oxidation events anodic to their open circuit potentials. To test the stability of the oxidized states that would be accessed during the intended 2-electron reactivity, **3a** was chemically oxidized by one and two electrons through a ferrocenium salt in acetonitrile according to **Scheme 3.2**. The resulting six-coordinate mono- and di-cationic Ru-RAL complexes were characterized through X-ray crystallography, NMR, EPR, and electronic spectroscopies, and electrochemical studies to verify their oxidation states.

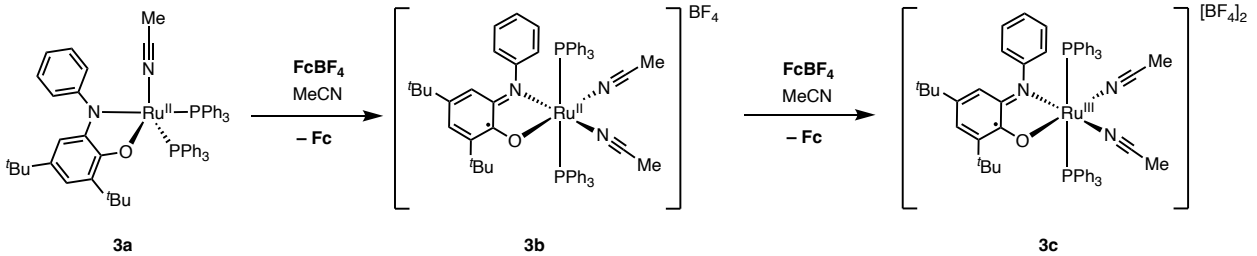

3a **3b** **3c**

Scheme 3.2 Chemical oxidation of **3a** with ferrocenium salts.

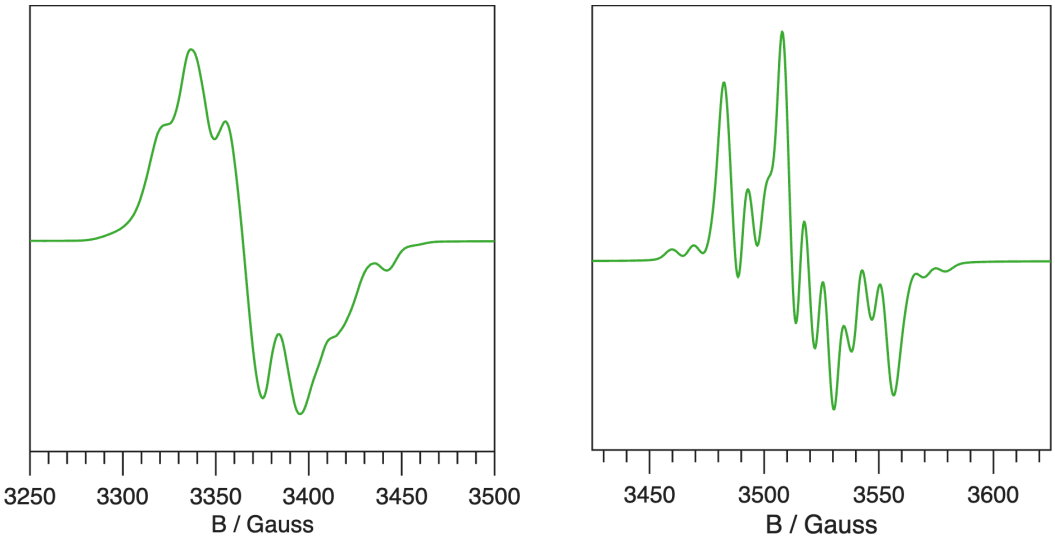

Figure 3.1 Experimental X-band EPR spectra of **3b** in toluene at 77 K (left) and 298 K (right).

The singly oxidized monocation species $(MeCN)_2Ru(^{Ph}isq)(PPh_3)_2$ **3b** was expected to harbor a radical as a Class C Ru-RAL complex, either on the metal as $Ru^{III\text{-}Ph}ap$ or on the ligand as $Ru^{II\text{-}Ph}isq$. As expected, the complex was paramagnetic and showed an EPR signal with g = 1.9996. which indicates S = ½ and similar to the EPR signal of a free iminosemiquinone radical (g = 2.0061) reported earlier (**Figure 3.1**).[29] Previous EPRs of Ru-RALs with iminosemiquinones or phosphines have shown that the delocalization of the radical on the metal could lead to hyperfine coupling with nuclei on ancillary ligands.[30,31] As

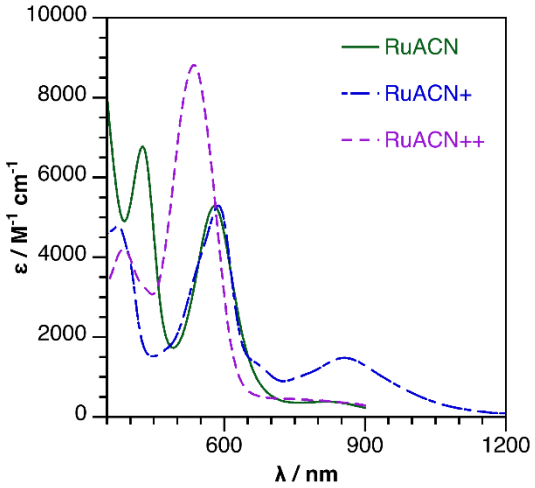

Figure 3.2 UV-visible spectra of **3a-c** in THF.

expected from those examples, the hyperfine coupling of **3b** was complex, with multiple possible nuclei that could contribute: ^{99}Ru, ^{101}Ru, ^{14}N and ^{31}P. Attempts to simulate the EPR accurately were unfruitful.

Table 3.1 UV-vis transition of complexes 3a-c in THF.

λ / nm (ε / $M^{-1}cm^{-1}$)		
3a	**3b**	**3c**
426 (3800)	375 (5000)	384 (4200)
576 (3200)	588 (5700)	536 (8800)
842 (400)	856 (1600)	

In the UV-vis region of the electromagnetic spectrum presented in **Figure 3.2** and **Table 3.1**, there was a characteristic low energy absorption band observed in metal semiquinone complexes that is assigned as an intraligand π to π* charge transfer at 856 nm.[32,33] The solid-state structure (**Figure 3.3**) and bond distances within the ligand revealed by single crystal X-ray diffraction presented in **Table 3.2** showed that the N–C(2) bond distance for **3b** (1.364 Å) is slightly shorter compared to the neutral **3a** (1.390 Å), while the O–C(1) bond distance

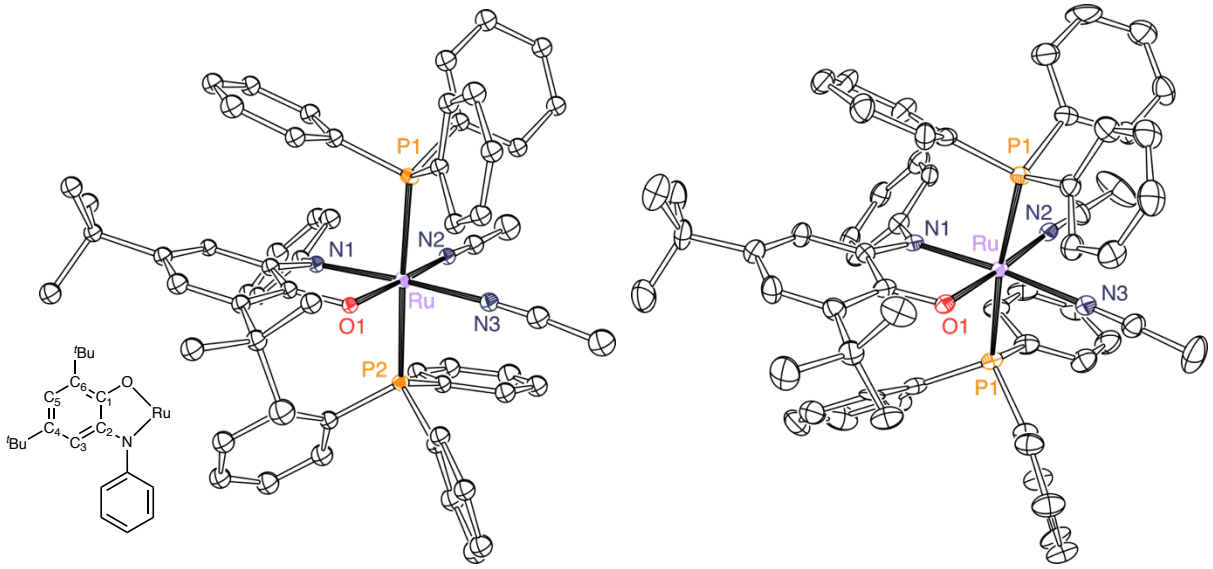

Figure 3.3 ORTEP diagrams of **3b** (left) and **3c** (right) with thermal ellipsoids shown at 50 % probability. Hydrogen atoms, solvent molecules, and counterions have been omitted for clarity.

decreases less (1.318 Å vs. 1.333 Å). In addition, the C(3)–C(4) and C(5)–C(6) distances contract in **3b** while the other C-C distances in the ligand backbone increases, as expected of

Table 3.2 Selected bond distances (Å) and angles of solid-state structures of **3a-c**. Estimated standard deviations are indicated in parentheses.

Complex	3a[a]	3b	3c
Ru–O(1)	2.052	2.0691(11)	2.050(4)
Ru–N(1)	1.984	2.0312(13)	2.004(5)
O(1)–C(1)	1.333	1.3180(19)	1.275(8)
N(1)–C(2)	1.390	1.364(2)	1.343(9)
C(1)–C(2)	1.420	1.435(2)	1.449(10)
C(2)–C(3)	1.396	1.417(2)	1.415(9)
C(3)–C(4)	1.388	1.373(2)	1.355(10)
C(4)–C(5)	1.398	1.421(2)	1.443(11)
C(5)–C(6)	1.405	1.384(2)	1.396(2)
C(6)–C(1)	1.418	1.429(2)	1.465(9)
Ru–P(1)	2.240	2.4021(4)	2.4086(17)
Ru–P(2)	2.294	2.4041(4)	2.4362(16)
Ru–N(2)	1.992	2.0130(14)	2.027(5)
Ru–N(3)	-	2.0605(14)	2.066(6)
MOS	**−1.63**	**−1.18**	**−0.71**
O(1)–Ru–N(1)	79.36	79.12(5)	77.9(2)
P(1)–Ru–P(2)	-	175.780(15)	172.73(6)
N(1)–Ru–N(3)	-	175.57(5)	174.9(2)
O(1)–Ru–N(2)	-	177.87(5)	175.3(2)

(a) Preliminary data

the localized double bonds in the iminosemiquinone. This leads to the calculated metrical oxidation state (MOS)[34] of the ligand being −1.18. The evidence above indicates that the radical resides mostly on the ligand as a semiquinone, with some delocalization into the metal as seen from the hyperfine coupling in the EPR spectra.

In the case of the doubly oxidized **3c**, the position of the electron was not as explicit. The complex showed sharp peaks in the diamagnetic region of ^{1}H and $^{31}P\{^{1}H\}$ NMR and was EPR silent, which ruled out the open shell triplet state where the metal and ligand each harbor a radical. However, the low energy peak in the UV-vis spectra of **3c** showed up at 586 nm, which is consistent with a mixed Ru(d)-RAL(π) to RAL(π*) charge transfer in similar ruthenium complexes.[35,36] The solid-state bond distances of **3c** as presented in **Table 3.2** did

show signs of some further oxidation on the ligand, as observed by the shorter O–C(1) bond length between **3b** and **3c** (1.318 Å vs. 1.275 Å). However, the rest of the C–C bond lengths do not show significant oxidation compared to the expected bond distances for a fully oxidized iq state. For the C(3)–C(4) and C(5)–C(6) bonds where the double bond character is localized, the expected bond length is 1.35 Å vs 1.355 and 1.396 Å. And the rest of the C–C bond lengths are expected to range from 1.43 to 1.51 Å vs 1.443 to 1.465 Å. The calculated MOS therefore turns out to be −0.71, a value closer to a formal isq•. This made it difficult to assign a definitive formal oxidation state to the ligand or metal.

Table 3.3 Mulliken population analysis distributions for selected FMOs of **3b** and **3c**.

		M / %	N(^{Ph}ap) / %	O / %	C(^{Ph}ap) / %	P / %
3b	**LUMO**	32.1	0.0	0.0	0.0	15.1
	SOMO	12.5	19.4	14.7	44.7	0.0
3c	**LUMO**	15.1	20.1	12.3	41.9	2.8
	HOMO	38.6	3.8	9.4	37.6	0.0

Density functional theory (DFT) calculations of **3b** and **3c** were performed in Gaussian 16 to support the extent of covalency observed through experimental data. The *tert*-butyl groups of the solid structures were substituted to hydrogen atoms to minimize computational load. The final geometry optimizations and energy calculations were carried out using B3LYP

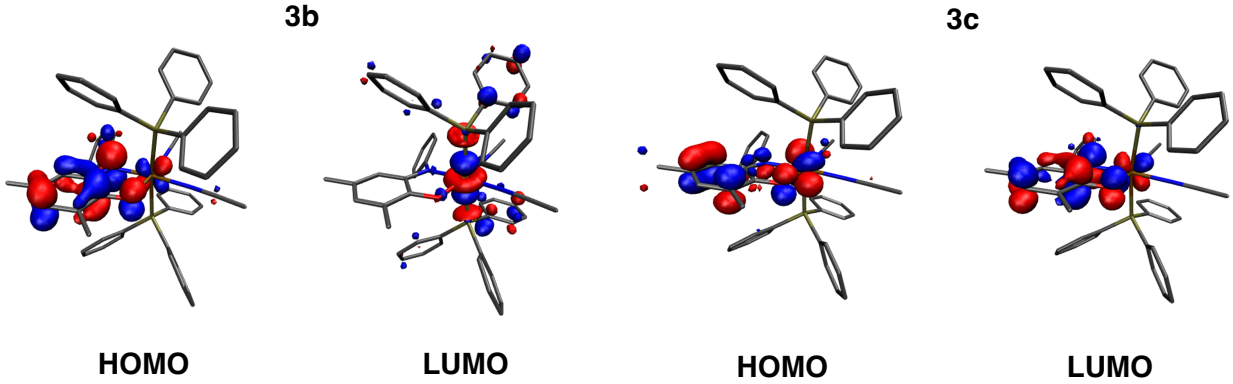

Figure 3.4 Kohn-Sham representations of the FMOs of **3b** (left) and **3c** (right). (iso = 0.045)

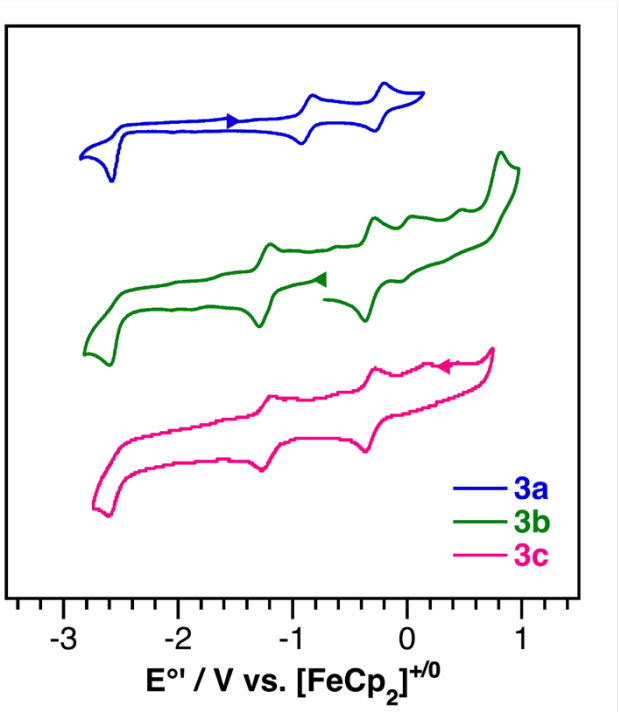

Figure 3.5 Cyclic voltammograms of **3a-c** in MeCN at 200 mV/s. Star indicates the open circuit potential.

functional with LANL2DZ basis set for the central ruthenium and 6-311G basis set for all other atoms. The bond metrics obtained from the optimized geometry and thermodynamic frequency calculations were within 0.04 Å with the experimental structural data for the metal-heteroatom bond distances, and within 0.02 Å for the intraligand bond distances. Mulliken population analysis yielded the atomic charge distributions for the frontier molecular orbitals (FMOs), presented in **Table 3.3**. The Kohn-Sham diagrams of the same FMOs are presented in **Figure 3.4**. The calculated spin density plot for **3b** correlate well with the SOMO (**Figure 3.10**).

The oxidized species **3b** and **3c** were also studied electrochemically to observe if the reduction in the six-coordinate environment was reversible in the cyclic voltammetry timescale. Voltammetric experiments were performed with 1.0 mM analyte and 0.1 M $[Bu_4N][PF_6]$ electrolyte concentration with a glassy carbon working electrode, platinum wire counter electrode, and $Ag^{+/0}$ pseudo-reference electrode under N_2 atmosphere at 298 K. All

three complexes **3a-c** showed similar electrochemistry, with a events at −2.5, −1.2, and −0.3 V. The cathodic shift of the second event at −1.2 V compared to −0.8 V of **3a** is possibly due to the change in coordination number around the metal as it picks up an acetonitrile from the solvent. In **3b**, another irreversible event at +0.7 V was observed, which is most likely a metal oxidation.

Table 3.4 Reduction potentials from cyclic voltammetry experiments for **3a-c** in MeCN, respectively at 200 mV/s. All values are referenced to the $[FeCp_2]^{+/0}$ internal standard redox couple.

	E°' / V vs. $[FeCp_2]^{+/0}$ (i_{pa}/i_{pc})		
3a	−2.48	−0.83 (1.78)	−0.19 (1.02)
3b	−2.45	−1.22 (0.90)	−0.33 (1.23)
3c	−2.48	−1.23 (0.61)	−0.33 (1.02)

3.2.2. Reactivity with H_2

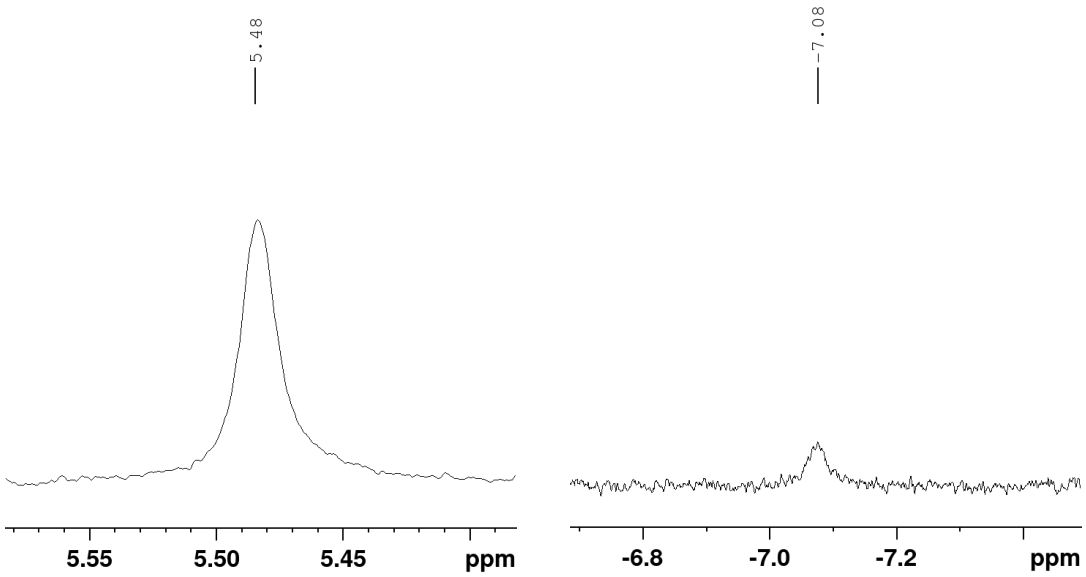

Figure 3.6 Zoomed in ^1H NMR of the H_2 addition product of **1a** in C_6D_6.

To determine if H_2 is being heterolytically cleaved by **1a**, the addition of excess gaseous H_2 to **1** was monitored by ^1H NMR in C_6D_6 with the residual proteo solvent signal as reference at 7.16 ppm. The color of the solution changed over the course of 30 minutes from a deep

purple of **1a** to a deep yellow. New broad singlets at 5.48 and −7.08 ppm were observed, which were assigned as N–H and Ru–H resonances, respectively (**Figure 3.6**). Attempts to isolate

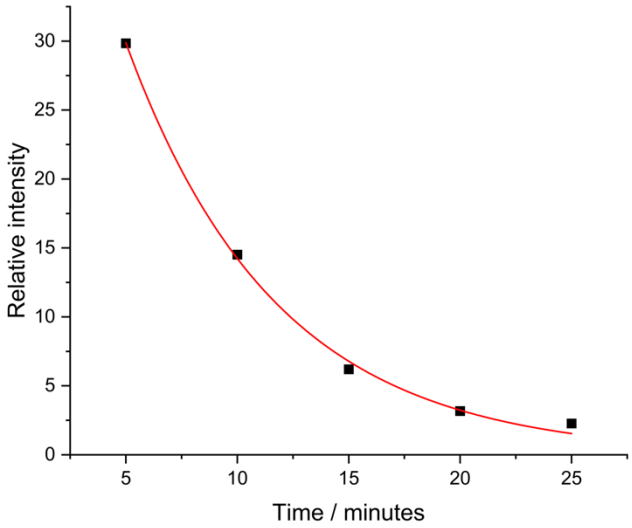

Figure 3.7 Relative area under the *tert*-butyl peaks of **1a** over time.

the newly generated hydrogenated species were unsuccessful due to the instability of the hydrogenated complex. In the presence of excess H_2, the complex decomposes through the hydrogenation and demetallation of the ligand. Upon exposure to vacuum, the hydrogenated product loses H_2 and reverts to 1 under N_2 atmosphere.

The characteristic *tert*-butyl signals from the ligand were monitored to track the kinetics of the hydrogenation in an attempt to understand the mechanism. Over the course of 20 minutes, the decrease of signals of **1a** and the generation of a new species was observed, which can be seen in **Figure 3.15**. The relative intensity has been plotted against time in **Figure 3.7**. Analogous experiment with D_2 was conducted, and the rate constant for each reaction was $k_H = 3.2 \pm 0.6$ and $k_D = 1.5 \pm 0.6$. The kinetic isotope effect (KIE), determined by the ratio of the rate constants with hydrogen and deuterium, was calculated to be 2.13.

Proof-of-concept direct and transfer hydrogenation studies were performed as presented in **Scheme 3.3**, monitored by ^{1}H NMR. As expected from the decreased stability of **1a** under excess H_2, direct hydrogenation attempts to stoichiometric benzyl aldehyde under H_2 atmosphere resulted in 64% conversion to benzyl alcohol after 15 hours in room temperature. Therefore, transfer hydrogenation was attempted in order to control the equivalents of H_2 that can be added onto complex **1a**. The addition of 1 equiv. NH_3BH_3 lead to a generation of the hydride peak at the same chemical shift as the H_2 addition product. However, both *tert*-butyl peaks were downshifted by 0.07 ppm and no corresponding N–H peak was observed. Using NH_3BH_3 as the hydrogen source to 5 equivalents of trans-stilbene led to a 100% conversion after 2 days in room temperature.

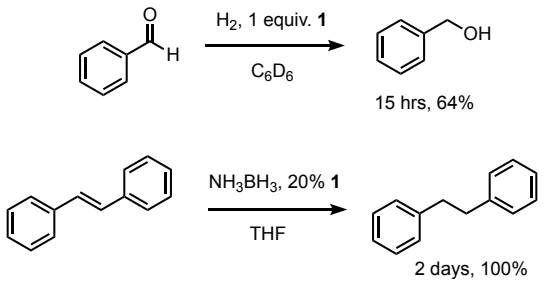

Scheme 3.3 Direct and transfer hydrogenation studies performed with complex **1a**.

3.2.3. Reactivity with acid

Because the hydrogenation product was not isolated successfully, protonation of **1a** was attempted to test the ability for the amidophenolate amine to store proton equivalents. An addition of 1 equiv. HBF_4 to 1a generated a cationic species where the proton was observed on the amidophenolate nitrogen (complex **6**). Structural data was obtained from an unwanted reaction between boron trifluoride

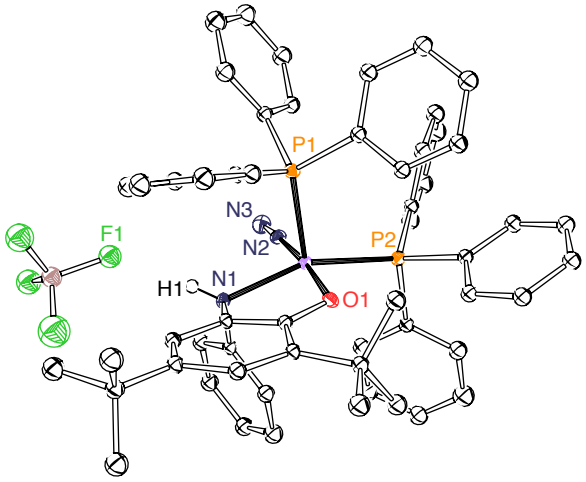

Figure 3.8 ORTEP diagram of **6** with thermal ellipsoids shown at 50 % probability. Hydrogen atoms and solvent molecules have been omitted for clarity.

etherate with water impurity and **1a**, which was confirmed to be **6** through ^{1}H NMR.

3.2.4. Addition of azides

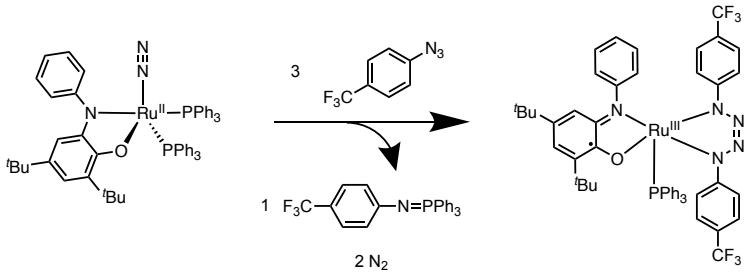

Scheme 3.4 Synthesis of the tetrazene complex **7**.

Inspired by earlier work in the group that utilized RALs to alleviate electron density on late transition metal center to invoke a transient imido,[28] N-group transfer reactivity was attempted through the introduction of 1-azido-4-(trifluoromethyl)benzene as the nitrene donor. Previous studies of metal phosphines exposed to azides have resulted in the oxidation of phosphines into hypervalent iminophosphoranes (R'N=PR_3). The subsequent dissociation of the iminophosphoranes have left empty coordination sites on the metal. Therefore, expecting reactivity with both equivalents of PPh_3, three equivalents of 1-azido-4-(trifluoromethyl)benzene was added to **1a** according to **Scheme 3.4**. The resulting complex was investigated through ^{1}H, ^{31}P {^{1}H}, and ^{19}F NMR and single crystal X-ray diffraction. Interestingly, only one equivalent of PPh_3 on the metal seem to react with the azide to generate the iminophosphorane, as determined by ^{31}P {^{1}H} and ^{19}F NMR where peaks at 1.86 and 60.29 ppm were observed. The other two equivalents of the azide are found bound to the ruthenium as a tetrazene (R–N–N=N–N–R) after releasing an equivalent of N_2, as observed in the solid-state structure in **Figure 3.9** as well as from the peaks at −61.73 and −61.62 ppm in the ^{19}F NMR. The isolated product **7** was identified as $Ru^{III}(^{Ph}isq)$(tetrazene) as the bond distances within

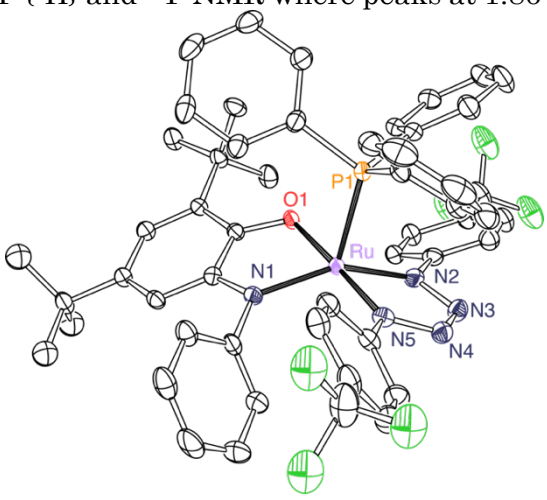

Figure 3.9 ORTEP diagram of **7** with thermal ellipsoids shown at 50 % probability. Hydrogen atoms and solvent molecules have been omitted for clarity.

the aminophenol was more consistent with the iminosemiquinone and the bond distances between the nitrogens of the tetrazene was consistent with the fully reduced 2– state (**Table 3.5**).[34,37]

Table 3.5 Selected bond distances (Å) and angles of solid-state structure of **6-8**.

Complex	6	7	8
Ru–O(1)	2.0418(10)	2.0761(16)	2.1026(15)
Ru–N(1)	2.1550(12)	1.973(2)	2.0047(18)
O(1)–C(1)	1.3508(16)	1.315(3)	1.325(3)
N(1)–C(2)	1.4591(18)	1.379(3)	1.392(3)
C(1)–C(2)	1.3968(19)	1.418(3)	1.419(3)
C(2)–C(3)	1.3887(19)	1.426(3)	1.399(3)
C(3)–C(4)	1.389(2)	1.383(3)	1.387(3)
C(4)–C(5)	1.407(2)	1.416(3)	1.402(3)
C(5)–C(6)	1.3969(19)	1.371(4)	1.396(3)
C(6)–C(1)	1.4247(19)	1.412(3)	1.422(3)
Ru–P(1)	2.3650(4)	2.3036(6)	2.3348(6)
Ru–P(2)	2.2609(4)	-	2.3191(6)
Ru–N(2)	1.9451(12)	1.957(2)	-
Ru–N(5)	-	1.969(2)	-
N(2)–N(3)	-	1.364(3)	-
N(3)–N(4)	-	1.297(3)	-
N(4)–N(5)	-	1.361(3)	-
Ru–C(7)	-	-	1.834(2)
C(7)–C(8)	-	-	1.316(4)
MOS	**-**	**–1.32**	**–1.55**
O(1)–Ru–N(1)	79.46(4)	77.53(7)	77.80(7)
N(2)–Ru–N(5)	-	75.04(9)	-
N(1)–Ru–N(2)	95.59(5)	147.54(9)	-
O(1)–Ru–N(5)	-	176.39(8)	-
O(1)–Ru–C(7)	-	-	166.44(8)
N(1)–Ru–P(1)	158.31(3)	-	134.13(5)
O(1)–Ru–N(2)	173.64(4)	-	-
τ_5	**0.26**	**0.48**	**0.54**

The reaction between **1a** and azide was monitored through ^{1}H NMR in C_6D_6 by following the peak intensity of the *tert*-butyl peaks of the amidophenolate for an attempt to elucidate the reaction mechanism. Excess azide was added in order to assume pseudo-first order kinetics. As the reaction proceeded, an intermediate species was observed at 1.45 and

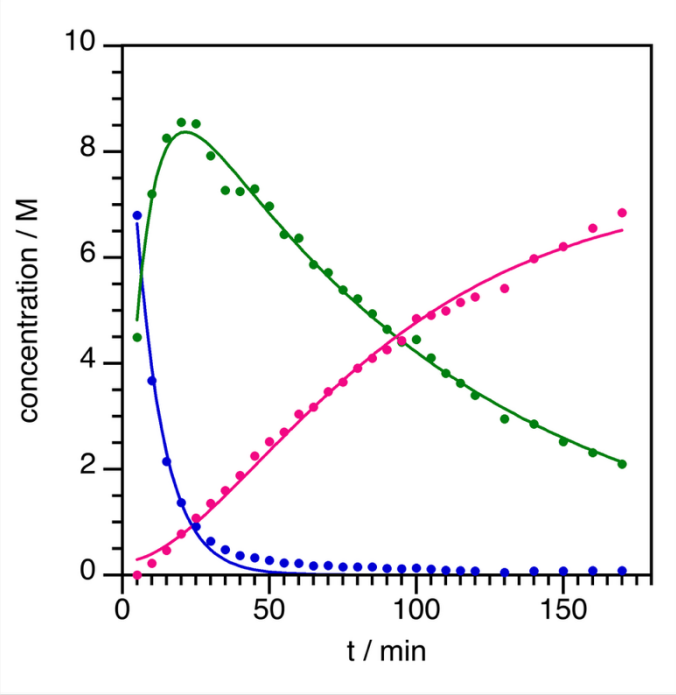

Figure 3.10 Kinetics data of the reaction between **1a** (blue) and 4 equivalents of 1-azido-4-(trifluoromethyl)benzene. The intermediate is depicted in green and product (**7**) in magenta.

1.52 ppm. The kinetics data of **1a**, the intermediate, and **7** are presented in **Figure 3.10**. The data was fitted as two consecutive first order reactions[38] according to the **Equations 3.1-3.3**. The reaction rate constant determined through triplicate measurement was k_1 = 0.103 ± 0.015 s^{-1} and k_2 = 0.0101 ± 0.0012 s^{-1}.

$$[A] = [A]_0 e^{-k_1 t} \qquad (3.1)$$

$$[B] = [A]_0 \frac{k_1}{k_2 - k_1}(e^{-k_1 t} - e^{k_2 t}) \qquad (3.2)$$

$$[C] = [A]_0 \left(1 + \frac{k_1 e^{-k_2 t} - k_2 e^{-k_1 t}}{k_2 - k_1}\right) \qquad (3.3)$$

Nitrene transfer reactivity with the tetrazene complex was attempted with 2,6-dimethylphenyl isocyanide in C_6D_6 monitored by NMR. However, even in elevated temperatures near 70 °C, no transfer was observed. Metal tetrazenes have been identified as an off-cycle side product in nitrene transfer catalysts,[39] and in general regarded as a stable analogue of the free R_2N_4 ligand.[40,41] However, imidos are invoked as intermediates for metal

tetrazenes generated through the addition of 2 equivalents of organic azides, through 1,3-additions.[42] Therefore, the addition of 1 atm of gaseous CO as the putative nitrene acceptor to **1a** before the addition of the azide was monitored through NMR. Upon initial addition of CO, a mixture of five- and six-coordinate carbonyl complexes reported in the previous chapter was generated. The consecutive addition of 4 equivalents of the organic azide and heating to 85 °C led to a generation of the respective isocyanate observed as a singlet at −62.16 ppm in ^{19}F NMR, though the integrity of the metal complex could not be determined.

3.2.5. Reactivity with phenylacetylene

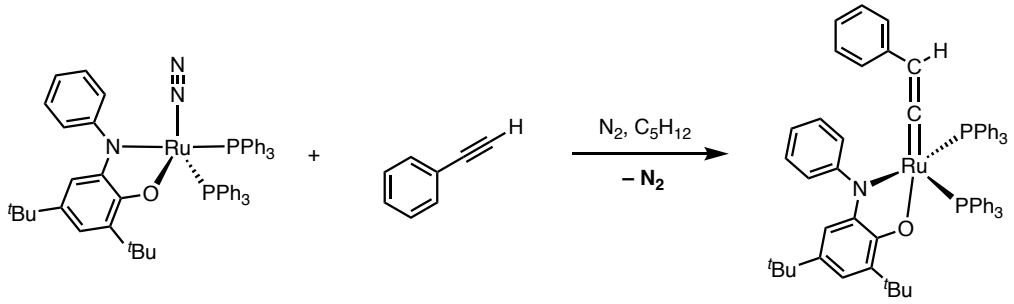

Scheme 3.5 Synthesis of the vinylidene complex **8**.

To study the reactivity of **1a** to unsaturated bonds, phenylacetylene was added. Unlike the expectation that the substrate would add η^2 similar to the ethylene complex reported in Chapter 2, a rearranged vinylidene complex **8** was isolated. The ^{1}H NMR of the complex in C_6D_6 shows a vinylidene proton at 3.96 ppm, as well as a distinctive carbene carbon in the

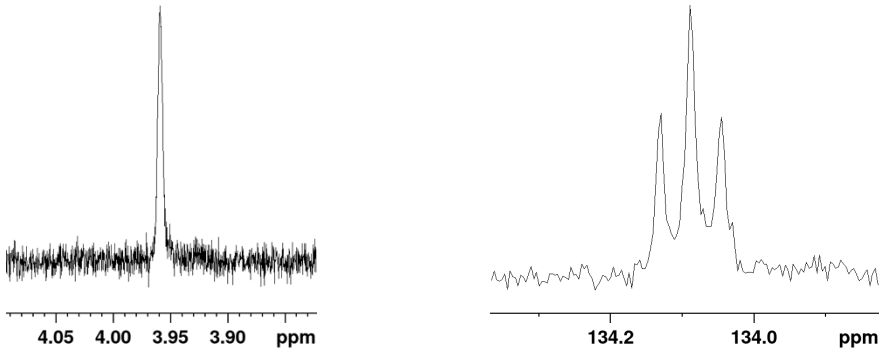

Figure 3.11 Zoomed ^{1}H NMR and ^{13}C[^{1}H] NMR of **8** displaying the vinylidene proton and the metal-bound carbon.

$^{13}C\{^{1}H\}$ NMR at 5.33 ppm coupled with the phosphines ($^{2}J_{PC}$ = 5.33 Hz) as presented in **Figure 3.11**. The vinylidene structure was also confirmed in the solid-state through X-ray diffractometry (**Figure 3.12**, **Table 3.5**). There were only minimal changes observed for the bond distances within the amidophenolate ligand compared to **1a**, expected from a singlet carbene. Similar rearrangement of acetylenes upon binding has been reported with Ru(II) complexes, which could also catalyze the coupling of bound acetylenes into enynes.[21]

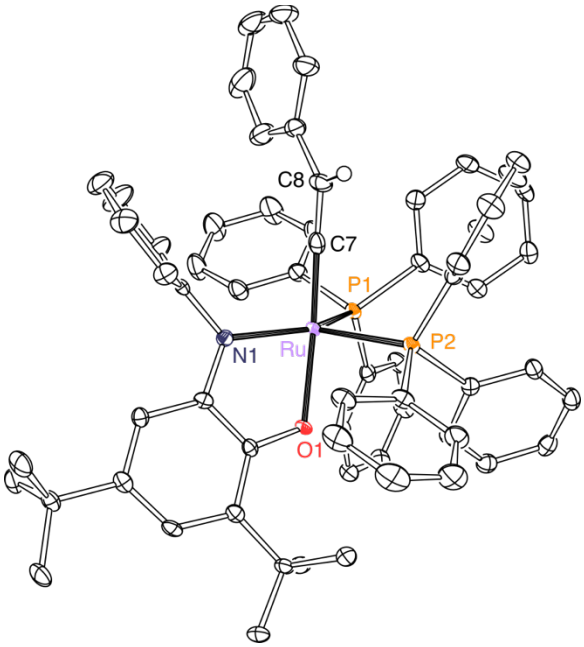

Figure 3.12 ORTEP diagram of **8** with thermal ellipsoids shown at 50 % probability. Hydrogen atoms and solvent molecules have been omitted for clarity.

Therefore, **1a** was also exposed to 20 equiv. phenylacetylene while the reaction was monitored with ^{1}H NMR. After heating at 70 °C for 4 days, the generation of two couples of new doublets at 5.73, 6.35 (J_{HH} = 12.00 Hz) and 5.64 and 5.70 ppm (J_{HH} = 1.00 Hz) was observed. The chemical shift and the coupling constants for the former set of peaks agreed with the literature value for Z-isomer of the 1,2-dipheylbut-1-ene-3-yne.[43] The latter is identified as the geminal constitutional isomer, but-3-en-1-yne-1,3-diyldibenzene.[44] Comparing the area under the alkene proton peaks of the products and the remaining phenylacetylene peak, the yield was 30 %. The ratio of the Z and geminal constitutional isomers calculated by the area underneath the doublets was 8:1.

3.3. Discussion

3.3.6. Chemical oxidation of 1a

Both one- and two-electron oxidation products were stable enough to be isolable. The g value of the singly oxidized **3b** closely matches that of a free iminosemiquinone radical, and the low energy transition in the UV-Vis spectra is consistent with a semiquinone π to π* intraligand charge-transfer. Therefore, **3b** is assigned as a ruthenium (II) with a ligand-centered radical. In contrast, the doubly oxidized **3c** exhibits a higher covalency between metal and ligand so that a definitive formal oxidation state assignment for either the metal or ligand becomes impractical. The calculated FMOs show substantial mixing between metal- and ligand-based orbitals, corroborating experimental evidence of increased covalency within the Ru-RAL framework. As a consequence, the two relatively reversible reduction events in the cyclic voltammetry of **3c** are assigned as Class D to Class C, and Class C to Class B Ru-RAL events without specifying the location of the electrons.

3.3.1. Hydrogenation

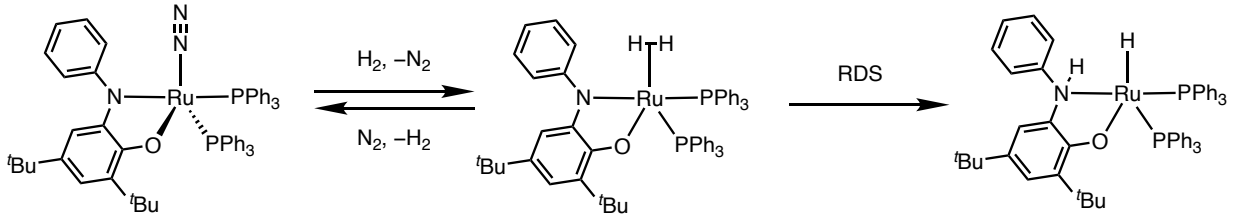

Scheme 3.6 Proposed mechanism of hydrogenation of **1a**.

The two new singlets at 5.48 and −7.08 ppm in the ^{1}H NMR assigned as N–H and Ru–H are reproducibly generated through gaseous H_2 addition to **1a**. However, the broadness of the singlets and the absence of the free H_2 signal which is expected to show at 4.47 ppm in C_6D_6 might be caused by rapid exchange between the hydride and free H_2 (**Figure 3.15**). The KIE of 2.13 suggests that the rate determining step involves a bond breaking between H_2, which would agree with the lack of free H_2 peak in the NMR, suggesting that there is a rapidly

generated intermediate undetectable in the NMR timescale. Regardless of the equivalents of the hydride on the metal, the singlet at 5.48 ppm is evidence that **1a** can heterolytically cleave an equivalent of H_2 using the basic nitrogen on the amidophenolate ligand.

The lack of stability of **1a** under gaseous H_2 makes it undesirable for catalytic hydrogenation. However, **1a** was able to catalytically transfer 5 equivalents of hydrogen in a proof-of-concept experiment. The increased efficiency upon reacting with transfer hydrogenation reagents could come from limiting the equivalents of hydride on the metal. The observed Ru–H and the absence of N–H in the ^{1}H NMR of the ammonia borane addition product could be evidence that the B–H bond is being activated through MLC, similar to a piano-stool molybdenum thiolate reported by Wang, Liao, and coworkers.[45] This would control the equivalents of hydrogen from reacting with the complex, preventing ligand hydrogenation.[46]

3.3.2. Reactivity with azide

Previous studies of transition metal nitrene transfer catalysts have invoked metal tetrazene formation as a possible intermediate step in nitrene transfer.[47,48] Some metal tetrazines are also known to be able to transfer a nitrene stoichiometrically to a substrate.[39,48] To test whether complex **7** is similarly reactive it was exposed substrates known to receive N-groups. However, no nitrene transfer was observed at temperatures up to 70 °C. Switching the order of addition so that the substrate was bound first to the complex lead to some generation of the nitrene transfer product observed in the ^{19}F NMR. Therefore, we suspect that once the tetrazene is formed, it is thermodynamically stable and does not perform nitrene transfer. The observed intermediate in the ^{1}H NMR could be the reactive imido species known in other transition metal nitrene transfer catalysts. However, there is a possibility that the intermediate is merely a low coordination number ruthenium species

generated after the loss of an equivalent of PPh_3, or a six-coordinate ruthenium species before the phosphine reacts with the azide. A possible mechanism for the latter is presented in **Scheme 3.7**, where a reactive ruthenium imido is suggested to form the tetrazene before losing an equivalent of PPh_3 which then reacts with the third equivalent of azide to form the iminophosphorane side product.

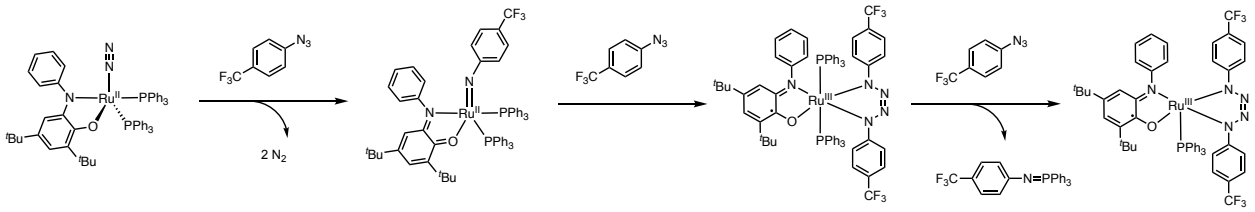

Scheme 3.7 A potential mechanism for generating the tetrazene product **7**.

3.3.3. Reactivity with phenylacetylene

Reaction of phenylacetylene with **1a** led to a vinylidene complex instead of the expected η^2-acetylene complex. The rearrangement of the acetylene to the vinylidene has been reported for d^6 metals before.[20] The relative stability of the vinylidene is known to depend on the electron density on the metal, due to the repulsion from the d orbitals of π symmetry to the filled π orbitals of the acetylene. DFT studies on a series of Ru(II) cyclopentadienyl species have shown that the increased electron density on the metal leads to the increase of the energy gap between the alkyne and vinylidene complexes.[49] Examples of bis-amidophenolate Ru(II) systems that can be isolated as the η^2-acetylene[50] prove that the single, fully reduced ligand donates enough electron density to shift the equilibrium to the vinylidene.

As expected from the ruthenium vinylidene complex **8**, complex **1a** was capable of phenylacetylene homocoupling into enynes. The steric hindrance from the triphenylphosphines seem to lead to the Z isomer selectively forming as the favored product.[51–53] The minor geminal product is known to be formed through pathways not involving vinylidene rearrangement, suggesting that the equilibrium between the vinylidene and acetylene complex could shift towards the acetylene in higher temperatures.

3.4. Conclusion

Ruthenium amidophenolate complexes were tested for hydrogenation and nitrene transfer. The N_2-bound $(N_2)Ru(^{Ph}ap)(PPh_3)_2$ showed evidence that it can heterolytically cleave H_2 as with other MLC hydrogenation catalysts albeit the instability under excess gaseous H_2. The results indicate promising reactivity towards heterolytically cleaving E–H bonds through MLC by using the amidophenolate nitrogen as the hydrogen acceptor. Attempts to perform nitrene transfer with the putative imido intermediate stabilized by the increased covalency between the metal and ligand was inconclusive, as the isolated tetrazene complex did not show reactivity. However, an intermediate species was observed through kinetic studies and partial conversion was achieved from switching the order of addition of the substrates, suggesting the possibility of a reactive intermediate. Kinetic studies with ^{19}F NMR could shed light on the identity of the observed intermediate, while increasing the steric bulk on the organic azide could be a viable strategy to prevent tetrazene formation and trap the imido. Complex **1** could also couple phenylacetylene selectively into the Z isomer enyne with a small impurity from the geminal isomer. The limited yield could be improved with less bulky phosphines or acetylenes.

3.5. Experimental

General Considerations. All manipulations were carried out using standard Schlenk-line techniques and glovebox techniques under nitrogen, except where noted. Hydrocarbon and ethereal solvents were sparged with argon before being deoxygenated and dried through activated Q5 and alumina columns. Such solvents were stored over activated molecular sieves in the glovebox. Deuterated solvents were dried over calcium hydride, distilled, and freeze-pump-thawed to remove dioxygen. Potassium hydride was obtained in mineral oil and washed with pentane prior to use. Tetrabutylammonium hexafluorophosphate (Acros) was recrystallized from ethanol three times and dried under vacuum before use. Ferrocene (Acros) was purified by vacuum sublimation. Tris(triphenylphosphine)ruthenium (II) dichloride (Sigma), ferrocenium hexafluorophosphate (Sigma), ferrocenium tetrafluoroborate (Sigma), dihydrogen (Airgas), carbon monoxide (Airgas), deuterium (Cambridge Isotope Laboratories), NH_3BH_3 (Sigma), and phenylacetylene (Sigma) was used as received. 4,6-di-tert-butyl-2-(phenylamino)phenol[32] and 1-azido-4-(trifluoromethyl)benzene[54] was prepared according to published procedures.

Spectroscopic and Electronic Characterization. All NMR spectroscopy was performed on a Bruker Avance 400, 500, or 600 MHz spectrometer at 298K. ^{1}H spectra were referenced to residual proteo impurities of the solvents (7.16 ppm, C6D6). ^{13}C NMR spectra were referenced to TMS using the natural ^{13}C abundance of the solvent. ^{31}P $\{^{1}H\}$ NMR were referenced with a phosphoric acid external standard (85%, 0.00 ppm). ^{19}F NMR were referenced with a trifluoro acetic acid external standard (85%, –76.55 ppm). All chemical shifts are reported using the standard notation in parts-per-million with positive shifts to higher frequency from given reference. Perpendicular-mode X-band EPR spectra were collected at 77 K and 298 K using a Bruker EMX spectrometer equipped with ER041XG

microwave bridge. The following spectrometer settings were used for 77 K: attenuation = 20 dB, microwave power 2.147 mW, frequency = 9.416 GHz, modulation amplitude = 4.000 G, gain = 30 dB, conversion time = 58.44 ms, time constant = 0.01 ms, sweep width 308.0 G and resolution 770 points. The following spectrometer settings were used for 298 K: attenuation = 20 dB, microwave power 2.154 mW, frequency = 9.837 GHz, modulation amplitude = 4.000 G, gain = 30 dB, conversion time = 76.01 ms, time constant = 0.01 ms, sweep width 236.8 G and resolution 592 points. The spectra were simulated using EasySpin for MATLAB.

Electronic absorption spectra were recorded using a PerkinElmer Lambda 800 absorption spectrometer using 10mm quartz cuvettes at ambient temperatures.

Cyclic voltammetry and differential pulse voltammetry experiments were performed on a Gamry G300 potentiostat/galvanosta/ZRA using a 3.0 mm glassy carbon working electrode, a platinum wire counter electrode, and a silver wire pseudo-reference electrode. Experiments were performed at ambient temperature in a dry nitrogen glovebox with 1 mM analyte and 100 mM $[NBu_4][PF_6]$ supporting electrolyte. All potentials were referenced to $[FeCp]^{+/0}$ using ferrocene as an internal standard.

Crystallographic Measurements. X-ray diffraction data were collected on single crystals mounted on glass fiber loops using Bruker CCD platform diffractometer equipped with a CCD detector at 143 K using Mo Kα (λ = 0.71073 Å) radiation, which was wavelength selected with a single-crystal graphite monochromator. A full sphere of data was collected for each crystal structure. The SMART program package was used to determine unit-cell parameters and to collect data. The raw frame data were processed using SAINT[55] and SADABS[56] to yield the reflection data files. Subsequent calculations were carried out using the SHELXTL[57] program suite. Structures were solved by direct methods and refined on F^2 by full-matrix least-squares techniques to convergence. Analytical scattering factors for neutral atoms[58] were used throughout the analyses. Hydrogen atoms, through visible in the

difference Fourier map, were generated at calculated positions and their positions refined using the riding model. ORTEP diagrams were generated using ORTEP-3 for Windows.[59] Bond distances were extracted in Mercury for Windows.

All DFT calculations were performed using Gaussian 16[60] employing B3LYP/LANL2DZ level of theory. VMD for Windows was used for 3D rendering of molecular orbitals.

Synthesis of $[(MeCN)_2Ru(^{Ph}ap)(PPh_3)_2][BF_4]$ (**3b**)

3a (0.05 g, 0.05 mmol, 1 equiv.) was suspended in 5 mL MeCN. To it, ferrocenium tetrafluoroborate (0.02 g, 0.05 mmol, 1 equiv.) dissolved in 4 mL MeCN was added dropwise. The mixture was stirred in ambient temperature for 1.5 hours. Volatiles were removed under vacuum and ferrocene was washed with 3x5 mL pentane to obtain dark purple solids in 94% yield (0.05 g). X-ray quality crystals were obtained from a layered THF solution with pentane. UV-vis (THF) λ_{max} / nm (ε / M^{-1} cm^{-1}): 375 (5000), 588 (5700), 856 (1600). EPR (X-band, $\perp$ mode, toluene, 77 K - 298 K): g = 1.9996.

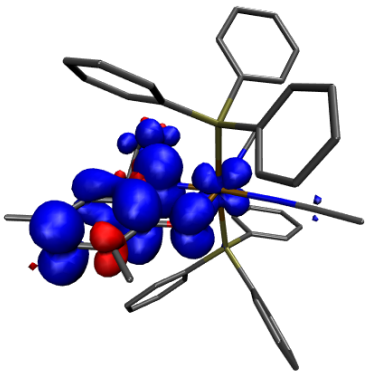

Figure 3.13 Spin density plot for **3b** with isovalues 0.0015.

Synthesis of $[(MeCN)_2Ru(^{Ph}ap)(PPh_3)_2][PF_6]_2$ (**3c**)

3a (0.04 g, 0.05 mmol, 1 equiv.) was suspended in 5 mL MeCN. To it, ferrocenium hexafluorophosphate (0.03 g, 0.09 mmol, 2 equiv.) dissolved in 4 mL was added dropwise. The mixture was stirred in ambient temperature for 1.5 hours. Volatiles were removed under vacuum and ferrocene was removed with 3x5 mL pentane wash to yield dark purple solids (0.05 g, 89% yield). X-ray quality crystals were obtained from a layered THF solution with pentane. ^{1}H NMR (CD_3CN, 500 MHz) δ/ppm: 1.13 (s, 9H, $C(CH_3)_3$), 1.36 (s, 9H, $C(CH_3)_3$), 1.47 (s, 3H, MeCN), 2.10 (s, 3H, MeCN), 5.92 (d, J = 7.0 Hz, 2H, N-Ph), 6.31 (br s, 1H, isq-H), 7.17 (dd, J = 5.7, 11.7 Hz, 12H, PPh_3) 7.33 (m, 2H, aryl-H), 7.41 (t, J = 7.6 Hz, 12H, PPh_3) 7.53 (m, 8H, aryl-H). $^{31}P\{^1H\}$ NMR (500 MHz) δ/ppm: 31.36 (s, PPh_3). UV-vis (THF) λ_{max} / nm (ε / M^{-1} cm^{-1}): 384 (4200), 536 (8800).

Table 3.6 X-ray diffraction data collection and refinement parameters for complexes **3b**, **3c**, **6-8**.

Complex	3b	3c	6	7	8
empirical formula	$C_{60}H_{61}N_3OP_2Ru \cdot (BF_4) \cdot (C_4H_8O)$	$C_{60}H_{61}N_3OP_2Ru \cdot 2(PF_6) \cdot 0.5(C_4H_8O) \cdot 0.5(C_4H_{10}O)$	$C_{56}H_{56}N_3OP_2Ru \cdot (BF_4) \cdot (C_4H_{10}O)$	$C_{52}H_{48}F_6N_5OPRu$	$C_{64}H_{61}NOP_2Ru \cdot (C_5H_{12})$
formula weight	1162.04	1366.18	1110.97	1044.99	1095.29
crystal system	Monoclinic	Monoclinic	Monoclinic	Triclinic	Monoclinic
space group	$P2_1/n$	Cc	$P2_1/n$	$P1$	$P2_1/n$
T / K	93.15	92.85	93.15	100(2)	92.85
***a* / Å**	15.1801(9)	45.555(2)	16.7805(13)	9.8794(5)	16.6319(14)
***b* / Å**	16.7704(12)	17.7237(9)	19.0026(14)	14.7368(7)	16.7258(13)
***c* / Å**	22.1582(12)	16.7328(8)	18.0334(14)	17.8308(8)	20.5471(16)
***α* / °**	90	90	90	96.573(2)	90
***β* / °**	95.968(3)	107.727(2)	108.4842(12)	99.547(3)	93.459(4)
***γ* / °**	90	90	90	107.982(2)	90
***V* / Å^3**	5610.4(6)	12868.5(11)	5453.7(7)	2396.7(2)	5705.4(8)
Z	4	8	4	2	4
refl. collected	92068	82996	140763	40129	82240
Data/restraints/parameters	17101 / 21 / 697	22210 / 97 / 1556	16645 / 0 / 670	9040 / 0 / 595	10396 / 0 / 675
R1 (*I* > 2*σ*)[a]	0.0339	0.0471	0.0308	0.0346	0.0345
***w*R2 (all data)[b]**	0.0877	0.1255	0.0811	0.0848	0.0875
***GOF*[c]**	1.027	1.048	1.031	1.049	1.035

[a] $R1 = \Sigma | |F_o| - |F_c| | / \Sigma |F_o|$; [b] $wR2 = [\Sigma[w(F_o^2 - F_c^2)^2] / \Sigma[w(F_o^2)^2]]^{1/2}$ [c] Goodness of Fit $= S = [\Sigma [w(F_o^2 - F_c^2)^2] / (n-p)]^{1/2}$ where n is the number of reflections and p is the total number of parameters refined.

Addition of 1 atm H_2 to **1a**

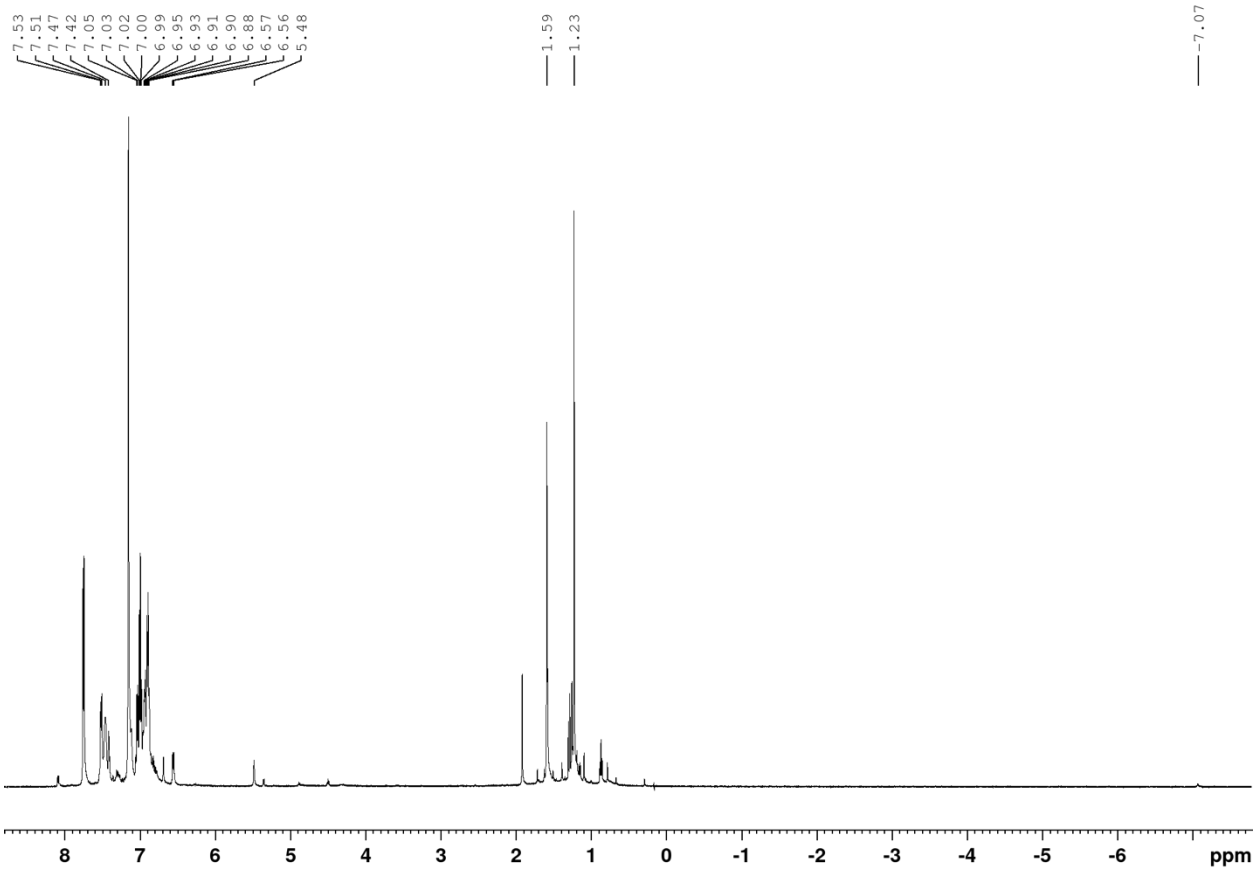

Figure 3.14 ^{1}H NMR of the H_2 addition product to **1a** in C_6D_6.

6.8 mM solution of **1a** in 1 mL C_6D_6 with 0.2 mM HMB as the reference was added to a borosilicate NMR tube with a J-Young cap. The solution was subjected to two freeze-pump-thaw cycles and was frozen again. The headspace was evacuated once more before being exposed to 1 atm of H_2. The frozen sample was kept in liquid nitrogen until it was ready to be thawed. The solution was thawed and shaken before the first ^{1}H NMR measurement. Subsequent measurements were taken in 5-minute intervals without adjusting the lock and shim.

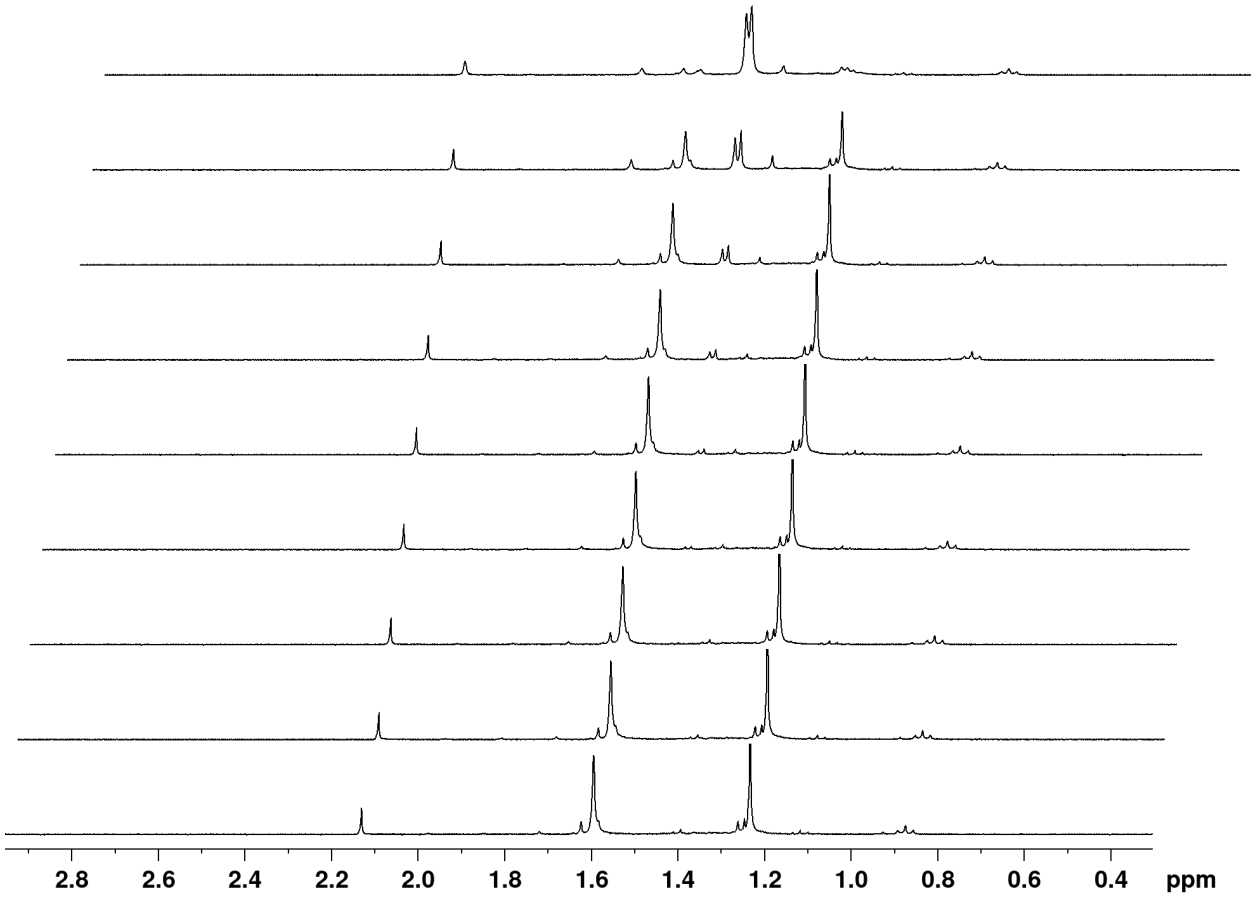

Figure 3.15 ^{1}H NMR spectrum of **1a** with the addition of 1 atm H_2.

Hydrogenation studies

In a J-Young cap fitted NMR tube, a 0.5 mL C_6D_6 solution with 0.004 M **1a**, 0.004 M benzaldehyde, and 0.0002 M hexamethylbenzene was added. After 3 freeze-pump-thaw cycles, 1 atm of gaseous H_2 was introduced to the NMR tube. The tube was sealed and left to react at 25 °C. The reaction was monitored by ^{1}H NMR.

Transfer hydrogenation study

In 10 mL THF, **1a** (0.067 g, 0.071 mmol, 1 equiv.) and NH_3BH_3 (0.010 g, 0.31 mmol, 4.5 equiv.) was dissolved. To the solution, trans-stilbene (0.057 g, 0.316 mmol, 4.48 equiv.)

was added. The reaction was stirred at 25 °C and aliquots were removed to monitor the reaction through ^{1}H NMR.

Synthesis of [(N_2)Ru(^{Ph}apH)(PPh_3)$_2$][BF_4] (**6**)

1a (0.095 g, 0.10 mmol, 1 equiv.) was dissolved in 20 mL Et_2O in a 50 mL Schlenk flask under dinitrogen atmosphere. Through a septum, tetrafluoroboric acid-diethyl ether complex (13 uL, 0.10 mmol, 1 equiv.) was added dropwise. The color of the solution changed from deep purple to deep bluish violet within 10 seconds. The solution was transferred into a nitrogen glovebox and was concentrated under vacuum. ^{1}H NMR (C_6D_6, 500 MHz) δ/ppm: 1.23 (s, 9H, $C(CH_3)_3$), 1.62 (s, 9H, $C(CH_3)_3$), 6.89-6.98 (m, aryl-H), 7.30-7.50 (m, aryl-H) 10.14 (d, J = 4.0 Hz, 1H, N-H).

Synthesis of Ru(^{Ph}ap)(PPh_3)[(4-$CF_3C_6H_4$)NNNN(4-$CF_3C_6H_4$)] (**7**)

1a (0.067 g, 0.065 mmol, 1 equiv.) was dissolved in a mixture of 5 mL pentane and 5 mL benzene. To it, 1-azido-4-(trifluoromethyl)benzene (40 uL, 0.28 mmol, 4.4 equiv.) was added with a microsyringe. The solution was stirred overnight before being concentrated down into a solid under vacuum. The product was extracted with pentane and recrystallized at –40 °C to obtain the product as brown solids (0.040 g, 61.7 % yield). X-ray quality crystals were obtained from chilled pentane solution. ^{1}H NMR (C_6D_6, 500 MHz) δ/ppm: 1.26 (s, 9H, $C(CH_3)_3$), 1.37 (s, 9H, $C(CH_3)_3$), 5.97 (d, J = 8.3 Hz, 1H, aryl-H), 6.64-6.91 (m, aryl-H), 7.25 (d, J = 8.5 Hz, 1H, aryl-H), 7.29 (d, J = 2.2 Hz, 2H, aryl-H), 7.41 (d, J = 2.0 Hz, 2H, aryl-H) 7.90 (m, aryl-H). ^{31}P{^{1}H} NMR (500 MHz) δ/ppm: 48.59 (s, PPh_3). 19F NMR (500 MHz) δ/ppm: −61.73, −61.62.

Synthesis of Ru(^{Ph}ap)(PPh_3)$_2$(CCHPh) (**8**)

1a (0.209 g, 0.115 mmol, 1 equiv.) was dissolved in 10 mL benzene. To the solution, phenylacetylene (12.6 µL, 0.115 mmol, 1 equiv.) was added with a 10 uL microsyringe. The solution was stirred overnight before being concentrated into a solid. The residue was dissolved in pentane and filtered through a filter pipette. A film was formed after chilling the solution, which was collected through decanting the mother liquor and removing volatiles *in vacuo*. The product was collected as a purple film (0.049 g, 40.7 %). X-ray quality crystals were obtained from chilled pentane solution. ^{1}H NMR (C_6D_6, 500 MHz) δ/ppm: 1.39 (s, 9H, $C(CH_3)_3$), 1.54 (s, 9H, $C(CH_3)_3$), 3.96 (s, 1H, RuCCH), 6.47 (d, aryl-H), 6.80-6.93 (m, aryl-H), 7.22-7.25 (m, aryl-H), 7.47-7.51 (m, aryl-H). ^{13}C NMR (C6D6, 500 MHz) δ/ppm: 134.09 (t, $^{2}J_{PC}$ = 5.3 Hz, Ru–C). ^{31}P{^{1}H} NMR (500 MHz) δ/ppm: 49.31 (s, PPh_3).

Phenylacetylene homocoupling reaction

0.1 mL of a C_6D_6 solution with 0.004 M of **1a** (4 µmol, 1 equiv.) and 0.01 M of hexamethylbenzene (reference) was added to an NMR tube with a J-Young fitted cap. To it, 4.4 uL of phenylacetylene (40 µmol, 11 equiv.) was added. The solution was diluted with about 0.5 mL C_6D_6. The solution was heated at 70 °C over 5 days while being monitored by NMR.

3.6. References

(1) Ramspoth, T.-F.; Kootstra, J.; Harutyunyan, S. R. Unlocking the Potential of Metal Ligand Cooperation for Enantioselective Transformations. *Chem. Soc. Rev.* **2024**, *53* (7), 3216–3223. https://doi.org/10.1039/D3CS00998J.

(2) Khusnutdinova, J. R.; Milstein, D. Metal–Ligand Cooperation. *Angew. Chem. Int. Ed.* **2015**, *54* (42), 12236–12273. https://doi.org/10.1002/anie.201503873.

(3) Mondal, R.; Guin, A. K.; Chakraborty, G.; Paul, N. D. Metal–Ligand Cooperative Approaches in Homogeneous Catalysis Using Transition Metal Complex Catalysts of Redox Noninnocent Ligands. *Org. Biomol. Chem.* **2022**, *20* (2), 296–328. https://doi.org/10.1039/D1OB01153G.

(4) Dub, P. A.; Gordon, J. C. Metal–Ligand Bifunctional Catalysis: The "Accepted" Mechanism, the Issue of Concertedness, and the Function of the Ligand in Catalytic Cycles Involving Hydrogen Atoms. *ACS Catal.* **2017**, *7* (10), 6635–6655. https://doi.org/10.1021/acscatal.7b01791.

(5) Shvo, Youval.; Czarkie, Dorotha.; Rahamim, Yocheved.; Chodosh, D. F. A New Group of Ruthenium Complexes: Structure and Catalysis. *J. Am. Chem. Soc.* **1986**, *108* (23), 7400–7402. https://doi.org/10.1021/ja00283a041.

(6) Higashi, T.; Kusumoto, S.; Nozaki, K. Cleavage of Si–H, B–H, and C–H Bonds by Metal–Ligand Cooperation: Focus Review. *Chem. Rev.* **2019**, *119* (18), 10393–10402. https://doi.org/10.1021/acs.chemrev.9b00262.

(7) Hesp, K. D.; McDonald, R.; Ferguson, M. J.; Stradiotto, M. New Cationic and Zwitterionic Cp*M(κ² -P,S) Complexes (M = Rh, Ir): Divergent Reactivity Pathways Arising from Alternative Modes of Ancillary Ligand Participation in Substrate Activation. *J. Am. Chem. Soc.* **2008**, *130* (48), 16394–16406. https://doi.org/10.1021/ja8062277.

(8) Stahl, T.; Müther, K.; Ohki, Y.; Tatsumi, K.; Oestreich, M. Catalytic Generation of Borenium Ions by Cooperative B–H Bond Activation: The Elusive Direct Electrophilic Borylation of Nitrogen Heterocycles with Pinacolborane. *J. Am. Chem. Soc.* **2013**, *135* (30), 10978–10981. https://doi.org/10.1021/ja405925w.

(9) Stahl, T.; Hrobárik, P.; Königs, C. D. F.; Ohki, Y.; Tatsumi, K.; Kemper, S.; Kaupp, M.; Klare, H. F. T.; Oestreich, M. Mechanism of the Cooperative Si–H Bond Activation at Ru–S Bonds. *Chem. Sci.* **2015**, *6* (7), 4324–4334. https://doi.org/10.1039/C5SC01035G.

(10) Charette, B. J.; Ziller, J. W.; Heyduk, A. F. Exploring Ligand-Centered Hydride and H-Atom Transfer. *Inorg. Chem.* **2021**, *60* (7), 5367–5375. https://doi.org/10.1021/acs.inorgchem.1c00351.

(11) Charette, B. J.; Ziller, J. W.; Heyduk, A. F. Metal-Ion Influence on Ligand-Centered Hydrogen-Atom Transfer. *Inorg. Chem.* **2021**, *60* (3), 1579–1589. https://doi.org/10.1021/acs.inorgchem.0c02981.

(12) Rosenkoetter, K. E.; Wojnar, M. K.; Charette, B. J.; Ziller, J. W.; Heyduk, A. F. Hydrogen-Atom Noninnocence of a Tridentate [SNS] Pincer Ligand. *Inorg. Chem.* **2018**, *57* (16), 9728–9737. https://doi.org/10.1021/acs.inorgchem.8b00618.

(13) Paik, J.; Choe, J. H.; Padmanaban, S.; Seo, M.; Yoo, C.-J.; Lee, H. B.; Lee, Y. Thermodynamic Hydricity of a Ruthenium CO_2 Hydrogenation Catalyst Supported by a Rigid PNP Pincer. *JACS Au* **2025**, *5* (2), 811–821. https://doi.org/10.1021/jacsau.4c01078.

(14) Ishikawa, M.; Ohshita, J.; Ito, Y.; Minato, A. Palladium-Catalyzed Synthesis of Silyl-Substituted Enynes. *J. Organomet. Chem.* **1988**, *346* (3), C58–C60. https://doi.org/10.1016/0022-328X(88)80147-5.

(15) Singer, H.; Wilkinson, G. The Dimerisation of Monosubstituted α-Hydroxyacetylenes by Use of Tris(Triphenylphosphine)Chlororhodium(I) as Catalyst. *J Chem Soc A* **1968**, No. 0, 849–853. https://doi.org/10.1039/J19680000849.

(16) Kovalev, I. P.; Yevdakov, K. V.; Strelenko, Yu. A.; Vinogradov, M. G.; Nikishin, G. I. Dimerization of 1-Alkynes Catalyzed by RhCl(PMe3)3. Isolation of the Intermediate (Alkynyl)(Vinyl)Rhodium(III) Complexes. *J. Organomet. Chem.* **1990**, *386* (1), 139–146. https://doi.org/10.1016/0022-328X(90)80262-X.

(17) Ohshita, J.; Furumori, K.; Matsuguchi, A.; Ishikawa, M. Synthesis and Reactions of (E)-1,4-Bis(Silyl)-Substituted Enynes. *J. Org. Chem.* **1990**, *55* (10), 3277–3280. https://doi.org/10.1021/jo00297a054.

(18) Sabourin, E. T. The Selective Head-to-Tail Dimerization of α-Hydroxy Terminal Acetylenes. *J. Mol. Catal.* **1984**, *26* (3), 363–373. https://doi.org/10.1016/0304-5102(84)85110-X.

(19) Trost, B. M.; Chan, C.; Ruhter, G. Metal-Mediated Approach to Enynes. *J. Am. Chem. Soc.* **1987**, *109* (11), 3486–3487. https://doi.org/10.1021/ja00245a064.

(20) Bruce, M. I. Organometallic Chemistry of Vinylidene and Related Unsaturated Carbenes. *Chem. Rev.* **1991**, *91* (2), 197–257. https://doi.org/10.1021/cr00002a005.

(21) Trost, B. M.; Masters, J. T. Transition Metal-Catalyzed Couplings of Alkynes to 1,3-Enynes: Modern Methods and Synthetic Applications. *Chem. Soc. Rev.* **2016**, *45* (8), 2212–2238. https://doi.org/10.1039/C5CS00892A.

(22) Bianchini, C.; Peruzzini, M.; Zanobini, F.; Frediani, P.; Albinati, A. A Ruthenium(II) Enynyl Complex Mediates the Catalytic Dimerization of 1-Alkynes to Z-1,4-Disubstituted Enynes. *J. Am. Chem. Soc.* **1991**, *113* (14), 5453–5454. https://doi.org/10.1021/ja00014a047.

(23) Bianchini, C.; Frediani, P.; Masi, D.; Peruzzini, M.; Zanobini, F. Regio- and Stereoselective Dimerization of Phenylacetylene to (Z)-1,4-Diphenylbut-3-En-1-Yne by Ruthenium(II) Catalysis. Reaction Mechanism Involving Intermolecular Protonation of .Sigma.-Alkynyl by 1-Alkyne. *Organometallics* **1994**, *13* (11), 4616–4632. https://doi.org/10.1021/om00023a074.

(24) Wakatsuki, Y.; Koga, N.; Yamazaki, H.; Morokuma, K. Acetylene .Pi.-Coordination, Slippage to .Sigma.-Coordination, and 1,2-Hydrogen Migration Taking Place on a Transition Metal. The Case of a Ru(II) Complex as Studied by Experiment and Ab Initio Molecular Orbital Simulations. *J. Am. Chem. Soc.* **1994**, *116* (18), 8105–8111. https://doi.org/10.1021/ja00097a017.

(25) Yamazaki, H. Novel Catalytic Dimerization of T-Butylacetylene to Trans-1,4-Di-t-Butylbutatriene. *J Chem Soc Chem Commun* **1976**, No. 21, 841–842. https://doi.org/10.1039/C39760000841.

(26) Cadierno, V.; Gamasa, M. P.; Gimeno, J.; González-Bernardo, C.; Pérez-Carreño, E.; García-Granda, S. Reactivity of Indenyl−Ruthenium(II) Vinylidene Complexes: Selective Synthesis of Alkenyl−Phosphonio Derivatives via Nucleophilic Addition of Triphenylphosphine on Their η^2 -Alkyne Tautomers. Theoretical Study of the η^1 -Vinylidene−η^2 -Alkyne Tautomerization. *Organometallics* **2001**, *20* (24), 5177–5188. https://doi.org/10.1021/om010308e.

(27) Nguyen, A. I.; Zarkesh, R. A.; Lacy, D. C.; Thorson, M. K.; Heyduk, A. F. Catalytic Nitrene Transfer by a Zirconium(IV) Redox-Active Ligand Complex. *Chem Sci* **2011**, *2* (1), 166–169. https://doi.org/10.1039/C0SC00414F.

(28) Charette, B. J. Investigations into the Reactivity of Transition Metal Complexes with Redox-Active Ligands for Proton Coupled Electron Transfer and Nitrene Transfer, University of California, Irvine, 2021. https://escholarship.org/uc/item/2p70w8nm.

(29) Carter, S. M.; Sia, A.; Shaw, M. J.; Heyduk, A. F. Isolation and Characterization of a Neutral Imino-Semiquinone Radical. *J. Am. Chem. Soc.* **2008**, *130* (18), 5838–5839. https://doi.org/10.1021/ja711185s.

(30) Connelly, N. G.; Manners, I.; Protheroe, J. R. C.; Whiteley, M. W. Reduction-Ox Idation Properties of 0rganotransit Ion-metaI Complexes. Part 19.' Carbonylruthenium Catecholate and Semiquinone Complexes.

(31) Bhattacharya, S.; Pierpont, C. G. Structure and Bonding in Bis(Quinone) Complexes of Ruthenium. Synthesis and Characterization of the Ru(PPh3)2(SQ)2 (SQ = 3,5-Di-Ferf -Butylsemiquinone, Tetrachloro- 1,2-Semiquinone) Series.

(32) Chaudhuri, P.; Verani, C. N.; Bill, E.; Bothe, E.; Weyhermüller, T.; Wieghardt, K. Electronic Structure of Bis(*o* -Iminobenzosemiquinonato)Metal Complexes (Cu, Ni, Pd). The Art of Establishing Physical Oxidation States in Transition-Metal Complexes Containing Radical Ligands. *J. Am. Chem. Soc.* **2001**, *123* (10), 2213–2223. https://doi.org/10.1021/ja003831d.

(33) Das, D.; Das, A. K.; Sarkar, B.; Mondal, T. K.; Mobin, S. M.; Fiedler, J.; Záliš, S.; Urbanos, F. A.; Jiménez-Aparicio, R.; Kaim, W.; Lahiri, G. K. The Semiquinone−Ruthenium Combination as a Remarkably Invariant Feature in the Redox and Substitution Series $[Ru(Q)_n(Acac)_{3-n}]^m$, n = 1−3; m = (−2), −1, 0, +1, (+2); Q = 4,6-Di- *Tert* -Butyl- *N* -Phenyl- *o* -Iminobenzoquinone. *Inorg. Chem.* **2009**, *48* (24), 11853–11864. https://doi.org/10.1021/ic901900g.

(34) Brown, S. N. Metrical Oxidation States of 2-Amidophenoxide and Catecholate Ligands: Structural Signatures of Metal–Ligand π Bonding in Potentially Noninnocent Ligands. *Inorg. Chem.* **2012**, *51* (3), 1251–1260. https://doi.org/10.1021/ic202764j.

(35) Das, D.; Mondal, T. K.; Chowdhury, A. D.; Weisser, F.; Schweinfurth, D.; Sarkar, B.; Mobin, S. M.; Urbanos, F. A.; Jiménez-Aparicio, R.; Lahiri, G. K. Valence and Spin Situations in Isomeric [(Bpy)Ru(Q′)2]n (Q′ = 3,5-Di-Tert-Butyl-N-Aryl-1,2-Benzoquinonemonoimine). An Experimental and DFT Analysis. *Dalton Trans.* **2011**, *40* (33), 8377. https://doi.org/10.1039/c1dt10609k.

(36) Gianino, J.; Brown, S. N. Highly Covalent Metal–Ligand π Bonding in Chelated Bis- and Tris(Iminoxolene) Complexes of Osmium and Ruthenium. *Dalton Trans.* **2020**, *49* (21), 7015–7027. https://doi.org/10.1039/D0DT01287D.

(37) Vanicek, S.; Jochriem, M.; Hassenrück, C.; Roy, S.; Kopacka, H.; Wurst, K.; Müller, T.; Winter, R. F.; Reisner, E.; Bildstein, B. Redox-Rich Metallocene Tetrazene Complexes: Synthesis, Structure, Electrochemistry, and Catalysis. *Organometallics* **2019**, *38* (6), 1361–1371. https://doi.org/10.1021/acs.organomet.8b00681.

(38) Heyduk, A. F.; Driver, T. G.; Labinger, J. A.; Bercaw, J. E. Kinetic and Thermodynamic Preferences in Aryl vs Benzylic C−H Bond Activation with Cationic Pt(II) Complexes. *J. Am. Chem. Soc.* **2004**, *126* (46), 15034–15035. https://doi.org/10.1021/ja045078k.

(39) Isbill, S. B.; Chandrachud, P. P.; Kern, J. L.; Jenkins, D. M.; Roy, S. Elucidation of the Reaction Mechanism of C_2 + N_1 Aziridination from Tetracarbene Iron Catalysts. *ACS Catal.* **2019**, *9* (7), 6223–6233. https://doi.org/10.1021/acscatal.9b01306.

(40) Overbosch, P.; Van Koten, G.; Overbeek, O. Synthesis and Reactivity of Bis(1,4-Diaryltetraazabutadiene)Nickel Complexes. Crystal and Molecular Structure of Bis[1,4-Bis(3,5-Dimethylphenyl)Tetraazabutadiene]Nickel. *Inorg. Chem.* **1982**, *21* (6), 2373–2378. https://doi.org/10.1021/ic00136a051.

(41) Overbosch, P.; Van Koten, G.; Spek, A. L.; Roelofsen, G.; Duisenberg, A. J. M. Synthesis, Reactivity, and Crystal Structure of [1,4-Bis(4-Tolyl)Tetraazabutadiene](.Eta.5-Cyclopentadienyl)Nickel. *Inorg. Chem.* **1982**, *21* (11), 3908–3913. https://doi.org/10.1021/ic00141a010.

(42) Vaddypally, S.; McKendry, I. G.; Tomlinson, W.; Hooper, J. P.; Zdilla, M. J. Electronic Structure of Manganese Complexes of the Redox-Non-Innocent Tetrazene Ligand and Evidence for the Metal-Azide/Imido Cycloaddition Intermediate. *Chem. – Eur. J.* **2016**, *22* (30), 10548–10557. https://doi.org/10.1002/chem.201600531.

(43) Bhunia, M.; Sahoo, S. R.; Vijaykumar, G.; Adhikari, D.; Mandal, S. K. Cyclic (Alkyl)Amino Carbene Based Iron Catalyst for Regioselective Dimerization of Terminal Arylalkynes. *Organometallics* **2016**, *35* (21), 3775–3780. https://doi.org/10.1021/acs.organomet.6b00703.

(44) Liang, Q.; Sheng, K.; Salmon, A.; Zhou, V. Y.; Song, D. Active Iron(II) Catalysts toward *Gem* -Specific Dimerization of Terminal Alkynes. *ACS Catal.* **2019**, *9* (2), 810–818. https://doi.org/10.1021/acscatal.8b03552.

(45) Hou, S.-F.; Chen, J.-Y.; Xue, M.; Jia, M.; Zhai, X.; Liao, R.-Z.; Tung, C.-H.; Wang, W. Cooperative Molybdenum-Thiolate Reactivity for Transfer Hydrogenation of Nitriles. *ACS Catal.* **2020**, *10* (1), 380–390. https://doi.org/10.1021/acscatal.9b04455.

(46) Lau, S.; Gasperini, D.; Webster, R. L. Amine–Boranes as Transfer Hydrogenation and Hydrogenation Reagents: A Mechanistic Perspective. *Angew. Chem. Int. Ed.* **2021**, *60* (26), 14272–14294. https://doi.org/10.1002/anie.202010835.

(47) Russell, J. J.; DeJesus, J. F.; Smith, B. A.; Nalaoh, P.; Vogiatzis, K. D.; Jenkins, D. M. Disparate Reactivity of a Chiral Iron(II) Tetracarbene Complex with Organic Azides. *Dalton Trans.* **2024**, *53* (26), 10819–10823. https://doi.org/10.1039/D4DT01422G.

(48) Cramer, S. A.; Hernández Sánchez, R.; Brakhage, D. F.; Jenkins, D. M. Probing the Role of an Fe^{IV} Tetrazene in Catalytic Aziridination. *Chem Commun* **2014**, *50* (90), 13967–13970. https://doi.org/10.1039/C4CC05124F.

(49) De Angelis, F.; Sgamellotti, A.; Re, N. Acetylene to Vinylidene Rearrangements on Electron Rich D6 Metal Centers: A Density Functional Study. *Dalton Trans.* **2004**, No. 20, 3225. https://doi.org/10.1039/b408452g.

(50) Ayson, P. R. H.; Brown, S. N. Anisotropic π Bonding in Bis(Iminoxolene)Ruthenium: Consequences for Alkene and Alkyne Binding. *Organometallics* **2024**, *43* (17), 1889–1903. https://doi.org/10.1021/acs.organomet.4c00259.

(51) Wakatsuki, Y.; Yamazaki, H.; Kumegawa, N.; Satoh, T.; Satoh, J. Y. Regio- and Stereocontrolled Dimerization of Tert-Butylacetylene to (Z)-1,4-Di-Tert-Butylbutatriene by Ruthenium Catalysis. Reaction Mechanism Involving Alkynyl-Vinylidene Coupling and Rearrangement of the Metal-Bound C4 Unit. *J. Am. Chem. Soc.* **1991**, *113* (25), 9604–9610. https://doi.org/10.1021/ja00025a027.

(52) Yi, C. S.; Liu, N. Homogeneous Catalytic Dimerization of Terminal Alkynes by $C_5Me_5Ru(L)H_3$ (L = PPh_3 , PCy_3 , PMe_3). *Organometallics* **1996**, *15* (19), 3968–3971. https://doi.org/10.1021/om9601110.

(53) Slugovc, C.; Mereiter, K.; Zobetz, E.; Schmid, R.; Kirchner, K. Ruthenium-Catalyzed Dimerization of Terminal Alkynes Initiated by a Neutral Vinylidene Complex. *Organometallics* **1996**, *15* (25), 5275–5277. https://doi.org/10.1021/om9607816.

(54) Dai, Z.-C.; Chen, Y.-F.; Zhang, M.; Li, S.-K.; Yang, T.-T.; Shen, L.; Wang, J.-X.; Qian, S.-S.; Zhu, H.-L.; Ye, Y.-H. Synthesis and Antifungal Activity of 1,2,3-Triazole Phenylhydrazone Derivatives. *Org Biomol Chem* **2015**, *13* (2), 477–486. https://doi.org/10.1039/C4OB01758G.

(55) Bruker AXS, Inc. SAINT, 2013.

(56) Sheldrick, G. M.; Bruker AXS, Inc. SADABS.

(57) Sheldrick, G. M. SHELXTL, 2001.

(58) *International Tables Fo rX-Ray Crystallography*; Kluwer Academic: Dordrecht, Netherlands, 1992.

(59) Farrugia, L. J. ORTEP-3 for Windows - a Version of ORTEP-III with a Graphical User Interface (GUI). *J. Appl. Crystallogr.* **1997**, *30* (5–1), 565–565. https://doi.org/10.1107/S0021889897003117.

(60) Frisch, M. J.; Trucks, G. W.; Schlegel, H. B.; Scuseria, G. E.; Robb, M. A.; Cheeseman, J. R.; Scalmani, G.; Barone, V.; Petersson, G. A.; Nakatsuji, H.; Li, X.; Caricato, M.; Marenich, A. V.; Bloino, J.; Janesko, B. G.; Gomperts, R.; Mennucci, B.; Hratchian, H. P.; Ortiz, J. V.; Izmaylov, A. F.; Sonnenberg, J. L.; Williams; Ding, F.; Lipparini, F.; Egidi, F.; Goings, J.; Peng, B.; Petrone, A.; Henderson, T.; Ranasinghe, D.; Zakrzewski, V. G.; Gao, J.; Rega, N.; Zheng, G.; Liang, W.; Hada, M.; Ehara, M.; Toyota, K.; Fukuda, R.; Hasegawa, J.; Ishida, M.; Nakajima, T.; Honda, Y.; Kitao, O.; Nakai, H.; Vreven, T.; Throssell, K.; Montgomery Jr., J. A.; Peralta, J. E.; Ogliaro, F.; Bearpark, M. J.; Heyd, J. J.; Brothers, E. N.; Kudin, K. N.; Staroverov, V. N.; Keith, T. A.; Kobayashi, R.; Normand, J.; Raghavachari, K.; Rendell, A. P.; Burant, J. C.; Iyengar, S. S.; Tomasi, J.; Cossi, M.; Millam, J. M.; Klene, M.; Adamo, C.; Cammi, R.; Ochterski, J. W.; Martin, R. L.; Morokuma, K.; Farkas, O.; Foresman, J. B.; Fox, D. J. Gaussian 16 Rev. C.01, 2016.

Chapter 4: Charge Transfer Complexes of Titanium(IV) and Zirconium(IV)

4.1. Introduction

The efficient conversion of solar energy to electricity is crucial in addressing increasing global energy demand and climate change.[1] Within strategies to convert sunlight into electricity, dye-sensitized solar cells (DSSCs) that utilize molecular charge-transfer dyes have been studied extensively due to advantages such as cost-effectiveness and ease of production.[2–4] A type of common dye used in DSSCs is the porphyrin-based triad dye, in which the porphyrin moiety acts as a photosensitizer by absorbing a photon to excite an electron from the π orbital to the π* orbital within the porphyrin.[5,6] The electron in the excited state is then transferred to an electron acceptor such as a fullerene, while an electron from a donor

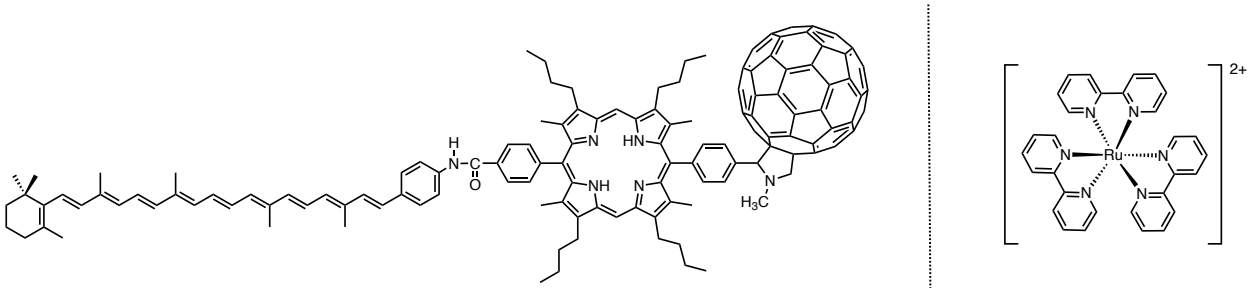

Scheme 4.1 The structures of a carotene-porphyrin-fullerene triad charge-transfer dye molecule and $[Ru(bpy)_3]^{2+}$ MLCT dye. The porphyrin acts as a photosensitizer which initiates the electron-hole separation. The carotene is the electron donor, and the fullerene electron acceptor. In the $[Ru(bpy)_3]^{2+}$, the charge-transfer occurs from the metal to the bipyridine ligand.

such as carotene is transferred to the hole in the partially filled SOMO–1 of the excited state porphyrin. An advantage of this system is that the charge is separated over a long distance, which allows the charge separation state to be long lived. However, there is energy loss in the thermal transfer of the electron from the excited state porphyrin to the electron acceptor moiety, which decreases the efficiency of this system.[7,8]

Early studies to overcome such energy loss involved strategies to localize the HOMO and LUMO on different parts of the molecule as with $[Ru(bpy)_3]^{2+}$.[9,10] The photoinduced charge transfer occurs from the ruthenium(II) d orbitals to the π* orbitals of the bipyridine ligand. In addition to the increased efficiency, the metal-to-ligand charge-trasfer (MLCT) dye is easier to synthesize and customize than the organic dyes.[11] The ability to customize the absorption profile of the dye is especially useful in tandem DSSCs, in which two dyes of complementary absorption profiles in the visible region is used in tandem to increase the efficiency of energy conversion.[3,12–14] However, the distance of the charge transfer is shorter, increasing the probability of rapid recombination of the electron-hole pair to the ground state. To combine the longer charge separation of the triad and the customizability the MLCT dyes, ligand-to-ligand charge transfer (LL′CT) complexes have been designed.[15–17] In these complexes, the HOMO and LUMO reside on different ligands that act as an electron donor and acceptor, respectively. Redox-active ligands have the ability to undergo oxidations and reductions while remaining bound to the metal, making them a focus of charge-transfer complexes. Square planar LLCT complexes have been intensively studied for their optimal orbital overlap between the HOMO and LUMO that stem from the coplanar arrangement of the ligand π system.[17–22] Within such systems, asymmetric LL′CT complexes employ two different ligands resulting in a polar excited state that is attractive for DSSCs. The stability and the tunability of redox-active ligands on a LL′CT dye was demonstrated on a series of Ni(II) square planar catecholate diimine complexes.[23,24] The varying reduction potentials of the redox-active catecholates and diimines allow one to serve as a donor and the other as an acceptor.[23,25] The complexes exhibited LL′CT transitions, as identified as an intense absorption in the visible region of the electromagnetic spectrum, confirming the dependency of the transition energy to the donor and acceptor ligands. The LL′CT band could be tuned

up to 0.8 eV by adjusting the electron-donating and accepting abilities of the two ligands, emphasizing its tunability.

Previous studies have been focused on d^8 metals which allow for the square planar geometry that maximizes the ligand orbital overlap through the d orbitals, as well as a mostly filled metal orbital that minimally impacts the charge transfer.[26] Recent studies have found that slight mixing of redox-active metal orbitals can aid in a charge transfer between ligand orbitals with a dihedral angle less than 180 °.[27] However, there are very few cases of LL′CT reported in group IV complexes so far, and even fewer attempts at tuning the energetics of the absorption.[28]

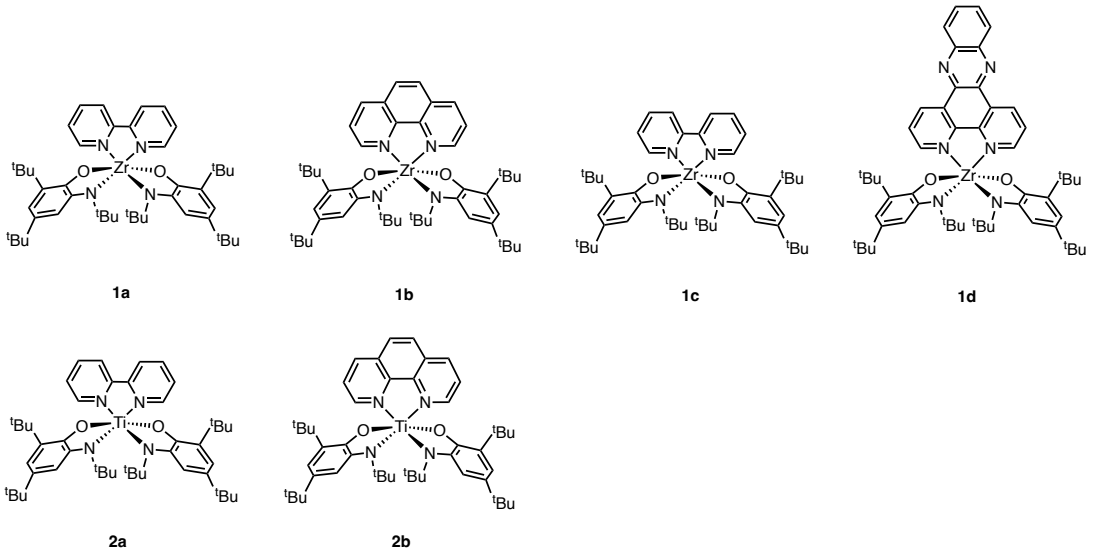

Scheme 4.2 Complexes presented in this chapter.

In this study, a series of six-coordinate titanium(IV) and zirconium(IV) donor-acceptor complexes were synthesized to explore the effects of geometry and the empty metal d orbital to the LL′CT band energy. Group IV metals were chosen to investigate the effects of changing the geometry of the complex from the four-coordinate square planar to six-coordinate pseudo-octahedral and the effects of the metal d electrons by using formally d^0 M^{4+} ions. Amidophenolates were chosen as the donor as they have been reported as electron sources for "oxidative addition" and "reductive elimination"-like reactivity on redox-innocent

metals,[29–31] which highlights their ability to store electrons. A library of bipyridines, which are commonly used as electron acceptors in MLCT dyes, have been selected to observe the effect of acceptor orbital energy on the putative charge transfer. This chapter reports the study on the effects of geometry and metal d electrons using zirconium(IV) and titanium(IV) donor-acceptor complexes.

4.2. Results

4.2.1. Synthesis

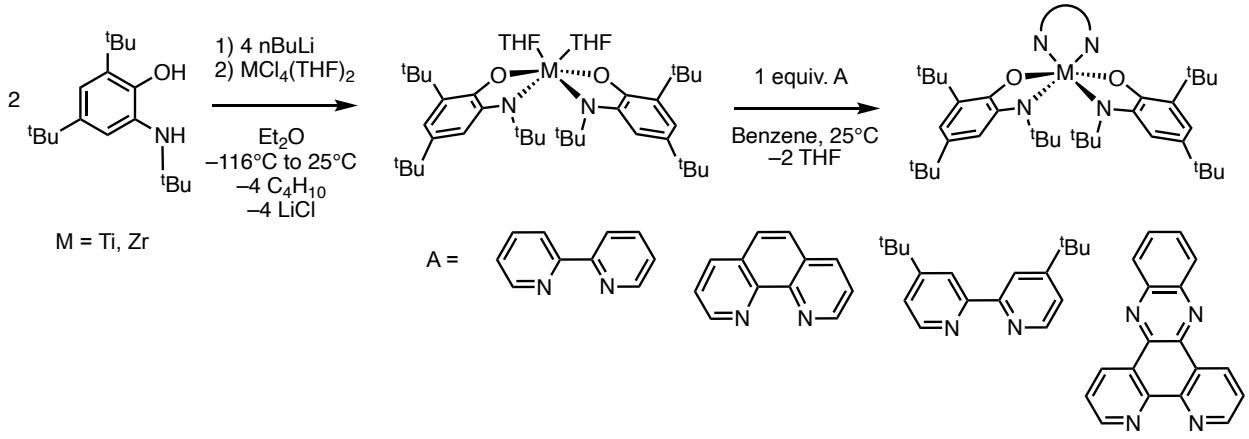

Scheme 4.3 Synthesis of **1a-d** and **2a-b**.

Previously reported titanium (IV) and zirconium (IV) complexes with fully reduced amidophenolates, Ti(^{tBu}ap)$_2$(THF)$_2$ and Zr(^{tBu}ap)$_2$(THF)$_2$,[29,30] were chosen as the synthons for the LL′CT dyes. The acceptors of choice were a series of bipyridine moieties with varying electronic properties (bpy = 2,2'-bipyridine, ^{tBu}bpy = 4,4'-di-*tert*-butyl-2,2'-bipyridine, phen = 1,10-phenanthroline, dipph = dipyridophenazine). Due to the hypothesized lability of the THF adducts and the chelating effect of the bipyridines, the ligand exchange between THF of the synthon and the bipyridine derivative led to a clean conversion to the desired donor-acceptor. Upon addition of 1 equivalent of the bipyridine-like acceptors in benzene to the zirconium moiety yielded an instant color change from light orange to deep green or blue, yielding a series of donor-acceptor complexes Zr(^{tBu}ap)$_2$bpy (**1a**), Zr(^{tBu}ap)$_2$phen (**1b**),

$Zr(^{tBu}ap)_2$dipph (**1c**), and $Zr(^{tBu}ap)_2{}^{tBu}$bpy (**1d**). Similarly, titanium analogues of the complexes were synthesized from the bis-amidophenolate bis-THF complexes which yielded $Ti(^{tBu}ap)_2$bpy (**2a**), $Ti(^{tBu}ap)_2$phen (**2b**).

4.2.2. Structural Analysis

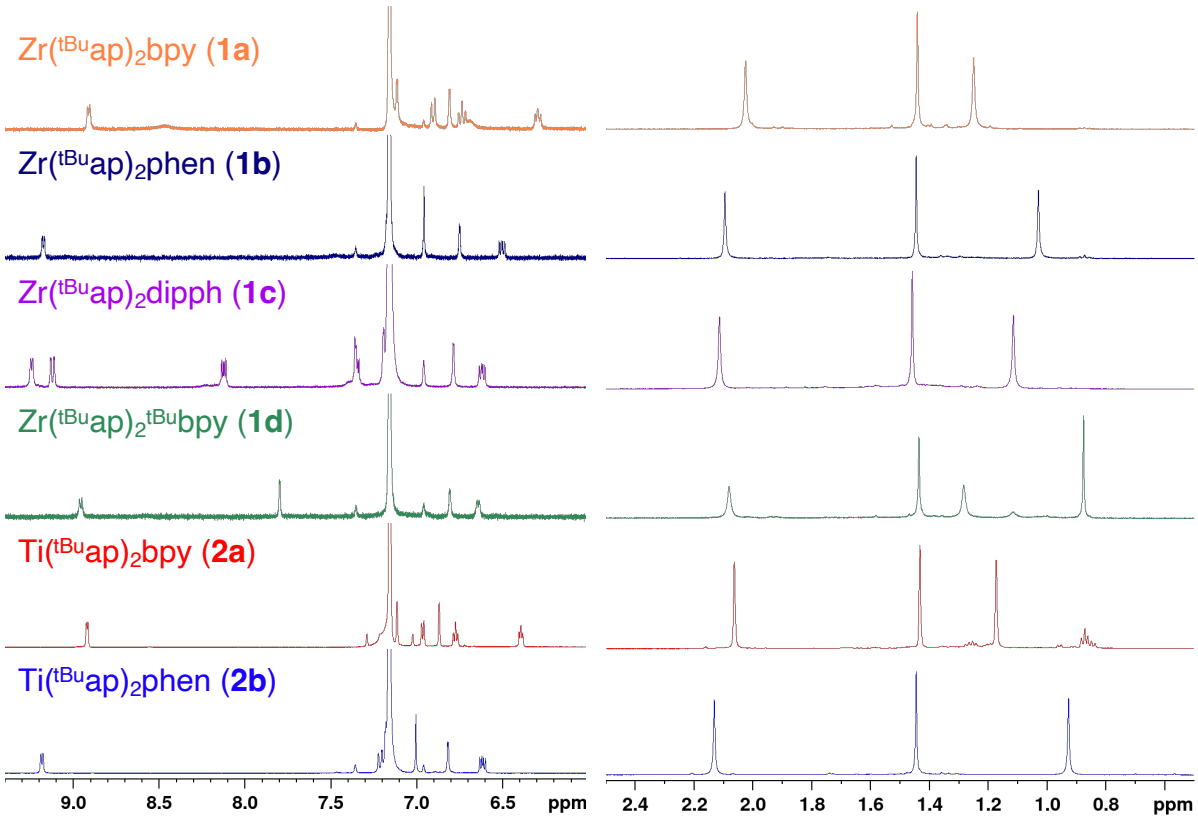

Figure 4.1 ^{1}H NMR of $Zr(^{tBu}ap)_2$A (A = bpy, phen dipph, ^{tBu}bpy) and $Ti(^{tBu}ap)_2$A (A = bpy, phen) (top to bottom) in benzene-d_6 at 298K. Residual proteo solvent signal appears at 7.16 ppm. Satellite peaks from the residual solvent signal are observed at 6.96 and 7.36 ppm. Minor solvent impurities from pentane and THF are present in **2a** near 0.8 ppm.

All of the complexes display sharp NMR signals in the diamagnetic region in C_6D_6 as presented in **Figure 4.1**. The *tert*-butyl protons on the amidophenolates provide easily distinguishable group of three singlets in the aliphatic region between 0.8 and 2.2 ppm as a spectroscopic handle. The aromatic peaks of the amidophenolates show up between 6.8 and 7.5 ppm, as two singlets. Some of the aromatic signals overlap with the residual proteo solvent signal at 7.16 ppm and the satellite peaks at 6.96 and 7.36 ppm in C_6D_6. However,

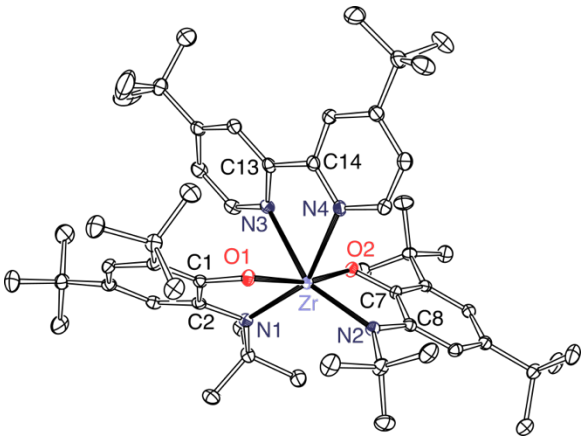

Figure 4.2 ORTEP diagram of **1d** with thermal ellipsoids shown at 50 % probability. Hydrogen atoms and solvent molecules have been omitted for clarity.

the complexes quickly decompose upon solvation in acetonitrile and halogenated solvents and revert to the bis-THF complex upon solvation in THF after prolonged exposure. Therefore, diagnostic NMRs of all complexes in this study have been collected in deuterated benzene for consistency. The signals from both donor amidophenolate ligands are identical and that of the acceptors are symmetric in the NMR timeframe, which agrees with a C_{2v} symmetry environment.

High-resolution single-crystal X-ray diffraction studies were performed to determine the solid-state structures of the complexes. Due to the highly oxophilic and water-sensitive nature of the group IV complexes,[32,33] X-ray quality single crystals were only successfully harvested from $Zr(^{tBu}ap)_2{}^{tBu}bpy$. The key bond distances are reported in **Table 4.1**, and the molecular structure of the solid state is shown in **Figure 4.2**. The complex adopts a distorted trigonal antiprism geometry where the oxygen atoms of the amidophenolate ligands are located trans to each other, consistent with its synthon and similar early metal complexes with bis-redox-active donors. The oxidation

Table 4.1 Selected bond distances of $Zr(^{tBu}ap)_2{}^{tBu}bpy$ and the previously reported $Zr(^{tBu}ap)_2(THF)_2$[30] in solid state.

Distance / Å		
Complex	**2d**	**Bis-THF[30]**
Zr-O(1)	2.0402(14)	2.057(3)
Zr-N(1)	2.1356(17)	2.216(4)
O(1)-C(1)	1.363(2)	1.358(5)
N(1)-C(2)	1.415(3)	1.413(6)
C(1)-C(2)	1.423(3)	1.424(6)
C(2)-C(3)	1.399(3)	1.396(6)
C(3)-C(4)	1.399(3)	1.394(7)
C(4)-C(5)	1.386(3)	1.387(7)
C(5)-C(6)	1.403(3)	1.394(6)
C(6)-C(1)	1.397(3)	1.400(6)
C(13)-C(14)	1.483(3)	-
MOS	**−1.91**	**−1.94**
Angle / °		
O(1)-Zr-O(2)	163.73(6)	159.9
N(1)-Zr-N(2)	115.17(7)	103.9
O(1)ZrN(1)-N(3)ZrN(4)	80.3	
O(2)ZrN(2)-N(3)ZrN(4)	87.5	

states of the ligands can be determined by comparing the key bond distances involving the backbone of the amidophenolates and the 2 and 7 carbons on the bipyridine to literature precedents.[34] In the donors, the decrease of the O-C(1) and the N-C(2) bond distances as well as the localization of the C-C double bonds on the backbone ring are expected as the ligand becomes more oxidized. For the ^{tBu}bpy, the C(7)-C(8) bond distance will decrease as it gets reduced. Both of the amidophenolates on the complex displayed bond distances consistent with the fully reduced, –2 oxidation state assignment. As for the ^{tBu}bpy, the C(7)-C(8) bond distance was 1.483 Å, which is consistent with the fully oxidized neutral assignment. The dihedral angle between each ^{tBu}ap and the ^{tBu}bpy were 80.3 ° and 87.5 °.

4.2.3. Spectroscopic Analysis

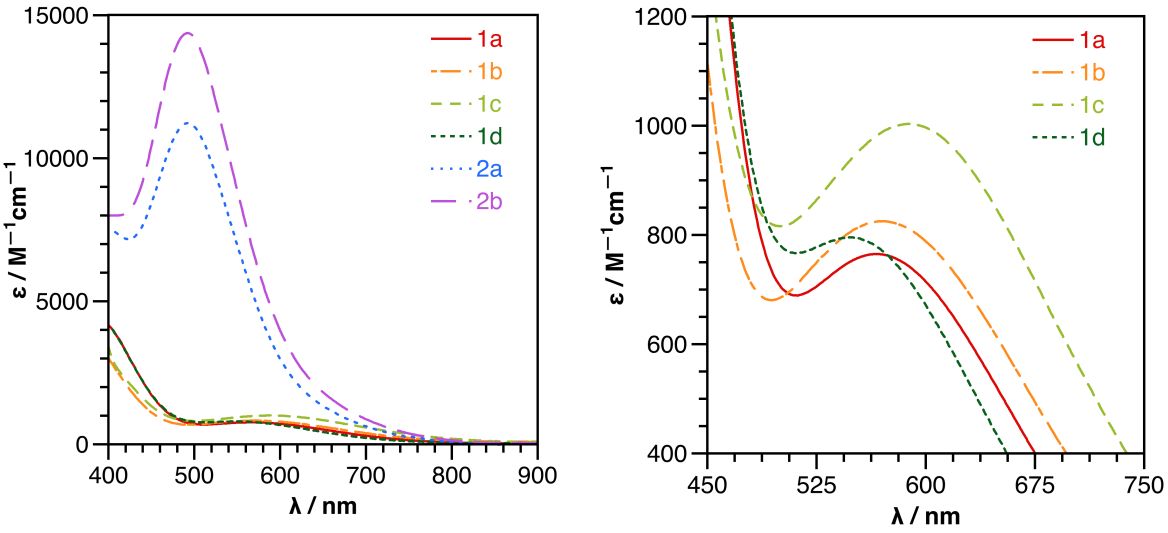

Figure 4.3 Electronic absorption spectra of complexes **1a-d**, **2a-b** (left). A zoom-in of the same spectra between 450 and 750 nm (right).

Spectroscopic studies were performed to determine how changes to the acceptor ligand and to the metal ion changed the light-absorbing properties of the dono-acceptor complexes. The solution absorption spectra reported in **Figure 4.3** were collected in benzene at 298 K. The complexes are characterized by an absorption peak at 500-600 nm in the UV-Vis-NIR

region. The energy and extinction coefficients for the low energy absorption varied significantly between the zirconium and titanium complexes. For the zirconium complexes, the band at 550-590 nm had less intense absorption than the titanium complexes (1000 $M^{-1}cm^{-1}$ vs. 11000-15000 $M^{-1}cm^{-1}$). The complex with dipph as the acceptor exhibited a 20 nm (0.08 eV) bathochromic shift compared to complexes with bpy and phen acceptors. While the energy of the band between **1a** and **1b** were not significantly different, an increase in the intensity was observed from **1a**, **1b**, and **1d**, which correlated with the size of the acceptor's aromatic backbone.

Table 4.2 UV-vis transitions of complexes **1a-d** and **2a-b** in benzene.

Complex	1a	1b	1c	1d	2a	2b
λ / nm	566	570	589	550	492	492
λ / eV	2.19	2.18	2.10	2.25	2.52	2.52
ε / $M^{-1}cm^{-1}$	760	820	1000	920	11000	14000

4.2.4. Density Functional Theory Calculations

Density functional theory (DFT) calculations were performed on all complexes using the Gaussian 16 suite to aid in the designation of the orbitals involved in the low energy peak

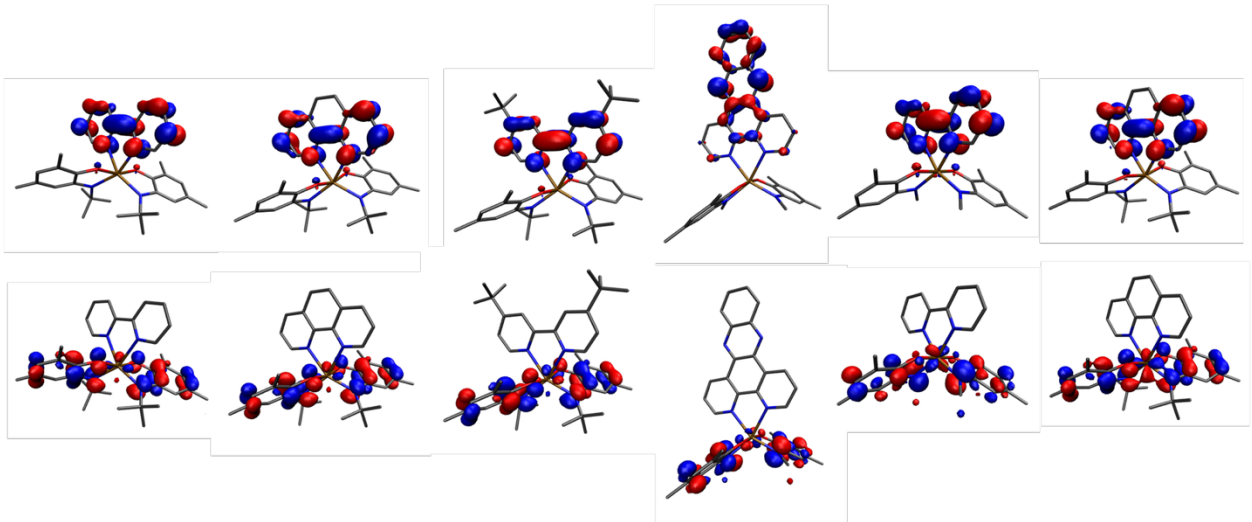

Figure 4.4 Kohn-Sham representations of the HOMO (bottom) and LUMO (top) of **1a-d** and **2a-b** (left to right).

in the absorption spectra. The calculations were performed with the B3LYP exchange-correlation functional in the LANL2DZ basis set. The solid-state structure for $Zr(^{tBu}ap)_2{}^{tBu}bpy$ was substituted accordingly as the starting point for the calculations, as solid state structures for the rest of the complexes have yet to be obtained. The *tert*-butyl groups on the ^{tBu}ap were substituted with methyl groups in order to minimize the computational load. The bond metrics obtained from the optimized geometry and thermodynamic frequency calculations were within 0.04 Å with the experimental structural data for $Zr(^{tBu}ap)_2{}^{tBu}bpy$ for the metal-heteroatom bond distances, and within 0.02 Å for the intraligand bond distances. Full population analysis yielded the atomic charge distributions for the frontier molecular orbitals, presented in **Table 4.3**.

Table 4.3 Mulliken population analysis atomic charge distributions for frontier molecular orbitals and their calculated energy difference.

	HOMO				LUMO		Energy gap
	M / %	N(tBuap) / %	O / %	C(tBuap) / %	N(bpy) / %	C(bpy) / %	/ eV
1a	7.7	17.4	14.3	54.5	23.3	72.5	0.061
1b	7.6	17.4	14.4	54.2	24.5	70.7	0.062
1c	6.4	31.3	3.8	51.1	37.5	62.0	0.028
1d	7.7	17.6	14.3	54.1	21.9	73.1	0.068
2a	7.9	32.7	2.5	50.4	23.1	70.3	0.060
2b	11.0	14.5	14.2	54.8	24.5	69.6	0.075

The HOMO for the complexes almost entirely consists of the amidophenolate ligands with the total percentage of contribution around 85 % while a small contribution about 10 % comes from the metal. The LUMO is almost entirely localized on the bpy variants. The

HOMO–1 orbitals were calculated to have comparable energies within 0.01 eV to HOMO for all of the complexes, and they also had near 10 % contributions from the metal.

Time dependent density functional theory calculations with correction for solvent dielectric in benzene were also performed for complexes **1a-d** (**Figure 4.5**). The calculated energies of the low energy transitions were sensitive to the acceptor ligand and followed the trend of the experimentally observed low energy transitions. There were discrepancies between the calculated and experimentally observed excitation energy and oscillator strength, where the excitation energy was consistently underestimated while the oscillator strength was consistently overestimated. The overestimated oscillator strength could be evidence that the overlap integral of the orbitals involved in the transition mostly originate from the d orbital of the metal.[27]

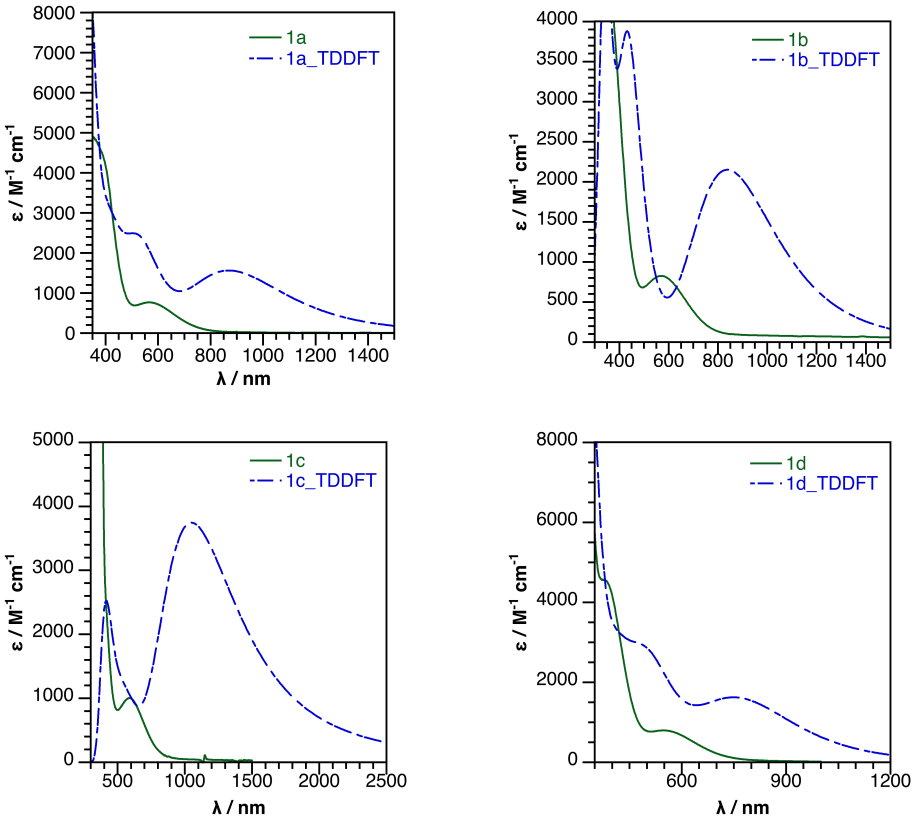

Figure 4.5 TD-DFT UV-Vis plot (purple broken line) and experimentally obtained UV-Vis spectra (green solid line) of **1a-d**.

4.3. Discussion

4.3.5. Designation of the oxidation states of the redox-active ligands and metals

The oxidation states of the ligands and the metal need to be elucidated to determine the sites of electron transfer. Therefore, the solid-state bond distances of the ligands were used to determine the oxidation states of the redox-active ligands. In **1d**, the bond distances within the ligand backbone of the ^{tBu}ap agrees with the fully reduced dianionic state expected from the synthon while the ^{tBu}bpy stays neutral after binding to the metal. The metal itself must be in the +4 oxidation state to balance the charge. Therefore, complex **1d** has the potential to display LL′CT from the amidophenolate to the bipyridine, as well as ligand-to-metal charge-transfer (LMCT) from the amidophenolate into the metal.

Even though attempts to obtain structural data from the other complexes were unsuccessful, ^{1}H NMR can be used to determine the chemical environment and the symmetry of the bulk in solution. As with complex **1d**, the rest of the complexes display sharp signals in the diamagnetic region where the peaks from both donors overlap while the peaks from the bpy derivatives also retain their symmetry. From this data, the other complexes are also assumed to be the six-coordinate complexes with C_{2v} symmetry with formally two equivalents of fully reduced amidophenolates and one equivalent of fully oxidized bpy derivative bound to the tetravalent metal. In addition, the UV-Vis absorption spectra which is sensitive to the oxidation state of the amidophenolates are all similar for the zirconium complexes. Complexes **1a-d** all display a peak around 550-600 nm with a low extinction coefficient. The titanium complexes have a different absorption profile where there is a peak at 500 nm with a significantly higher absorption coefficient. The identity of these peaks is discussed below.

4.3.6. Characters of the low energy charge-transfer transition

With the oxidation states of the redox-active ligands assigned, it was clear the metals possessed empty d orbitals which introduce a possibility of an LMCT from the electron rich amidophenolates into the metal. As expected, the synthons $Zr(^{tBu}ap)_2(THF)_2$ and $Ti(^{tBu}ap)_2(THF)_2$ possess a charge-transfer band that has been assigned as the LMCT from the ^{tBu}ap into the respective metals at 340 nm (3.65 eV) and 364 nm (3.41 eV).[30,35] As both the donor ligand and the acceptor metal remain constant between the synthons and the complexes in this work, the LMCT band is not expected to shift significantly above 400 nm. Therefore, the low energy feature observed in the UV-vis absorption spectra presented in **Table 4.2** is not expected to be the LMCT. The prominent low energy feature observed in zirconium complexes **1a-d** is dependent on the energy of the π* orbital of the acceptor bpy variant. Complex **1d**, which has the inductively electron donating *tert*-butyl group in the backbone of the acceptor, has a higher energy transition at 550 nm (2.25 eV) compared to the unsubstituted bpy of **1a** at 566 nm (2.19 eV). An unexpected deviation was that the low energy transition of **1b** was very similar to **1a** despite the increased size of the aromatic backbone. Computational analysis of the LUMO suggests that the added carbons at the 5 and 6 positions do not participate in the low lying π* orbital on the phen, resulting in minimal differences in the energy of the LUMO compared to the unsubstituted bpy complex. This was demonstrated in the experimental spectra where the λ_{max} of the LL′CT absorption 566 and 570 nm for **1a** and **1b**. However, as the size of the aromatic backbone significantly increases to dipph, the extended conjugation leads to a decrease in the energy of the π* orbital which is apparent by the bathochromic shift of the low energy transition from 566 nm (2.19 eV) to 589 nm (2.10 eV). The difference in the energy of the charge-transfer band was tuned by up to 0.15 eV by changing the electron donating and withdrawing ability of the acceptor.

Computational analysis agrees with the experimental data as the energy difference between HOMO and LUMO follows the same pattern. In addition, the lowest energy transitions in the TD-DFT for **1a-d** are calculated to have the largest contributions from both the HOMO-to-LUMO and HOMO–1-to-LUMO transitions. The difference in the extinction coefficient of the transition could be attributed to the increased rigidity of the bpy derivatives, which allows the π* orbital to align better in order to receive the electron. Therefore, the low energy transition of the zirconium complexes is most accurately assigned as a LL′CT from the electron rich ^{tBu}ap to the neutral bpy derivatives.

In complexes **1a-d**, the LL′CT transitions had significantly smaller extinction coefficients of less than or equal to 1000 $M^{-1}cm^{-1}$, which is considered to be the low end for charge transfer bands.[36] Theoretically, approaching to a 90 ° angle between the donor and acceptor orbitals would decrease the oscillator strength to zero as the overlap integral goes to zero in orthogonal orbitals. Experimentally, diminishing LLCT or LL′CT absorptions have been observed in symmetric and asymmetric charge-transfer complexes with ligands situated at an angle less than 180 ° through a bulky ligand design or control of the coordination environment.[26,27] Therefore, the diminished intensity of the absorption is most likely due to the decrease in overlap of the donor and acceptor orbitals due to the decrease in the dihedral angle (80.3 °) between the donor and acceptor ligands.

The identity of the metal greatly affected the energy and the extinction coefficient of the LL′CT. In the titanium complexes, the extinction coefficients observed for the peak at 492 nm were an order of magnitude larger (>11000 $M^{-1}cm^{-1}$) than the LL′CT observed in the zirconium species, which make the complexes deep red. The synthon Ti(^{tBu}ap)$_2$(THF)$_2$ also displays an absorption in the same region, which was designated as a LMCT, which could be observed in both Ti(^{tBu}ap)$_2$(bpy) (**2a**) and Ti(^{tBu}ap)$_2$(phen) (**2b**) as the metal and the donor are

identical. However, the observed extinction coefficient for the LMCT transition is only 4000 $M^{-1}cm^{-1}$, insufficient to be responsible for the tenfold difference between the synthon and the donor-acceptor complexes. It is most likely that the HOMO of the amidophenolates are mixing more extensively with the titanium d orbitals, which would delocalize the donor orbitals onto the metal. The resulting increased proximity of the donor orbital to the acceptor orbital would greatly increase the oscillator strength of the charge-transfer. Another less likely possibility is that the titanium is accessing the Ti(III) oxidation state through the donation of electrons from the donor ligands, which is more stable than Zr(III).[37,38] Without the solid-state structure of **2a** or **2b**, it is difficult to unequivocally determine the oxidation state of the titanium metal as +4. Charge transfer bands in $Ti^{III}Cl_3$(bpy)(MeCN) in acetonitrile are reported to be observed around 400 nm and 550 nm, near the observed 492 nm for the titanium complexes. These charge transfers of different ligand and metal characters that may occur near one another could explain the broadness and increased intensity of the low energy transition of the titanium analogues compared to the zirconium analogues.

4.4. Conclusion

Six new donor-acceptor complexes of tetravalent metal were synthesized. The lowest energy transitions in the UV-Vis region of the complexes have been determined to be predominantly LL′CT from the amidophenolate donor to the bipyridine acceptor. By changing the acceptor, the energy of the charge transfer could be tuned by up to 0.15 eV. The titanium complexes exhibit broader and higher intensity absorption due to a higher degree of covalency between the metal and ligand, while the zirconium analogues possess a transition that is at a lower intensity due to smaller overlap between the donor and acceptor orbitals. These

results show that geometric and electronic factors can be leveraged to design tunable LL′CT dyes relevant to light-harvesting applications.

4.5. Experimental

The reactions below were carried out using standard Schlenk-line and glovebox techniques under nitrogen. Solvents were sparged with argon before being deoxygenated and dried by Q5 and activated alumina columns. 3,5-di-*tert*-butyl-1,2-quinone, bipyridine, phenanthroline, nBuLi (2.85M in hexane), and $ZrCl_4$ were reagent grade or better and used as received. The 2,4-di-*tert*-butyl-6-(*tert*- butylamino)phenol ligand (apH_2), 4,6-di-*tert*-butyl-2-(phenylamino)phenol ($apPhH_2$), Dipyrido[3,2-a:2′,3′-c]phenazine (dipph)[39] and $ZrCl_4(THF)_2$ was prepared according to published procedures.[19,29] $Zr(ap)_2(THF)_2$ was prepared according to published procedure[29] and was recrystallized from chilled pentane solutions. NMR spectra were collected at 298 K on Bruker Avance 400 MHz and 500 MHz spectrometers in dried and degassed C_6D_6, $CDCl_3$, and CD_2Cl_2. ^1H NMR spectra were referenced to TMS using the residual proteo impurities (7.16 ppm for benzene) of the solvents and ^{13}C NMR spectra were referenced to TMS using the natural ^{13}C abundance of the solvent. ^{31}P NMR were referenced using an external reference H_3PO_4 (85 %) at 0 ppm. All chemical shifts are reported using the standard notation in parts-per-million with positive shifts to higher frequency from given reference. Electronic absorption spectra were recorded with either the JASCO V-670 UV-Vis-NIR Spectrophotometer or the PerkinElmer Lambda 800 UV-Vis Spectrophotometer in dry, degassed solvents using 1 cm path length cuvettes in ambient temperature (20-24 °C).

X-ray diffraction data were collected on single crystals mounted on glass fiber loops using Bruker CCD platform diffractometer equipped with a CCD detector at 143 K using Mo Kα (λ = 0.71073 Å) radiation, which was wavelength selected with a single-crystal graphite monochromator. A full sphere of data was collected for each crystal structure. The SMART program package was used to determine unit-cell parameters and to collect data. The raw frame data were processed using SAINT[40] and SADABS[41] to yield the reflection data files. Subsequent calculations were carried out using the SHELXTL[42] program suite. Structures

were solved by direct methods and refined on F^2 by full-matrix least-squares techniques to analyses. Hydrogen atoms, through visible in the difference Fourier map, were generated at calculated positions and their positions refined using the riding model. ORTEP diagrams were generated using ORTEP-3[43] for Windows. Bond distances were extracted in Mercury for Windows. All DFT calculations were performed using Gaussian 16[44] employing B3LYP/6-311G and LANL2DZ level of theory. VMD for Windows was used for 3D rendering of molecular orbitals.

Synthesis of $Zr(ap)_2(bpy)$ (**1a**)

In a 20 mL scintillation vial, $Zr(ap)_2(THF)_2$ (0.091 g, 0.12 mmol, 1 equiv.) was dissolved in 10 mL benzene. To it, 2,2'-bipyridine (0.018 g, 0.12 mmol, 1 equiv.) dissolved in 3 mL benzene was added at once. The golden orange solution turned dark green instantly. The resulting solution was lyophilized to obtain the product as a deep blue powder in 94.2 % yield (0.087 g). ^{1}H NMR (400 MHz, C_6D_6) δ/ppm: 1.25 (s, 18H, $C(CH_3)_3$), 1.44 (s, 18H, $C(CH_3)_3$), 2.03 (s, 18H, $C(CH_3)_3$), 6.29 (t, J = 6.2 Hz, 3H, aryl-H), 6.73 (t, J = 6.8 Hz, 2H, aryl-H), 6.80 (s, 2H, aryl-H), 6.90 (d, J = 8.5 Hz, 2H, aryl-H), 7.12 (s, 2H, aryl-H), 8.91 (s, 2H, aryl-H)

Synthesis of $Zr(ap)_2(phen)$ (**1b**)

In a 20 mL scintillation vial, $Zr(ap)_2(THF)_2$ (0.121 g, 0.154 mmol, 1 equiv.) was dissolved in 8 mL benzene. To it, 1,10-phenanthroline (0.028 g, 0.16 mmol, 1 equiv.) dissolved in 5 mL benzene was added at once. The golden orange solution turned dark green instantly. The resulting solution was lyophilized to obtain the product as a deep blue powder in 88.9 % yield (0.113 g). ^{1}H NMR (400 MHz, C_6D_6) δ/ppm: 1.03 (s, 18H, $C(CH_3)_3$), 1.45 (s, 18H, $C(CH_3)_3$), 2.10 (s, 18H, $C(CH_3)_3$), 6.50 (dd, J = 8.2, 4.8 Hz, 2H, aryl-H), 6.75 (s, 2H, aryl-H), 6.96 (s, 2H, aryl-H), 7.17 (m, 2H, aryl-H), 9.18 (d, J = 5.2 Hz, 2H, aryl-H)

Synthesis of $Zr(ap)_2(dipph)$ (**1c**)

In a 20 mL scintillation vial, $Zr(ap)_2(THF)_2$ (0.105 g, 0.133 mmol, 1 equiv.) was dissolved in 8 mL benzene. To it, dipyridophenazine (0.038 g, 0.13 mmol, 1 equiv.) suspended in 5 mL benzene was added dropwise. The golden orange solution turned dark green within 5 seconds. The resulting solution was lyophilized to obtain the product as a deep blue powder in 84.5 % yield (0.104 g). ^{1}H NMR (400 MHz, C_6D_6) δ/ppm: 1.12 (s, 18H, $C(CH_3)_3$), 1.46 (s, 18H, $C(CH_3)_3$), 2.11 (s, 18H, $C(CH_3)_3$), 6.61 (dd, J = 8.3, 5.0 Hz, 2H, aryl-H), 6.78 (s, 2H, aryl-H), 7.19 (s, under proteo solvent peak, aryl-H), 7.35 (m, 2H, aryl-H), 8.11 (dd, J = 6.6, 3.4 Hz, 2H, aryl-H), 9.11 (dd, J = 1.4, 8.1 Hz, 2H, aryl-H), 9.23 (d, J = 3.6 Hz, 2H, aryl-H)

Synthesis of $Zr(ap)_2(^{tBu}bpy)$ (**1d**)

In a 20 mL scintillation vial, $Zr(ap)_2(THF)_2$ (0.113 g, 0.144 mmol, 1 equiv.) was dissolved in 10 mL benzene. To it, 4,4'-di-*tert*-butyl-2,2'-bipyridine (0.039 g, 0.144 mmol, 1 equiv.) dissolved in 5 mL benzene was added at once. The golden orange solution turned dark green instantly. The resulting solution was lyophilized to obtain the product as a deep brownish green powder in 96.0 % yield (0.126 g). 1H NMR (400 MHz, C6D6) δ/ppm: 0.88 (s, 18H, $C(CH_3)_3$), 1.29 (s, 18H, $C(CH_3)_3$), 1.44 (s, 18H, $C(CH_3)_3$), 2.08 (s, 18H, $C(CH_3)_3$), 6.65 (d, J = 4.3 Hz, 2H, aryl-H), 6.81 (s, 2H, aryl-H), 7.80 (s, 2H, aryl-H), 8.95 (d, J = 6.0 Hz, 2H, aryl-H)

Table 4.4 X-ray diffraction data collection and refinement parameters for complex **1d**.

Complex	2b
empirical formula	$C_{54}H_{82}N_4O_2Zr \cdot ?(C_5H_{12})$
formula weight	910.45
crystal system	Monoclinic
space group	$P2_1/n$
T / K	133.15
***a* / Å**	10.0734(10)
***b* / Å**	19.903(2)
***c* / Å**	27.371(3)
***α* / °**	90
***β* / °**	91.4288(18)
***γ* / °**	90
***V* / Å^3**	5485.9(10)
Z	4
refl. collected	93324
Data/restraints/parameters	11261 / 0 / 574
R1 (*I*> 2*σ*)[a]	0.0389
***w*R2 (all data)[b]**	0.0934
***GOF*[c]**	1.024

[a] $R1 = \Sigma | |F_o| - |F_c| | / \Sigma |F_o|$; [b] $wR2 = [\Sigma[w(F_o^2 - F_c^2)^2] / \Sigma[w(F_o^2)^2]]^{1/2}$
[c] Goodness of Fit = $S = [\Sigma [w(F_o^2 - F_c^2)^2] / (n-p)]^{1/2}$ where n is the number of reflections and p is the total number of parameters refined.

Synthesis of $Ti(ap)_2(bpy)$ (**2a**)

In a 20 mL scintillation vial, apH_2 (0.250 g, 0.900 mmol, 1 equiv) was dissolved in 10 mL Et_2O. The solution was frozen in a liquid nitrogen cold well. The solution was removed from the cold well and while it was thawing, n-butyllithium (0.72 mL, 1.8 mmol, 2 equiv) was added. The solution was allowed to warm to room temperature and was stirred for 1.5 hours. Then it was reintroduced to the nitrogen cold well to freeze. As it thawed, $TiCl_4(THF)_2$ was added at once. As the solution warmed up to room temperature, it changed color to dark green, purple, then red. After 1 hour, the solution was filtered over celite to remove LiCl and 2,2'-bipyridine (0.071 g, 0.46 mmol, 0.5 equiv) was added. No visible color change was

observed. The solution was concentrated into a solid and the product was extracted with pentane. Brown solids that crashed out of the chilled pentane solution was collected to be 221.5 mg (32.6 % yield). ^{1}H NMR (600 MHz, C_6D_6) δ/ppm: 1.17 (s, 18H, C(CH3)3), 1.43 (s, 18H, C(CH3)3), 2.06 (s, 18H, C(CH3)3), 6.39 (t, J = 6.4 Hz, 2H, aryl-H), 6.76 (s, 2H, aryl-H), 6.87 (s, 2H, aryl-H), 6.96 (d, J = 7.9 Hz, 2H, aryl-H), 7.11 (s, 2H, aryl-H), 8.91 (d, J = 5.1 Hz, 2H, aryl-H)

Synthesis of $Ti(ap)_2(phen)$ (**1b**)

In a 20 mL scintillation vial, $Ti(ap)_2(THF)_2$ (0.226 g, 0.296 mmol, 1 equiv.) was dissolved in 8 mL benzene. To it, 1,10-phenanthroline (0.054 g, 0.30 mmol, 1 equiv.) was added at once. The solution turned deep greenish brown after 30 minutes. The resulting solution was lyophilized to obtain the product as a deep brown powder in 96.0 % yield (0.227 g). ^{1}H NMR (400 MHz, C_6D_6) δ/ppm: 0.93 (s, 18H, $C(CH_3)_3$), 1.45 (s, 18H, $C(CH_3)_3$), 2.13 (s, 18H, $C(CH_3)_3$), 6.61 (dd, J = 8.1, 4.9 Hz, 2H, aryl-H), 6.82 (d, J = 1.9 Hz, 2H, aryl-H), 7.01 (s, 2H, aryl-H), 7.20-7.22 (m, 4H, aryl-H), 9.18 (dd, J = 1.4, 4.9 Hz, 2H, aryl-H)

4.6. References

(1) Hagfeldt, A.; Boschloo, G.; Sun, L.; Kloo, L.; Pettersson, H. Dye-Sensitized Solar Cells. *Chem. Rev.* **2010**, *110* (11), 6595–6663. https://doi.org/10.1021/cr900356p.

(2) Grätzel, M. Dye-Sensitized Solar Cells. *J. Photochem. Photobiol. C Photochem. Rev.* **2003**, *4* (2), 145–153. https://doi.org/10.1016/S1389-5567(03)00026-1.

(3) Mounika, P. M.; Ambapuram, M.; Maddala, G.; Kalvapalli, S.; Ganesha, M. K.; Singh, A. K.; Thota, N.; Rajesh, M. N.; Giribabu, L.; Venkateswarlu, K.; Mitty, R. Unveiling a New Frontier in Efficient Solar Power Conversion with a Pioneering Bifacial Tandem Dye-Sensitized Solar Cell. *ACS Appl. Electron. Mater.* **2023**, *5* (10), 5661–5667. https://doi.org/10.1021/acsaelm.3c01000.

(4) Prajapat, K.; Mahajan, U.; Kumar, A.; Dhonde, M.; Sahu, K.; Vyas, S.; Riyad, Y. M.; El-Bahy, Z. M. Next-Generation Counter Electrodes for Dye-Sensitized Solar Cells: A Comprehensive Overview. *Sustain. Mater. Technol.* **2024**, *42*, e01178. https://doi.org/10.1016/j.susmat.2024.e01178.

(5) Gust, D.; Moore, T. A.; Moore, A. L. Solar Fuels via Artificial Photosynthesis. *Acc. Chem. Res.* **2009**, *42* (12), 1890–1898. https://doi.org/10.1021/ar900209b.

(6) Kodis, G.; Liddell, P. A.; Moore, A. L.; Moore, T. A.; Gust, D. Synthesis and Photochemistry of a Carotene–Porphyrin–Fullerene Model Photosynthetic Reaction Center. *J. Phys. Org. Chem.* **2004**, *17* (9), 724–734. https://doi.org/10.1002/poc.787.

(7) Kelber, J. B.; Panjwani, N. A.; Wu, D.; Gómez-Bombarelli, R.; Lovett, B. W.; Morton, J. J. L.; Anderson, H. L. Synthesis and Investigation of Donor–Porphyrin–Acceptor Triads with Long-Lived Photo-Induced Charge-Separate States. *Chem Sci* **2015**, *6* (11), 6468–6481. https://doi.org/10.1039/C5SC01830G.

(8) Miwa, K.; Aoyagi, S.; Sasamori, T.; Ueno, H.; Okada, H.; Ohkubo, K. Anionic Fluorinated Zn-Porphyrin Combined with Cationic Endohedral Li-Fullerene for Long-Lived Photoinduced Charge Separation with Low Energy Loss. *J. Phys. Chem. B* **2021**, *125* (3), 918–925. https://doi.org/10.1021/acs.jpcb.0c10450.

(9) Verma, S.; Kar, P.; Das, A.; Ghosh, H. N. Photophysical Properties of Ligand Localized Excited State in Ruthenium(Ii) Polypyridyl Complexes: A Combined Effect of Electron Donor–Acceptor Ligand. *Dalton Trans.* **2011**, *40* (38), 9765. https://doi.org/10.1039/c1dt10266d.

(10) Burstall, F. H. 34. Optical Activity Dependent on Co-Ordinated Bivalent Ruthenium. *J. Chem. Soc. Resumed* **1936**, 173. https://doi.org/10.1039/jr9360000173.

(11) Wu, C.-G. Ruthenium-Based Complex Dyes for Dye-Sensitized Solar Cells. *J. Chin. Chem. Soc.* **2022**, *69* (8), 1242–1252. https://doi.org/10.1002/jccs.202200225.

(12) Greaney, M. J.; Araujo, J.; Burkhart, B.; Thompson, B. C.; Brutchey, R. L. Novel Semi-Random and Alternating Copolymer Hybrid Solar Cells Utilizing CdSe Multipods as

Versatile Acceptors. *Chem. Commun.* **2013**, *49* (77), 8602. https://doi.org/10.1039/c3cc44536d.

(13) Jaysankar, M.; Filipič, M.; Zielinski, B.; Schmager, R.; Song, W.; Qiu, W.; Paetzold, U. W.; Aernouts, T.; Debucquoy, M.; Gehlhaar, R.; Poortmans, J. Perovskite–Silicon Tandem Solar Modules with Optimised Light Harvesting. *Energy Environ. Sci.* **2018**, *11* (6), 1489–1498. https://doi.org/10.1039/C8EE00237A.

(14) Zheng, J.; Duan, W.; Guo, Y.; Zhao, Z. C.; Yi, H.; Ma, F.-J.; Granados Caro, L.; Yi, C.; Bing, J.; Tang, S.; Qu, J.; Fong, K. C.; Cui, X.; Zhu, Y.; Yang, L.; Lambertz, A.; Arafat Mahmud, M.; Chen, H.; Liao, C.; Wang, G.; Jankovec, M.; Xu, C.; Uddin, A.; Cairney, J. M.; Bremner, S.; Huang, S.; Ding, K.; McKenzie, D. R.; Ho-Baillie, A. W. Y. Efficient Monolithic Perovskite–Si Tandem Solar Cells Enabled by an Ultra-Thin Indium Tin Oxide Interlayer. *Energy Environ. Sci.* **2023**, *16* (3), 1223–1233. https://doi.org/10.1039/D2EE04007G.

(15) Fox, G. A.; Pierpont, C. G. Periodic Trends in Charge Distribution for Transition Metal Complexes Containing Catecholate and Semiquinone Ligands. Metal-Mediated Spin Coupling in the Bis(3,5-Di-Tert-Butyl-1,2-Semiquinone) Complexes of Palladium(II) and Platinum(II) M(DBSQ)2 (M = Pd, Pt). *Inorg. Chem.* **1992**, *31* (18), 3718–3723. https://doi.org/10.1021/ic00044a012.

(16) Chaudhuri, P.; Verani, C. N.; Bill, E.; Bothe, E.; Weyhermüller, T.; Wieghardt, K. Electronic Structure of Bis(*o*-Iminobenzosemiquinonato)Metal Complexes (Cu, Ni, Pd). The Art of Establishing Physical Oxidation States in Transition-Metal Complexes Containing Radical Ligands. *J. Am. Chem. Soc.* **2001**, *123* (10), 2213–2223. https://doi.org/10.1021/ja003831d.

(17) Bachler, V.; Olbrich, G.; Neese, F.; Wieghardt, K. Theoretical Evidence for the Singlet Diradical Character of Square Planar Nickel Complexes Containing Two *o*-Semiquinonato Type Ligands. *Inorg. Chem.* **2002**, *41* (16), 4179–4193. https://doi.org/10.1021/ic0113101.

(18) Ray, K.; Weyhermüller, T.; Neese, F.; Wieghardt, K. Electronic Structure of Square Planar Bis(Benzene-1,2-Dithiolato)Metal Complexes $[M(L)_2]^z$ ($z = 2-, 1-, 0$; M = Ni, Pd, Pt, Cu, Au): An Experimental, Density Functional, and Correlated Ab Initio Study. *Inorg. Chem.* **2005**, *44* (15), 5345–5360. https://doi.org/10.1021/ic0507565.

(19) Herebian, D.; Bothe, E.; Neese, F.; Weyhermüller, T.; Wieghardt, K. Molecular and Electronic Structures of Bis-(*o*-Diiminobenzosemiquinonato)Metal(II) Complexes (Ni, Pd, Pt), Their Monocations and -Anions, and of Dimeric Dications Containing Weak Metal−Metal Bonds. *J. Am. Chem. Soc.* **2003**, *125* (30), 9116–9128. https://doi.org/10.1021/ja030123u.

(20) Herebian, D.; Bothe, E.; Bill, E.; Weyhermüller, T.; Wieghardt, K. Experimental Evidence for the Noninnocence of O-Aminothiophenolates: Coordination Chemistry of o-Iminothionebenzosemiquinonate(1-) π-Radicals with Ni(II), Pd(II), Pt(II). *J. Am. Chem. Soc.* **2001**, *123* (41), 10012–10023. https://doi.org/10.1021/ja011155p.

(21) Vogler, A.; Kunkely, H. Optical Ligand to Ligand Charge Transfer of Metal Complexes Including Ligand-Based Mixed-Valence Systems. *Comments Inorg. Chem.* **1990**, *9* (3–4), 201–220. https://doi.org/10.1080/02603599008035810.

(22) Wootton, J. L.; Zink, J. I. Excited State Distortions in Ligand to Ligand Charge Transfer Excited States of Metal Diimine Dithiolate Mixed Ligand Complexes. *J. Phys. Chem.* **1995**, *99* (19), 7251–7257. https://doi.org/10.1021/j100019a007.

(23) Kramer, W. W.; Cameron, L. A.; Zarkesh, R. A.; Ziller, J. W.; Heyduk, A. F. Donor–Acceptor Ligand-to-Ligand Charge-Transfer Coordination Complexes of Nickel(II). *Inorg. Chem.* **2014**, *53* (16), 8825–8837. https://doi.org/10.1021/ic5017214.

(24) Cameron, L. A.; Ziller, J. W.; Heyduk, A. F. Near-IR Absorbing Donor–Acceptor Ligand-to-Ligand Charge-Transfer Complexes of Nickel(II). *Chem. Sci.* **2016**, *7* (3), 1807–1814. https://doi.org/10.1039/C5SC02703A.

(25) Hanna, M. C.; Nozik, A. J. Solar Conversion Efficiency of Photovoltaic and Photoelectrolysis Cells with Carrier Multiplication Absorbers. *J. Appl. Phys.* **2006**, *100* (7), 074510. https://doi.org/10.1063/1.2356795.

(26) Blanchard, S.; Neese, F.; Bothe, E.; Bill, E.; Weyhermüller, T.; Wieghardt, K. Square Planar vs Tetrahedral Coordination in Diamagnetic Complexes of Nickel(II) Containing Two Bidentate π-Radical Monoanions. *Inorg. Chem.* **2005**, *44* (10), 3636–3656. https://doi.org/10.1021/ic040117e.

(27) Yan, H.; Wu, B.; Wei, J.; Zhang, W.-X. Insight into the Ligand-to-Ligand Charge-Transfer Process in Rare-Earth-Metal Diradical Complexes. *Inorg. Chem.* **2023**, *62* (21), 8052–8057. https://doi.org/10.1021/acs.inorgchem.3c00900.

(28) Patel, S.; Li, Y.; Odom, A. L. Synthesis, Structure, and LLCT Transitions in Terminal Hydrazido(2−) Bipyridine Complexes of Titanium. *Inorg. Chem.* **2007**, *46* (16), 6373–6381. https://doi.org/10.1021/ic700426s.

(29) Blackmore, K. J.; Ziller, J. W.; Heyduk, A. F. "Oxidative Addition" to a Zirconium(IV) Redox-Active Ligand Complex. *Inorg. Chem.* **2005**, *44* (16), 5559–5561. https://doi.org/10.1021/ic050997c.

(30) Blackmore, K. J.; Sly, M. B.; Haneline, M. R.; Ziller, J. W.; Heyduk, A. F. Group IV Imino-Semiquinone Complexes Obtained by Oxidative Addition of Halogens. *Inorg. Chem.* **2008**, *47* (22), 10522–10532. https://doi.org/10.1021/ic801127r.

(31) Fedushkin, I. L.; Dodonov, V. A.; Skatova, A. A.; Sokolov, V. G.; Piskunov, A. V.; Fukin, G. K. Redox-Active Ligand-Assisted Two-Electron Oxidative Addition to Gallium(II). *Chem. – Eur. J.* **2018**, *24* (8), 1877–1889. https://doi.org/10.1002/chem.201704128.

(32) Beweries, T.; Panda, T. K.; Roberts, C. C.; Tsurugi, H. Early Transition Metals in Organometallic Chemistry. *Organometallics* **2023**, *42* (11), 1039–1042. https://doi.org/10.1021/acs.organomet.3c00238.

(33) Romain, C.; Bellemin-Laponnaz, S.; Dagorne, S. Recent Progress on NHC-Stabilized Early Transition Metal (Group 3–7) Complexes: Synthesis and Applications. *Coord. Chem. Rev.* **2020**, *422*, 213411. https://doi.org/10.1016/j.ccr.2020.213411.

(34) Brown, S. N. Metrical Oxidation States of 2-Amidophenoxide and Catecholate Ligands: Structural Signatures of Metal–Ligand π Bonding in Potentially Noninnocent Ligands. *Inorg. Chem.* **2012**, *51* (3), 1251–1260. https://doi.org/10.1021/ic202764j.

(35) Borgias, B. A.; Cooper, S. R.; Koh, Y. B.; Raymond, K. N. Synthetic, Structural, and Physical Studies of Titanium Complexes of Catechol and 3,5-Di-Tert-Butylcatechol. *Inorg. Chem.* **1984**, *23* (8), 1009–1016. https://doi.org/10.1021/ic00176a005.

(36) Figgis, B., N.; Hitchman, M. A. *Ligand Field Theory and Its Applications*; Wiley-VCH: New York, 2000.

(37) Samuel, E. Phosphine Complexes of Ti(III) and Zr(III)" Detection in Solution by EPR/Electrochemical Methods i.

(38) Fowles, G. W. A.; Hoodless, R. A.; Walton, R. A. Complexes of Titanium (III) Chloride with 2,2′-Bipyridyl. *J. Inorg. Nucl. Chem.* **1965**, *27* (2), 391–396. https://doi.org/10.1016/0022-1902(65)80357-8.

(39) Roy, N.; Sen, U.; Ray Chaudhuri, S.; Muthukumar, V.; Moharana, P.; Paira, P.; Bose, B.; Gauthaman, A.; Moorthy, A. Mitochondria Specific Highly Cytoselective Iridium(III)–Cp* Dipyridophenazine (Dppz) Complexes as Cancer Cell Imaging Agents. *Dalton Trans.* **2021**, *50* (6), 2268–2283. https://doi.org/10.1039/D0DT03586F.

(40) Bruker AXS, Inc. SAINT, 2013.

(41) Sheldrick, G. M.; Bruker AXS, Inc. SADABS.

(42) Sheldrick, G. M. SHELXTL, 2001.

(43) Farrugia, L. J. ORTEP-3 for Windows - a Version of ORTEP-III with a Graphical User Interface (GUI). *J. Appl. Crystallogr.* **1997**, *30* (5–1), 565–565. https://doi.org/10.1107/S0021889897003117.

(44) Frisch, M. J.; Trucks, G. W.; Schlegel, H. B.; Scuseria, G. E.; Robb, M. A.; Cheeseman, J. R.; Scalmani, G.; Barone, V.; Petersson, G. A.; Nakatsuji, H.; Li, X.; Caricato, M.; Marenich, A. V.; Bloino, J.; Janesko, B. G.; Gomperts, R.; Mennucci, B.; Hratchian, H. P.; Ortiz, J. V.; Izmaylov, A. F.; Sonnenberg, J. L.; Williams; Ding, F.; Lipparini, F.; Egidi, F.; Goings, J.; Peng, B.; Petrone, A.; Henderson, T.; Ranasinghe, D.; Zakrzewski, V. G.; Gao, J.; Rega, N.; Zheng, G.; Liang, W.; Hada, M.; Ehara, M.; Toyota, K.; Fukuda, R.; Hasegawa, J.; Ishida, M.; Nakajima, T.; Honda, Y.; Kitao, O.; Nakai, H.; Vreven, T.; Throssell, K.; Montgomery Jr., J. A.; Peralta, J. E.; Ogliaro, F.; Bearpark, M. J.; Heyd, J. J.; Brothers, E. N.; Kudin, K. N.; Staroverov, V. N.; Keith, T. A.; Kobayashi, R.; Normand, J.; Raghavachari, K.; Rendell, A. P.; Burant, J. C.; Iyengar, S. S.; Tomasi, J.; Cossi, M.; Millam, J. M.; Klene, M.; Adamo, C.; Cammi, R.; Ochterski, J. W.; Martin, R. L.; Morokuma, K.; Farkas, O.; Foresman, J. B.; Fox, D. J. Gaussian 16 Rev. C.01, 2016.

To philosophize is to know how to live and die.